

Observations
at Millimeter Wavelengths
of Small Angular Scale Isotropy
in the
Cosmic Background Radiation

by

Simon John Elliott Radford
September 30, 1986

©Copyright by
Simon John Elliott Radford
1986

**Observations at Millimeter Wavelengths
of Small Angular Scale Isotropy
in the Cosmic Background Radiation**

by

Simon John Elliott Radford

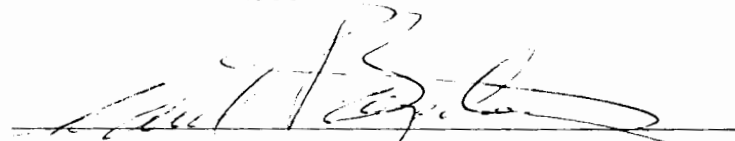
A dissertation submitted in partial fulfillment
of the requirements for the degree of

Doctor of Philosophy

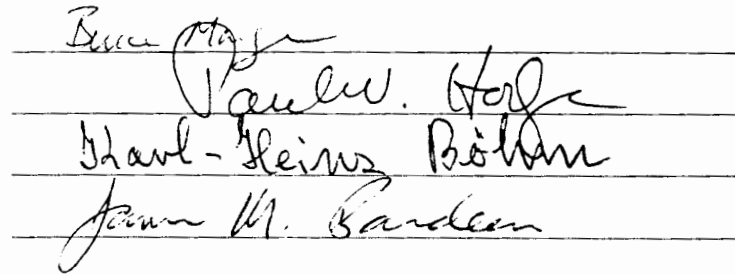
University of Washington

1986

Approved by



(Chairman of the Supervisory Committee)



Program Authorized to Offer Degree Department of Astronomy

September 30, 1986

University of Washington

Abstract

**Observations at Millimeter Wavelengths
of Small Angular Scale Isotropy
in the Cosmic Background Radiation**

by Simon J. E. Radford

Chairman of the Supervisory Committee: Professor Paul E. Boynton
Department of Astronomy

The observed fine scale isotropy of the cosmic background radiation (CBR) is a strong constraint on theories of the genesis and evolution of large scale structure in the universe. This dissertation reports an experiment to determine the amplitude of CBR anisotropies. Observations at a wavelength of 2.2 mm were made with a far infrared photometer based on a composite semiconductor bolometer cooled to 0.35 K by evaporation of ^3He . The photometer was operated in conjunction with a 9m Cassegrain telescope located at an altitude of 1 km at the Battelle Observatory near Richland, WA. The FWHM beamwidth was $4'$, and nutation of the secondary mirror was used to switch the beam over an effective angular scale of $8'$. Although millimeter wavelengths offer several advantages for these observations, previous ground based studies at these wavelengths have been limited by noise due to fluctuations in atmospheric emission and opacity. For this experiment, a sampling technique was developed that substantially reduces the effect of atmospheric noise. Using this technique, these measurements were limited by the intrinsic noise of the detector. The result of five nights' observations in March and April, 1986, is an upper limit to

CBR anisotropies of $\Delta T/T_{\text{CBR}} < 1.2 \times 10^{-4}$ at the 95% confidence level. In addition to demonstrating the performance of the apparatus and the efficacy of the sampling technique, this result is sufficient to constrain some currently popular cosmological models, excluding a baryon dominated universe, for example.

Table of Contents

	<i>Page</i>
Chapter 1: Introduction	1
Chapter 2: Experimental Design	5
Operating Wavelength	5
Spectral Signature	6
Non-cosmological Anisotropies	7
Atmospheric Limitations	8
Detector Properties	9
Angular Scale	13
Angular Correlations	14
Beam Size	15
Sampling Coefficient	18
Number of Sky Regions	21
Atmospheric and Instrumental Noise	22
Celestial Location	26
Chapter 3: Experimental Apparatus	29
Telescope	29
Optical Design	31
Primary Mirror	39
Secondary Mirror and Nutation Mechanism	42
Control System	43
Pointing Performance	45
Photometer	57
Data Acquisition System	58

Chapter 4: Operation and Observations	62
Telescope Focus.....	62
Beam Profile.....	66
Calibration and Atmospheric Opacity	69
Atmospheric Noise Reduction	74
Anisotropy Observations	75
Sampling Pattern.....	77
Observing Sequence	79
Chapter 5: Data Analysis	81
Preliminary Analysis.....	81
Data Editing	82
Scan Averaging.....	83
Polynomial Fitting	84
Wobble Demodulation	85
Region Averages.....	85
Calibration	91
Night Averaging.....	91
Hypothesis Test.....	94
Chapter 6: Interpretation and Summary.....	96
Interpretation.....	96
Summary	99
References	101
Appendix A: A High Performance Beam Switch	109
Introduction.....	109
Optical Design.....	110
System Components	111

Mirror Assembly	111
Driving Motors	116
Mounting	116
Electronic Components	118
Dynamical Analysis	120
Control System Design	125
Operation	127
Appendix B: An Improved Far Infrared Photometer	134
Introduction	134
The Cryogenic System	135
Cooling Procedure	139
Optical Elements	140
Performance	146

List of Figures

	<i>Page</i>
Figure 1.1: Current Observations and Theory.....	4
Figure 2.1: CBR Brightness Spectrum	6
Figure 2.2: CBR Brightness Temperature	7
Figure 2.3: Sky Antenna Temperature	8
Figure 2.4: Angular Correlation of CBR Anisotropies.....	15
Figure 2.5: Single Differencing Power Transfer Function	16
Figure 2.6: Variation of Power Transfer Function with Beam Size	17
Figure 2.7: Double and Triple Differencing Power Transfer Functions.....	18
Figure 2.8: Sampling Autocovariance	20
Figure 2.9: Number of Regions	23
Figure 2.10: Switching Pattern	27
Figure 2.11: Sky Sampling Pattern	28
Figure 3.1: Rattlesnake Mountain	32
Figure 3.2: Battelle Millimeter Telescope	33
Figure 3.3: Optical Arrangement of Telescope	35
Figure 3.4: Optical Geometry of Beam Switching	38
Figure 3.5: Primary Mirror.....	40
Figure 3.6: Relative Efficiency of Imperfect Telescope.....	42
Figure 3.7: Nutation Mechanism	44
Figure 3.8: Pointing Measurements.....	49
Figure 3.9: Star Distribution	50
Figure 3.10: Pointing Residuals vs. Azimuth, February 20, 1986	51
Figure 3.11: Pointing Residuals vs. Azimuth, February 20, 1986	52

Figure 3.12: Pointing Residuals February 20, 1986	53
Figure 3.13: Pointing Residuals vs. Azimuth, March 13, 1986	54
Figure 3.14: Pointing Residuals vs. Elevation, March 13, 1986	55
Figure 3.15: Pointing Residuals, March 13, 1986	56
Figure 3.16: Effective Integration Time	60
Figure 4.1: Lunar Focussing	65
Figure 4.2: Focussing with Saturn	67
Figure 4.3: Drift Scans of Saturn	68
Figure 4.4: Lunar Brightness Temperature	71
Figure 4.5: Atmospheric Noise Reduction	76
Figure 4.6: Switching and Wobbling Patterns	77
Figure 4.7: Power Transfer Function	78
Figure 4.8: Sampling Autocovariance	79
Figure 4.9: Sky Sampling Pattern	81
Figure 5.1: Window Used in Shaving Procedure	83
Figure 5.2: Preliminary Analysis of data of March 20, 1986.	86
Figure 5.3: Preliminary Analysis of data of April 3, 1986.	87
Figure 5.4: Preliminary Analysis of data of April 6, 1986.	88
Figure 5.5: Preliminary Analysis of data of April 7, 1986.	89
Figure 5.6: Preliminary Analysis of data of April 8, 1986.	90
Figure 5.7: Calibrated Data for all Nights	92
Figure 5.8: The Fractional Temperature Difference	93
Figure A.1: Optical Arrangement	112
Figure A.2: Secondary Mirror Nutation Mechanism	114
Figure A.3: Dynamic Model of Nutation Mechanism	121
Figure A.4: Open Loop Frequency Response	124

Figure A.5: Block Diagram of Control System	127
Figure A.6: Transfer Functions of Control System Elements	128
Figure A.7: Closed Loop Frequency Response	130
Figure A.8: Response to Square Wave Input	131
Figure A.9: Response to Tailored Input Waveform	132
Figure A.10: Position Switching with Tailored Input Waveform	133
Figure B.1: Cross Section of the Cryostat	136
Figure B.2: Top View of Cryostat	137
Figure B.3: Detail of Evaporation Refrigerator Mounting	138
Figure B.4: Photometer Optical Elements	143

List of Tables

	<i>Page</i>
Table 2.1: Receiver Comparison	11
Table 3.1: Optical Parameters	34
Table 3.2: Mount Imperfection Model	47
Table 3.3: Pointing Performance.....	57
Table 4.1: System Calibrations and Atmospheric Opacity	73
Table 4.2: Saturn Observations of February 8, 1986.....	75
Table 5.1: Results of Hypothesis Test.....	95
Table 6.1: Model Predictions	98
Table A.1: Optical Parameters	113
Table A.2: Nutation Mechanism Dynamic Parameters	120
Table A.3: Control System Parameters	129
Table B.1: Spectral Filters	144

List of Plates

	<i>Page</i>
Plate I: Battelle Millimeter Wave Facility.....	30
Plate II: Rattlesnake Mountain.....	30
Plate III: Telescope Brake.....	46
Plate B.I: Manufacture of Compound Parabolic Concentrators.....	142

Acknowledgements

This project would not have been possible without *l'amici dei amici*, both here and there. I received fellowship support from the Department of Energy through the NORCUS program and from the ARCS foundation, for which I am grateful. Ron Severtsen, Walt Siegmund, Heinz Guldenmann, Dick Davisson, Phil Eckstrom, Steve McCandliss, Doug Johnson, Dave Forbush, and Fritz Toeves all contributed ideas, time, and material toward making things work. Vanessa Lutey's moral support was invaluable.

Chapter 1. Introduction

Ever since its discovery in 1965,¹ the cosmic background radiation (CBR) has been interpreted as a relic that provides direct evidence of physical conditions during a hot, highly condensed phase in the universe's early history – the “hot big bang”.^{2,3} Two of the CBR's properties are of fundamental consequence: it has a thermal Planck spectrum with a temperature of 2.75 K,^{4,5,6} and aside from a dipole distortion attributable to the earth's peculiar motion, the CBR intensity is isotropic to better than 10^{-4} on all angular scales.⁷ The observed spectrum of the CBR implies a state of thermal equilibrium existed until the epoch of decoupling, when the universe became transparent following the formation of atomic hydrogen. Moreover, the observed isotropy of the CBR implies that the mass density and temperature were virtually the same everywhere. Neither of these conclusions are apparent from the nature of the present universe, which is neither in equilibrium, nor uniform in density on any observable scale size.⁸

The high degree of CBR isotropy is the most direct support for inflationary cosmological models.⁹ In the standard scenario, without inflation, the big bang would have had to have been a highly symmetric event to produce the observed isotropy, since areas in the sky separated by more than 3° were not causally connected until after decoupling. Inflation theories posit a symmetry breaking phase transition in the very early universe when an elementary scalar field is temporarily in a metastable false vacuum state with a large potential energy. During the rather long time it takes this field to evolve to the zero potential true vacuum, the false vacuum energy drives an exponential (de Sitter) expansion of the universe. By allowing the entire observable universe to have been in causal contact before the inflationary epoch, this mechanism naturally predicts a high degree of uniformity in the postinflation universe. Furthermore, inflation enlarges the scale factor

enough that any pre-existing spatial curvature is now undetectable. This implies the present universe is spatially flat, with the ratio of present density to the closure density $\Omega \equiv 1$.

The universe does not become completely uniform following the inflationary episode, however, as quantum fluctuations in the scalar field driving inflation generate postinflation temperature and density perturbations.^{10,11} Although the predicted amplitude of these perturbations is quite sensitive to the detailed shape of the scalar field potential, the perturbations are expected to have a scale invariant, Zel'dovich¹² spectrum, regardless of the potential.⁹ The presence of these perturbations during the decoupling era gives rise to CBR anisotropies that are observable in the present epoch.

To estimate the properties of CBR anisotropies, dynamic models may be used to calculate the growth of the perturbations from the end of the inflationary epoch through decoupling, and the perturbation amplitude may be normalized to the large scale galaxy distribution observed in the present universe.^{13,14} These calculations depend on the composition of the matter in the universe and two global properties of the universe: its spatial curvature and its age, expressed through Ω and the Hubble parameter, $H_0 = 100h \text{ km s}^{-1} \text{ Mpc}^{-1}$, respectively. Specifically, these studies predict smaller amplitude CBR anisotropies in the background for higher density (larger Ω) and more compact (larger h) models. Because the values of these parameters are only poorly known, the problem must be turned around: given the observed limits on CBR anisotropies, what models are ruled out or what constraints can we place on these universal parameters?¹⁵

Previously published upper limits on the amplitude of small angular scale CBR anisotropies¹⁶ have already restricted the acceptable range of parameters (fig. 1.1). Baryon and massive neutrino dominated universes with a current mass density

much less than the closure density, $\Omega \ll 1$, are generally disfavored by these observations.^{13,17} Moreover, it is unlikely that reheating the intergalactic medium subsequent to decoupling could have washed out the anisotropies.¹³ Since a baryon dominated universe with $\Omega \simeq 1$ is ruled out by the observed primordial abundance of helium,¹⁸ it seems probable that most of the mass of the universe is in a form not readily observed. Furthermore, numerical simulations of a universe dominated by cold dark matter indicate that if the clustering properties of the observed galaxies are the same as the clustering properties of the overall mass distribution, the observed peculiar velocity distribution of the galaxies is inconsistent with high density models.¹⁹ If, on the other hand, galaxies only formed in the highest density fluctuations, then the clustering of galaxies would be stronger than the clustering of the overall mass distribution and high density models could be accommodated.²⁰

The possibilities that the dominant form of matter in the universe is nonbaryonic, or that the distribution of galaxies in the universe is not the same as the overall distribution of the mass are strong statements about the structure and history of the universe. From these, it is clear that observations of small-scale anisotropies in the CBR can reveal fundamental new information about the universe, and this has motivated the experimental effort described in these pages.

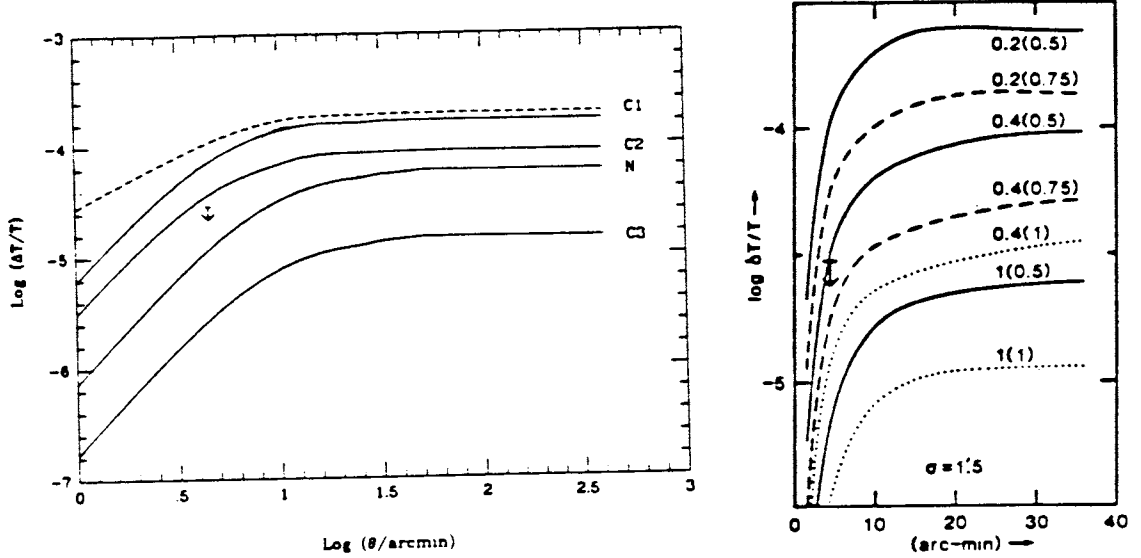


Figure 1.1. Predictions of the amplitude of CBR anisotropies, expressed as a fractional temperature change, $\Delta T/T$, for a universe dominated by cold non-interacting particles. On the left, from Bond and Efstathiou,¹³ are the following models: (C1) $\Omega = 0.2$, $h = 0.5$; (C2) $\Omega = 0.2$, $h = 0.75$; (C3) $\Omega = 1.0$, $h = 0.75$. (N) is a universe dominated by heavy neutrinos with $\Omega = 1.0$, $h = 0.75$. All models have a baryon mass of $\Omega_b = 0.03$. The data point is the upper limit of Uson and Wilkinson.¹⁶ On the right are the predictions of Vittorio and Silk¹⁴ with Ω and h given on each model line. Both of these plots are for three position double difference observations with a $1.5'$ beam as a function of beam switching angle. Although the experiment described in this work used triple differencing on a $10'$ scale with a $4'$ beam, these differences in experimental details do not alter the expected anisotropy signal significantly.

Chapter 2. Experimental Design

Because of the cosmological implications of CBR anisotropies, this experiment's goal was to determine the amplitude of fine angular scale CBR brightness fluctuations. For sampling these fluctuations, the basic strategy is to measure the difference in radiation intensity between a set of closely spaced spots in one region of the sky. This procedure is accomplished by pointing a telescope back and forth rapidly between the spots and synchronously demodulating the output of a detector placed at the focus of the telescope. If this difference is measured in several independent sky regions, the variance of the measurements between regions then reveals either the amplitude of CBR anisotropies that are detected, or an upper limit to their amplitude, if none are detected.

In the experimental design, details of sampling strategies and detector properties were considered in the context of the characteristics of CBR anisotropies and of the various noise sources that can obscure the anisotropy signal. A quantitative standard for comparing possible experimental configurations is the signal to noise ratio. This chapter discusses the dependence of that ratio on the values chosen for the design parameters.

Operating Wavelength

To determine the best wavelength for these observations, the expected signal's spectral signature must be considered, together with the spectra of non-cosmological anisotropies, the transparency of the atmosphere, and the properties of the various detectors that operate at different wavelengths.

Spectral signature: The thermal character and temperature, $T_{\text{CBR}} = 2.75 \text{ K}$, of the CBR spectrum have been verified by observations at wavelengths in the range $75 \text{ cm} \leq \lambda \leq 300 \mu\text{m}$.²¹ Perturbing the temperature in the Planck spectrum, $B_\lambda = 2hc^2/\lambda^5 (e^x - 1)^{-1}$, where $x = hc/\lambda k_B T_{\text{CBR}}$, yields the differential brightness, δB_λ that describes primordial fluctuations in the CBR temperature (fig. 2.1),

$$\delta B_\lambda = B_\lambda \frac{x e^x}{e^x - 1} \frac{\delta T}{T_{\text{CBR}}}. \quad 2.1$$

All other things being equal, then, the best wavelength for anisotropy measurements is the peak of this spectrum, $\lambda = 0.8 \text{ mm}$, where the radiation power is greatest.

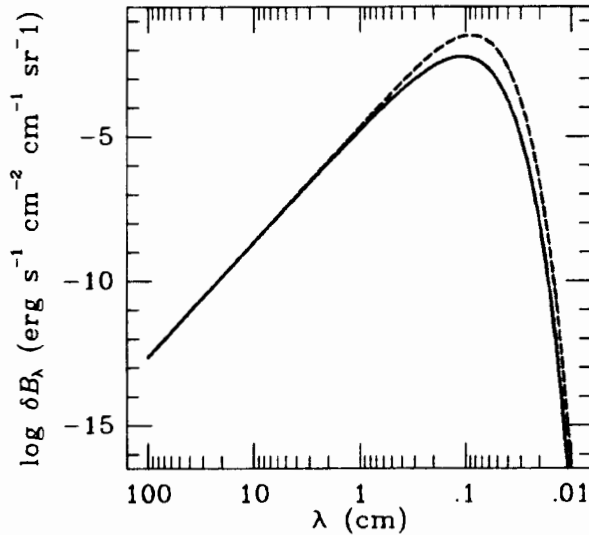


Figure 2.1. The differential brightness spectrum of primordial CBR anisotropies, $\delta B_\lambda / (\delta T / T_{\text{CBR}})$ (dashed curve), and the Planck spectrum of the CBR, B_λ (solid curve).

Because microwave receivers are commonly calibrated in terms of the Rayleigh-Jeans equivalent brightness temperature at their operating wavelengths, it is convenient to express the differential brightness spectrum similarly. The equivalent

Rayleigh-Jeans brightness temperature of the CBR is $T_B(x) = T_{\text{CBR}}x/(e^x - 1)$, and the differential brightness temperature of temperature fluctuations is (fig. 2.2)

$$\delta T_B(x) = T_{\text{CBR}} \frac{x^2 e^x}{(e^x - 1)^2} \frac{\delta T}{T_{\text{CBR}}}. \quad 2.2$$

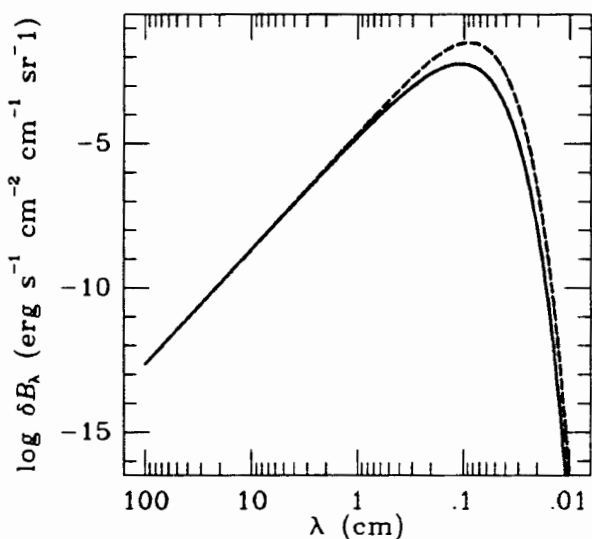


Figure 2.2. The Rayleigh-Jeans equivalent brightness temperatures of the CBR, $T_B(\lambda)$ (solid curve), and of primordial anisotropies, $\delta T_B(\lambda)/(\delta T/T_{\text{CBR}})$ (dashed curve).

Non-cosmological anisotropies: The two principle *celestial* backgrounds that could mimic CBR anisotropies are discrete radio sources and thermal emission by Galactic dust. This last is so even though the observations were made at the north celestial pole which, at $b \approx 25^\circ$, is well out of the Galactic plane. Their joint contribution is at a minimum at millimeter wavelengths, and recent studies^{22,23} indicate $\delta T_{\text{cel}}/T_{\text{CBR}} < 3 \times 10^{-6}$. Based on an emission measure²⁴ less than 4 cm^{-6} pc for $|b| > 20^\circ$, anisotropies in Galactic free-free emission are apparently less than 10^{-6} .

Atmospheric Limitations: Both of the above paragraphs indicate clear advantages to observing at millimeter wavelengths, but for ground-based observations, there is a drawback to this band, the emission from the atmosphere is more severe than at longer wavelengths. Emission from oxygen and water vapor are the strongest contributors to the sky background. Figure 2.3 shows the antenna (brightness) temperature of the sky calculated from an atmosphere model with 1 mm and with 3 mm precipitable water vapor.²⁵ In that figure, the line at 6 cm^{-1} and most of the lines above 10 cm^{-1} are due to water vapor. These spectra indicate three possible observing windows: at 3, 5, and 8 cm^{-1} . The 8 cm^{-1} band is bracketed by water lines and is in the wings of the 20 cm^{-1} water vapor complex, so fluctuations in atmospheric transparency should be worse than at lower frequencies.

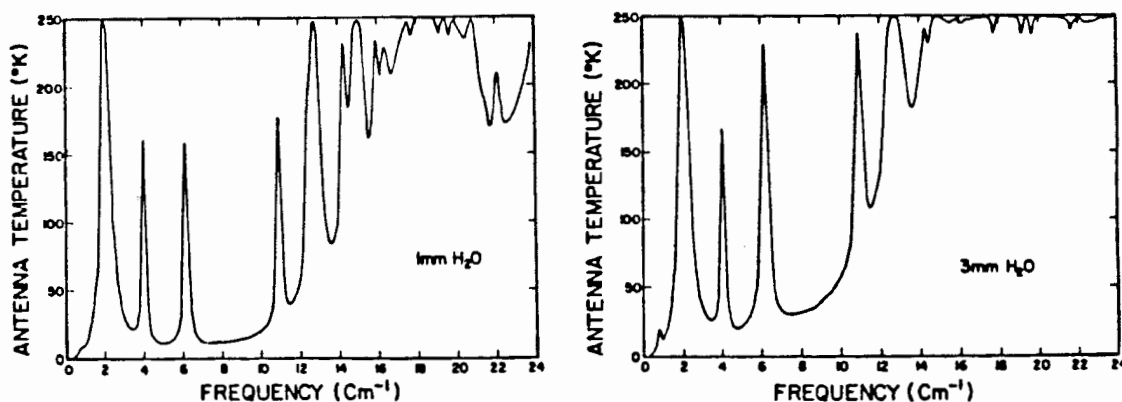


Figure 2.3. A model of the sky antenna temperature as a function of frequency for two values of precipitable H₂O. Oxygen lines are at 2, 4, 13, 15, 17 cm^{-1} , and the other lines are water vapor.

Detector properties: Detectors of microwave radiation fall into two general categories: single mode, phase coherent receivers and multimode, phase incoherent bolometers. Currently, the most sensitive phase coherent receivers are superheterodyne receivers employing as a first stage either a maser amplifier, at centimeter wavelengths, or a superconductor-insulator-superconductor (SIS) mixer, at millimeter wavelengths. The most sensitive multimode detectors are cryogenically cooled semiconductor bolometers, operated at millimeter and submillimeter wavelengths. In the succeeding paragraphs, three instruments representative of these technologies are compared to determine their suitability for observations of CBR anisotropies. This comparison, summarized in table 2.1, considers the ratio of anisotropy signal to the measured system noise, including the atmospheric contribution, for each instrument.

Fine scale anisotropies in the CBR temperature form a time invariant pattern of sky brightness fluctuations, so the temperature in any direction, $\hat{\mathbf{q}}$, can be written $T(\hat{\mathbf{q}}) = T_{\text{CBR}} + \delta T(\hat{\mathbf{q}})$. Here T_{CBR} is the mean CBR temperature and δT is a zero mean random variable that describes the temperature fluctuations. If the temperature difference between two infinitesimal spots, $\Delta T^{(1)} = T(\hat{\mathbf{q}}_1) - T(\hat{\mathbf{q}}_2)$, is measured in several sky regions, then the mean temperature difference will be zero, but the variance of the temperature difference between regions will characterize the brightness fluctuations, $\text{var}(\Delta T^{(1)}) = 2 \text{var}(\delta T)$.

In terms of a fractional change in the CBR temperature, the equivalent input noise of a square wave modulated, Dicke-switched receiver is²⁶

$$\text{var} \left(\frac{\Delta T_N^{(1)}}{T_{\text{CBR}}} \right) = \left[\frac{x^2 e^x}{(e^x - 1)^2} T_{\text{CBR}} \right]^{-2} \frac{4T_{\text{rec}}^2}{\eta^2 \Delta \nu t} \equiv \sigma_{\text{rec}}^2 / t, \quad 2.3$$

where T_{rec} is the receiver noise temperature, η is the telescope efficiency, $\Delta\nu$ is the predetection bandwidth, $x = hc/\lambda k_B T_{\text{CBB}}$, and t is the integration time. Then for this measurement the ratio of signal and noise variances is

$$\frac{S}{N} = \beta_1 \frac{\text{var}(\delta T/T_{\text{CBB}})}{\sigma_{\text{rec}}^2} t, \quad 2.4$$

where the sampling coefficient, $\beta_1 = 2$, indicates the coupling between the sampling pattern and the CBB anisotropies.

A further level of differencing may be necessary to overcome atmospheric and instrumental effects (see below). If this second difference is defined as

$$\begin{aligned} \Delta T^{(2)}(\hat{\mathbf{q}}_1, \hat{\mathbf{q}}_2, \hat{\mathbf{q}}_3) &\equiv \frac{1}{2} [\Delta T^{(1)}(\hat{\mathbf{q}}_1, \hat{\mathbf{q}}_2) - \Delta T^{(1)}(\hat{\mathbf{q}}_2, \hat{\mathbf{q}}_3)] \\ &= \frac{1}{2} T(\hat{\mathbf{q}}_1) - T(\hat{\mathbf{q}}_2) + \frac{1}{2} T(\hat{\mathbf{q}}_3), \end{aligned} \quad 2.5$$

then the anisotropy signal is $\text{var}(\Delta T^{(2)}) = \frac{3}{2} \text{var}(\delta T)$. With this normalization, the receiver noise is the same as in single differencing, $\text{var}(\Delta T_N^{(2)}/T_{\text{CBB}}) = \sigma_{\text{rec}}^2/t$, so the sampling coefficient is $\beta_2 = 3/2$.

In order to measure $\text{var}(\Delta T)$ it is necessary, of course, to observe more than one sky region. Below it is shown that for setting a 95% confidence level upper limit on $\text{var}(\Delta T)$, the most efficient number of regions is about ten, and in that case the expected upper limit is 15 times the variance expected from receiver noise if one region were observed for the entire integration interval. This determines the signal to noise ratio, $S/N = 15$, required to set such a limit.

Models of CBB anisotropies^{27,28} are significantly constrained by observations at a level of $\delta T/T_{\text{CBB}} \simeq 5 \times 10^{-5}$. The following receiver comparison was made,

Table 2.1. Receiver Comparison

Instrument	λ or ν	σ_{rec} ($10^{-3}\sqrt{\text{s}}$)	β	t
NRAO K band maser	20 GHz	12.0	3/2	160 hr
Generic SIS	90 GHz	9.6	3/2	100 hr
Bolometer	2.2 mm	8.6	5/4	110 hr

therefore, by solving equation 2.4 for the integration time necessary to set an upper limit at this level with each receiver.

Recently, Uson and Wilkinson²⁹ made measurements of the CBR with a K-band maser receiver at the National Radio Astronomy Observatory's 40 m telescope in Green Bank, West Virginia. They reported an effective double sideband (DSB) receiver noise temperature of $T_{\text{rec}} \simeq 115$ K, at a center frequency of $\nu_0 = 19.5$ GHz, with a predetection bandwidth $\Delta\nu = 370$ MHz, and a telescope efficiency $\eta = 55\%$. Second differencing was accomplished through a combination of secondary mirror nutation at 3 Hz and telescope wobbling every 5 min, so the appropriate sampling coefficient is $\beta_2 = 3/2$. Blanking during secondary mirror movement excluded 53% of the total observing time and a further 5% was excluded during telescope wobble motion. From equation 2.2, the brightness temperature of CBR anisotropies at 20 GHz is $\delta T_B = 2.7(\delta T/T_{\text{CBR}})$ K. Combining all these factors gives a receiver noise level of

$$\sigma_{\text{maser}}^2 = [(0.95)(0.47)]^{-1} \frac{4T_{\text{rec}}^2}{\eta^2 \Delta\nu (2.7 \text{ K})^2} = (12.0 \times 10^{-3} \sqrt{\text{s}})^2, \quad 2.6$$

and the necessary integration time is

$$t_{\text{maser}} = \frac{\sigma_{\text{maser}}^2}{(\delta T/T_{\text{CBR}})^2} \frac{S/N}{\beta_2} \approx 160 \text{ hrs} \quad 2.7$$

Notice that increasing the slew rate of the NRAO mirror nutation system could substantially reduce this observing period, both by decreasing the blanking percentage and by allowing modulation at a higher frequency, where $1/f$ noise in the maser is less severe.

SIS receivers are currently under development at a number of laboratories.³⁰ For comparison purposes a “generic” instrument can be considered, operating at frequency of $\nu_0 = 90$ GHz, with a bandwidth of $\Delta\nu = 1$ GHz, a DSB noise temperature of $T_{\text{rec}} = 150$ K, and a telescope efficiency of 50%. At this frequency, $\delta T_B = 2.2(\delta T/T_{\text{CMB}})$ K. If double differencing is used and the blanking can be kept to 20%, the receiver noise level is $\sigma_{\text{SIS}} = 9.6 \times 10^{-3} \sqrt{s}$ and the required integration time is $t_{\text{SIS}} \approx 100$ hrs. In addition to being very expensive, however, SIS receivers are only just beginning to emerge from the laboratory and be used for astronomical observations. In the absence of demonstrated performance over long integration times, therefore, this must be considered as a lower limit on the integration time.

At the short operating wavelength, $\lambda = 2.2$ mm, and with the wide bandwidth, $\Delta\lambda = 0.25$ mm, of the bolometer used in this experiment (Appendix B), triple differencing was necessary to reduce the effects of atmospheric noise to a negligible level (see below). This triple difference was composed of high frequency, double difference beam switching, accomplished through nutation of the telescope’s secondary mirror, and low frequency, single difference wobbling of the telescope structure. If the third difference is defined as

$$\begin{aligned} \Delta T^{(3)}(\hat{\mathbf{q}}_1, \dots, \hat{\mathbf{q}}_4) &= \frac{1}{2} \left[\Delta T^{(2)}(\hat{\mathbf{q}}_1, \hat{\mathbf{q}}_2, \hat{\mathbf{q}}_3) - \Delta T^{(2)}(\hat{\mathbf{q}}_2, \hat{\mathbf{q}}_3, \hat{\mathbf{q}}_4) \right] \\ &= \frac{1}{4} T(\hat{\mathbf{q}}_1) - \frac{3}{4} T(\hat{\mathbf{q}}_2) + \frac{3}{4} T(\hat{\mathbf{q}}_3) - \frac{1}{4} T(\hat{\mathbf{q}}_4), \end{aligned} \quad 2.8$$

then the receiver noise level is numerically the same as for single differencing, $\text{var}(\Delta T_N^{(3)}/T_{\text{CMB}}) = \sigma_{\text{rec}}^2/t$, and the sampling coefficient is $\beta_3 = 5/4$. At this

wavelength, $\delta T_B = 1.7(\delta T/T_{\text{CBR}})$ K. When referred above the atmosphere, the measured noise level on the clearest nights was $\sigma_{\text{rec}} = 8.6 \times 10^{-3} \sqrt{s}$, including the nutation slew time (Chapter 4). Then the necessary integration time, including a 10% allowance for blanking during telescope wobbling, is $t_{\text{bol}} = 110$ hrs. This comparison shows a millimeter wavelength bolometer is a good choice for observing CBR anisotropies.

Angular Scale

In the preceding discussion, the sampling coefficient was introduced to express the effect of different sampling patterns on the expected signal to noise ratio. It was defined under the assumptions that the CBR anisotropies are uncorrelated on the angular scale of the sampling, and that the spots on the sky have infinitesimal area. In practice, however, neither assumption holds. The nature of the decoupling era correlates fluctuations on small angular scales, setting a lower bound to the useful sampling scale, and observing practicalities mandate the use of finite area spots.

By generalizing the definition of the sampling coefficient to include these factors, their effect on an experiment may be estimated. Formally, this is done by describing the CBR anisotropies by their correlation function, $C_{\text{CBR}}(\theta)$, and the sampling pattern by its autocovariance, $C_s(\theta)$. Then the signal variance is³¹

$$\text{var}(\Delta T_{\text{CBR}}^{(s)}) = \int d^2\theta C_{\text{CBR}}(\theta) C_s(\theta), \quad 2.9$$

and the sampling coefficient can be defined as

$$\beta_s = \frac{\text{var}(\Delta T_{\text{CBR}}^{(s)})}{C_{\text{CBR}}(\theta = 0)}. \quad 2.10$$

Under the assumptions of uncorrelated anisotropies and infinitesimal spots this reduces to the previous definition.

Angular Correlation: Even if the spatial spectrum of primordial density perturbations is assumed scaleless, the finite duration of the decoupling era imposes a correlation on observable CBR anisotropies at small angular scales. Although its precise nature is model dependent, the general properties of this correlation are apparent from consideration of photon scattering during decoupling.

The probability that a photon of the CBR was last scattered at a given redshift, z , is approximated well by^{32,33}

$$P(z) = (\sqrt{\pi}\sigma_z)^{-1} \exp[-(z - z_{\max})^2/\sigma_z^2], \quad 2.11$$

where $z_{\max} \simeq 1055$, and $\sigma_z \simeq 75$. A perturbation with a linear size equal to the comoving thickness of the last scatter shell, $2\sigma_x = 2\sigma_z c/H_0(z_{\max}^3\Omega)^{-1/2}$, subtends an angle,

$$2\sigma_\theta = 2\sigma_x \frac{H_0\Omega}{2c} = \sigma_z z_{\max}^{-3/2} \Omega^{1/2} = 7.6' \Omega^{1/2}, \quad 2.12$$

if observed from the current epoch. On smaller angular scales, more than one independent perturbation will be present along the line of sight and the intensity fluctuations will be correlated because of the consequent averaging.

The angular correlations produced by this mechanism in several typical models are shown in figure 2.4. Since the effect of these correlations is to reduce the signal, $\text{var}(\Delta T)$, these models indicate an experiment designed to detect anisotropies should sample the sky on scales $\geq 10'$, where the correlations are small.

Variations in atmospheric emission and transparency place an upper limit, albeit ill-defined, on the angular scale amenable to investigation with ground based

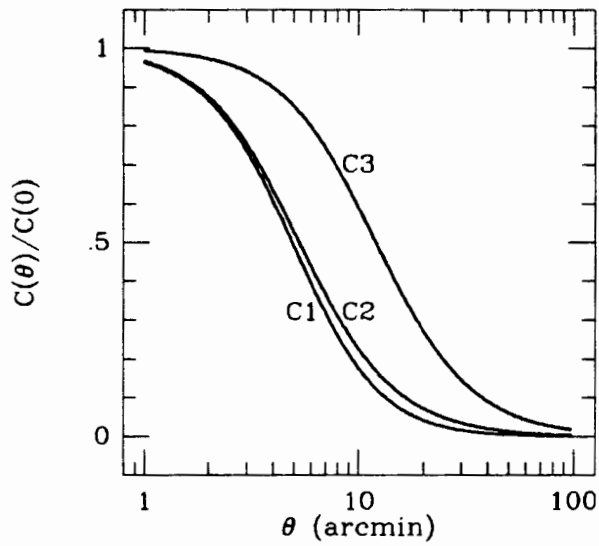


Figure 2.4. Predictions of the angular correlations of CBR brightness fluctuations in a cold dark matter dominated universe.²⁷ (C1: $\Omega = 0.2$, $h = 0.5$; C2: $\Omega = 0.2$, $h = 0.75$; C3: $\Omega = 1.0$, $h = 0.75$)

instruments. The spatial power spectrum of this atmospheric noise, discussed below, is quite red, favoring measurements at small angular scales. Based on these considerations, the apparatus was designed to be capable of investigating angular scales up to $\theta_s \simeq 15'$, and the beam switching angle actually used for observations was determined on the basis of photometric measurements of the sky noise.

Beam Size: An idealized differencing experiment would measure the change in intensity between two spots of infinitesimal area in the sky, but in practice, of course, the telescope beam size is finite. Furthermore, the optical throughput, and therefore the received power from an extended source, are proportional to the beam solid angle for a multimode, phase incoherent detector, such as our bolometer, so a large beam size is desirable to achieve a maximum signal to noise ratio. If the beam's angular diameter is comparable to the switching angle, however, the experiment's response at the switching scale will be reduced. The beam switching pattern defines a spatial power filter, and the extent of the sensitivity reduction may be determined

from the variation of this filter's power transfer with the ratio of beam width to switching angle.

Consider a telescope beam pattern that is approximated by a two dimensional Gaussian profile $P_b(\theta) = (4 \ln 2 / \pi \theta_b^2) \exp(-4 \ln 2 \theta^2 / \theta_b^2)$, where θ_b is the full width at half maximum (FWHM). If this beam is switched between two positions separated by an angle θ_s , the beam switching pattern can be written as $P_s(\theta) = \delta(\theta_y) [\delta(\theta_x - \theta_s/2) - \delta(\theta_x + \theta_s/2)]$, where θ_x and θ_y are Cartesian components of θ aligned with the switching direction. Then the two dimensional Fourier transform of the beam profile is $\mathcal{F}_b(k) = (2\pi)^{-1} \exp(-k^2 \theta_b^2 / 16 \ln 2)$, and the transform of the switching pattern is $\mathcal{F}_s(k) = (i/\pi) \sin(k_x \theta_s / 2)$. Here k is the spatial frequency conjugate to θ . The sampling pattern's power transfer function, illustrated in figure 2.5, is the squared product of these transforms

$$\tau_s(k) = |2\pi \mathcal{F}_b \mathcal{F}_s|^2 = \pi^{-2} \sin^2(k_x \theta_s / 2) \exp(-k^2 \theta_b^2 / 8 \ln 2). \quad 2.13$$

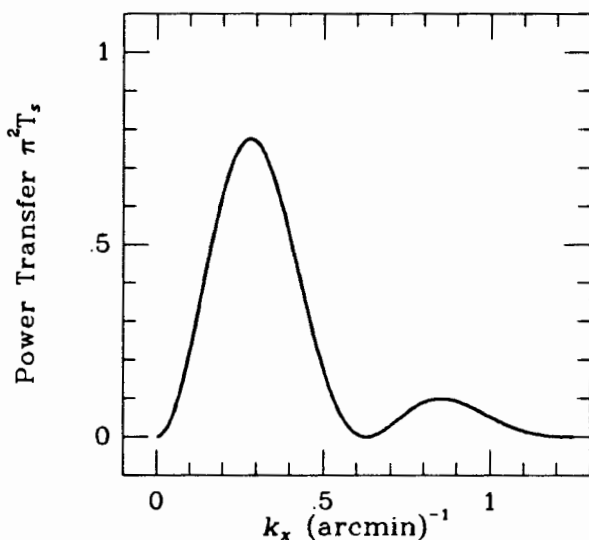


Figure 2.5. The power transfer function defined by two position switching (single differencing) with a Gaussian telescope beam. This is the component in the switching direction with a beam diameter (FWHM) $\theta_b = 4'$ and a switching angle $\theta_s = 10'$.

In the switching direction, the maximum transfer occurs at the first nonzero root of

$$\cot(k_x \theta_s / 2) - \frac{k_x \theta_b^2}{4 \theta_s \ln 2} = 0, \quad 2.14$$

and figure 2.6 shows the transfer function amplitude at this maximum as a function of θ_b/θ_s . From this figure, it is apparent the signal amplitude would be significantly reduced if $\theta_b/\theta_s \geq 0.5$. Based, therefore, on a design range of $\theta_s \geq 10'$ and the condition of the telescope optics (Chapter 3), a beam size $\theta_b \simeq 4'$ was chosen. For these values, the maximum transfer occurs at $k_x \approx 0.28 \text{ arcmin}^{-1}$.

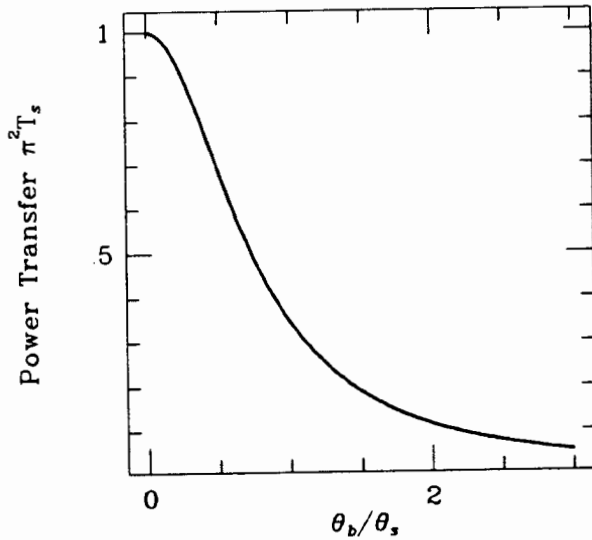


Figure 2.6. The variation with the ratio of the beam size to the switching angle, θ_b/θ_s , of the maximum power transfer of the filter defined by two position switching with a Gaussian telescope beam.

The merits of higher order differencing schemes are discussed below in the section on sampling strategies. Since successive convolutions of the two position beam switching pattern of single differencing will generate the higher order switching patterns, the power transfer function defined by n th order differencing is just:

$$\tau_{p,n}(k) = \pi^{-2} \sin^{2n}(k_x \theta_s / 2) \exp(-k^2 \theta_b^2 / 8 \ln 2). \quad 2.15$$

This filter's maximum transfer is at the first root of

$$n \cot(k_x \theta_s / 2) - \frac{k_x \theta_b^2}{4 \theta_s \ln 2} = 0, \quad 2.16$$

which approaches $k_x = \pi / \theta_s$ as $n \rightarrow \infty$. The resulting constraint on θ_b / θ_s is essentially the same as in the single differencing case. Figure 2.7 illustrates the power transfer functions for double and triple differencing (three and four position switching).

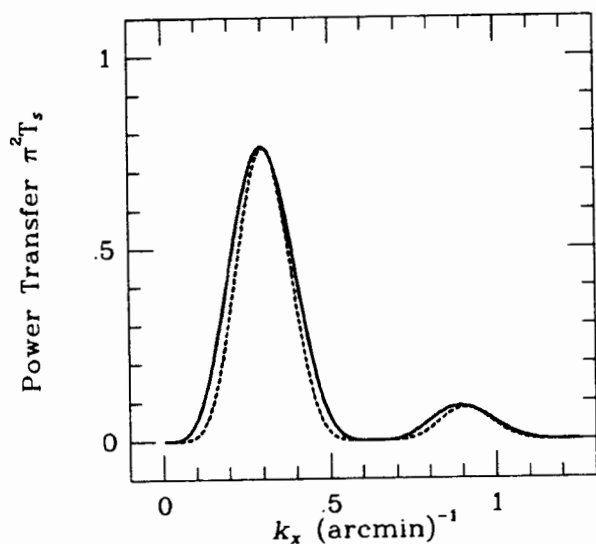


Figure 2.7. The power density filter defined by three position (double differencing; solid curve) and four position (triple differencing; dashed curve) beam switching with a Gaussian telescope beam. This is the component in the switching direction with a beam diameter (FWHM) $\theta_b = 4'$ and a switching angle $\theta_s = 10'$.

Sampling Coefficient: By evaluating the integral in equation 2.9, the effects of angular correlations in the CBR anisotropies and of finite beam area may be included in the sampling coefficient, β_s . The sampling pattern's spatial autocovariance is the Fourier transform of its power transfer function,

$$C_s(\theta) = \int_{-\infty}^{\infty} d^2k e^{-ik\theta} \tau_s(k). \quad 2.17$$

For n th order differencing with a Gaussian beam profile (eqn. 2.15), this autocovariance is (fig. 2.8)

$$C_n(\theta) = 2^{2(1-n)} \frac{2 \ln 2}{\pi \theta_b^2} \sum_{j=-n}^n (-1)^j \binom{2n}{n-j} \exp \left\{ - \left[\theta_y^2 + (\theta_x - j\theta_s)^2 \right] \frac{2 \ln 2}{\theta_b^2} \right\}, \quad 2.18$$

and for a cylindrically symmetric CBR correlation function the sampling coefficient is

$$\begin{aligned} \beta_n &= 2^{2(2-n)} \frac{\ln 2}{\theta_b^2} \sum_{j=-n}^n (-1)^j \binom{2n}{n-j} \\ &\times \int_0^\infty \theta d\theta \frac{C_{\text{CBR}}(\theta)}{C_{\text{CBR}}(0)} \exp \left[-(\theta^2 + j^2 \theta_s^2) \frac{2 \ln 2}{\theta_b^2} \right] I_0 \left(4j\theta\theta_s \frac{\ln 2}{\theta_b^2} \right), \quad 2.19 \end{aligned}$$

where I_0 is a Bessel function.

In the limit of delta function beams, the autocovariance reduces to

$$C_n(\theta) = 2^{2(1-n)} \delta(\theta_y) \sum_{j=-n}^n (-1)^j \binom{2n}{n-j} \delta(\theta_x - j\theta_s), \quad 2.20$$

and the sampling coefficient is

$$\beta_{n,\delta} = 2^{2(1-n)} \sum_{j=-n}^n (-1)^j \binom{2n}{n-j} C_{\text{CBR}}(j\theta_s) / C_{\text{CBR}}(0), \quad 2.21$$

or

$$\beta_{n,\delta} = 2^{2(1-n)} \binom{2n}{n}, \quad 2.22$$

under the assumption the anisotropies are uncorrelated, $C_{\text{CBR}}(\theta) = (\delta T / T_{\text{CBR}})^2 \times \delta(\theta)$. For single, double, and triple differencing, this is $\beta_{1,\delta} = 2$, $\beta_{2,\delta} = 3/2$, and $\beta_{3,\delta} = 5/4$, respectively.

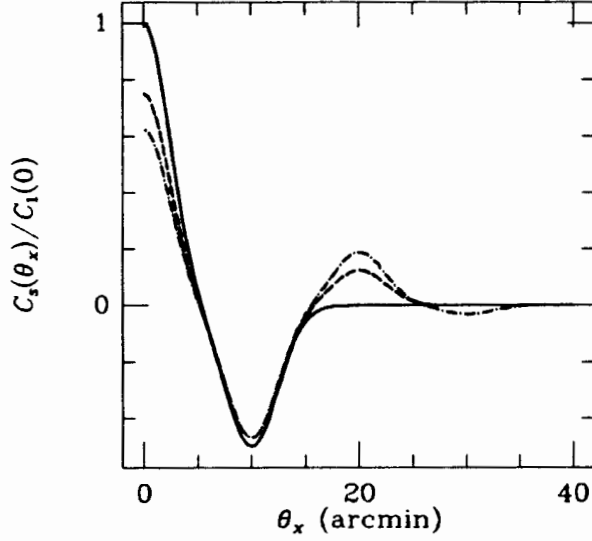


Figure 2.8. The spatial autocovariance of single, double and triple differencing with Gaussian beam profiles (solid, dashed, and dash-dotted curves, respectively). This is the component in the switching direction with a beam diameter (FWHM) $\theta_b = 4'$ and a switching angle $\theta_s = 10'$.

It is instructive to consider further the case of correlated anisotropies using a model where the correlation function has a Gaussian profile with FWHM diameter $\sqrt{2}\theta_{\text{CBR}}$,

$$C_{\text{CBR}}(\theta) = (\delta T/T_{\text{CBR}})^2 \frac{2 \ln 2}{\pi \theta_{\text{CBR}}^2} \exp \left[-\frac{2\theta^2 \ln 2}{\theta_{\text{CBR}}^2} \right]. \quad 2.23$$

Then the sampling coefficient is

$$\beta_n = 2^{2(1-n)} \sum_{j=-n}^n (-1)^j \binom{2n}{n-j} \frac{\theta_{\text{CBR}}^2}{\theta_b^2 + \theta_{\text{CBR}}^2} \exp \left[-2j^2 \ln 2 \left(\frac{\theta_s^2}{\theta_b^2 + \theta_{\text{CBR}}^2} \right) \right]. \quad 2.24$$

If the switching angle is much smaller than the sum of the beam size and correlation angle, $\theta_s^2 \ll \theta_b^2 + \theta_{\text{CBR}}^2$, then all the exponential terms in this equation are approximately one and the sum vanishes. As expected, this gives low sampling efficiency. On the other hand, if $\theta_s^2 \gg \theta_b^2 + \theta_{\text{CBR}}^2$, only the $j = 0$ term contributes significantly to the sum, and two subcases may be distinguished. If $\theta_{\text{CBR}} < \theta_b$, the coefficient scales as $\theta_{\text{CBR}}^2/\theta_b^2$, and beam dilution reduces the sampling efficiency. The best

situation is $\theta_b \ll \theta_{\text{CBR}} \ll \theta_s$, in which case equation 2.24 reduces to equation 2.22, the simple case of uncorrelated fluctuations and delta function beams.

Number of Sky Regions

If no anisotropies are detected, determination of an upper limit on the amplitude of CBR anisotropies proceeds from statistical analysis of the variance of the measured brightness differences within an ensemble of sky regions (Chapter 5). Two constraints affect into this procedure: the number of independent regions, which determines the stability of the variance estimate, and the individual uncertainties in the measured brightness differences, which determine the magnitude of the variance estimate. These constraints present a dilemma in the situation of a finite total observing interval. If a small number of regions are observed, the integration time per region will be long, and the uncertainty in each brightness difference will be small, but the stability of the variance estimate will be low because of the small number of independent regions. Conversely, if a large number of regions are observed, the stability of the estimate will be high, but the uncertainty in each brightness difference will be large. Clearly, there must be a compromise between these two extremes that is optimal for determining a limit on the anisotropy amplitude. It turns out the optimal number of regions depends solely on the desired confidence level of the upper limit.

Let the expected results of observations of N sky regions be the measured brightness temperature differences, ΔT_r , and variances σ_r^2 , for $r = 1, \dots, N$. Boynton and Partridge³⁴ presented a statistic developed from consideration of the Neyman-Pearson lemma³⁵ to test the hypothesis that there is some excess variance component present in the data, $\hat{\sigma}^2 > 0$, against the hypothesis that there is no excess

variance $\hat{\sigma}^2 = 0$. That statistic is

$$S = \sum_r \frac{\Delta T_r^2}{\sigma_r^2(\sigma_r^2 + \hat{\sigma}^2)}. \quad 2.25$$

If $\mathcal{R} = \sum_r \sigma_r^{-2} / \sum_r \sigma_r^{-4}$, then the product, $\mathcal{R}S$, is distributed approximately as χ^2 on $\nu_{\text{eff}} = \mathcal{R} \sum_r \sigma_r^{-2}$ degrees of freedom. If the σ_r are determined by white receiver noise, $\mathcal{E}(\sigma_r^2) = \sigma_{\text{rec}}^2/(t/N)$, where t is the total observing time, the numerator and denominator of S are statistically independent. Then the ΔT_r should be normally distributed with zero mean, and the expectation value of the product $\mathcal{R}S$ is then

$$\mathcal{E}(\mathcal{R}S) = \frac{\sum_r 1/\mathcal{E}(\sigma_r^2)}{\sum_r 1/\mathcal{E}(\sigma_r^4)} \sum_r \frac{\mathcal{E}(\Delta T_r^2)}{\mathcal{E}(\sigma_r^4) + \hat{\sigma}^2 \mathcal{E}(\sigma_r^2)} = \frac{N^2}{N + \hat{\sigma}^2 t / \sigma_{\text{rec}}^2}, \quad 2.26$$

which can be solved for the signal to noise ratio,

$$\frac{\hat{\sigma}^2}{\sigma_{\text{rec}}^2/t} = N \left[\frac{N}{\mathcal{R}S} - 1 \right], \quad 2.27$$

since $\mathcal{E}(\Delta T_r^2) = \mathcal{E}(\sigma_r^2) = N\sigma_{\text{rec}}^2/t$. Because $\mathcal{R}S$ is approximately distributed as χ^2 , the expected variance ratio, $\hat{\sigma}^2/(\sigma_{\text{rec}}^2/t)$, can be determined from the integrated probability distribution of χ^2 for any confidence level. For the 95% confidence interval, this ratio is shown in figure 2.9 against the number of sky regions. The minimum occurs at $N = 9$, but is quite broad: only a 10% change in the expected variance ratio occurs over the range $4 \leq N \leq 20$.

Atmospheric and Instrumental Noise

Several atmospheric and instrumental effects contribute to the system noise level. These effects can be categorized by where they occur in the optical path,

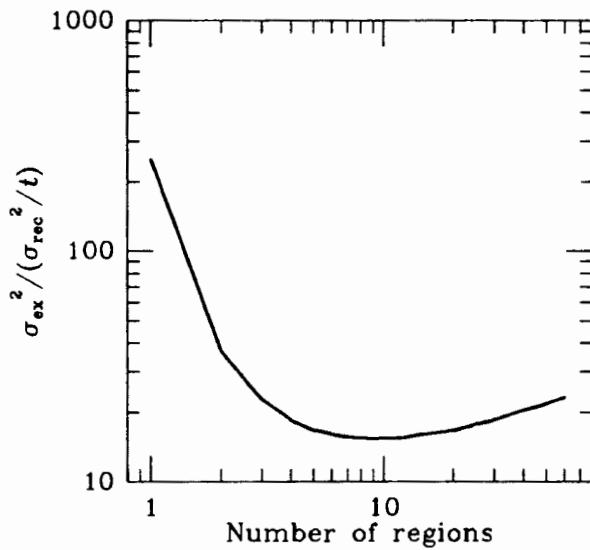


Figure 2.9. Ratio of 95% confidence upper limit on excess variance, $\hat{\sigma}^2$, to receiver noise σ_{rec}^2/t , vs. number of sky regions, N , for a fixed total observing time, t .

before, during, or after the beam switching process. All post-modulation noise arises from intrinsic Johnson noise in the detector and preamplifier. This noise is reduced as far as possible through careful design and selection of the photometer and its components, together with narrow band synchronous demodulation (Appendix B).

Pre-modulation noise is caused by space and time dependent fluctuations in atmospheric emission that are primarily due to inhomogeneities in the tropospheric water vapor distribution. At spatial and temporal frequencies below the modulation frequency, the atmospheric noise component is suppressed by the differencing implicit in beam switching and subsequent demodulation. To control the low frequency divergence of the characteristically red spectrum of atmospheric fluctuations, however, sufficiently high order differencing must be employed.³⁶ The differencing order is one less than the number of switched beam positions: two positions (A , B) yield a single difference, $A - B$, three positions (A , B , C) yield a double difference, $\frac{1}{2} [(A - B) - (B - C)] = \frac{1}{2}(A - 2B + C)$, and so forth.

A model³⁷ of the dependence of this noise source on the beam switching angle, θ_s , the beam switching frequency, f_s and the differencing order, n , indicates the integrated low frequency power scales roughly as $(\theta_s/f_s)^{-2n}$. Since the fundamental considerations discussed above set a lower bound on interesting values of θ_s , the highest possible switching frequency is important for suppressing red atmospheric noise. This highlights one important distinction between “chopping” and “wobbling” in customary sky sampling strategies where higher order differences are obtained by combining relatively high frequency, single difference beam switching (chopping) with lower frequency primary mirror motion (wobbling). The redder the noise, the less effective is the low frequency characteristic of wobbling. For this reason this experiment’s design has emphasized high frequency (~ 10 Hz) differencing. By necessity, this emphasis has driven the mechanical design of the secondary mirror and modulation system as well (Appendix A).

Although an ideal beam switch will sample the sky symmetrically, any practical system will exhibit various asymmetries; in the antenna reflectivity, for instance, or in the optical throughput of the switched beams. These asymmetries in the modulation process generate an atmospheric noise component orthogonal to symmetrically sampled atmospheric noise. In this case, the low frequency asymmetric atmospheric noise is attenuated only by second or higher order differencing.

Several related instrumental noise components must be considered as well. One stems from antenna emissivity asymmetry combined with the time dependence of the antenna surface temperature. Another comes through time dependent temperature gradients across the antenna surface and the average mirror surface emissivity. Higher order terms are possible but are relatively negligible. A third is time dependent diffracted or other environmental radiation modulated by secondary mirror motion. A fourth comes from the same general source as the third but is dependent

on primary mirror orientation. As far as they depend linearly on secondary mirror position, the first three components are suppressed by second-order differencing with secondary mirror beam switching. For nonlinearities, higher order differencing through secondary mirror motion or primary mirror wobbling can be a remedy. Wobbling, however, will introduce the fourth noise mentioned above, which then can be reduced only through another level of differencing, etc., – a process not guaranteed to converge.

A photometric comparison of differencing schemes (Chapter 4), showed that relative to single differencing, the double differencing noise level was almost a factor of four smaller, and not significantly larger than the intrinsic detector noise.

Unfortunately higher order differencing is a natural solution only to the symmetric differencing case. Asymmetries are best removed by symmetrizing the antenna and modulator geometry by periodically introducing 180° phase shifts in various components or by changing their phase both monotonically and continuously. With standard radio telescope hardware, however, such ploys as rotating the primary mirror about its symmetry axis are not possible. The alternative of removing higher and higher order polynomial asymmetry components is neither elegant nor efficient in the statistical sense.

For completeness, we mention one additional potentially important noise source, variable acoustic coupling between modulator and detector. We have minimized this problem through the torque cancelling design of the modulator, and up to now have not been able to measure this acoustic coupling in our system.

Celestial location

Two requirements of the observing strategy are apparent from the above discussions. First, for determining an upper limit to CBR anisotropies in a finite total observing time, the optimum number of independent sky regions is about ten. Second, telescope motion should be kept to the minimum required by the sampling pattern during observation of each region to reduce the effects of variable pickup of radiation from the ground. Only near the celestial pole is the apparent rotation rate of the sky slow enough that both of these requirements can be satisfied simultaneously.

The observing plan divided the sky around the north celestial pole into several pie slice regions, each to be observed once per night. When observing each region, the telescope was pointed just to the east or just to the west of the pole and at the same elevation as the pole. The double difference switching and single difference wobbling motions (fig. 2.10) then were carried out in the azimuth direction only to insure the same atmospheric attenuation for all beam positions. As the sky rotates, the spots of the pattern trace out arcs on the sky, smearing the sampling pattern (fig. 2.11). If the smearing angle is greater than the CBR correlation scale, independent fluctuations are averaged together, reducing the anisotropy signal. For a sampling pattern radiating from the pole, this smearing is worse for the outer spots. The drift time per region, 45^m , was chosen so the smearing at the pattern center is $5.5'$, less than the CBR correlation scale. Not coincidentally, this drift time allows observing ten independent regions in the roughly eight hours of observing time per night available after calibration and set up. The telescope position was alternated on either side of the pole, and the regions on each side interleaved as shown to attain the maximum packing of independent, nonoverlapping regions.

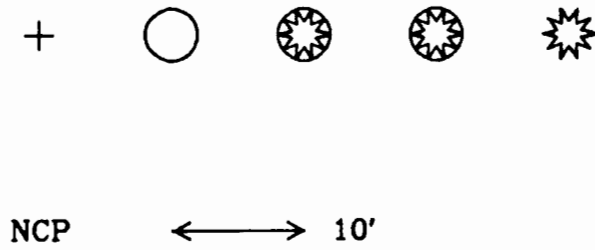


Figure 2.10. Switching and wobbling pattern. High frequency (5 Hz) beam switching takes place between the three spots in each group, and low frequency ($1/4^m 20^s$) telescope wobbling between the circled and starred groups.

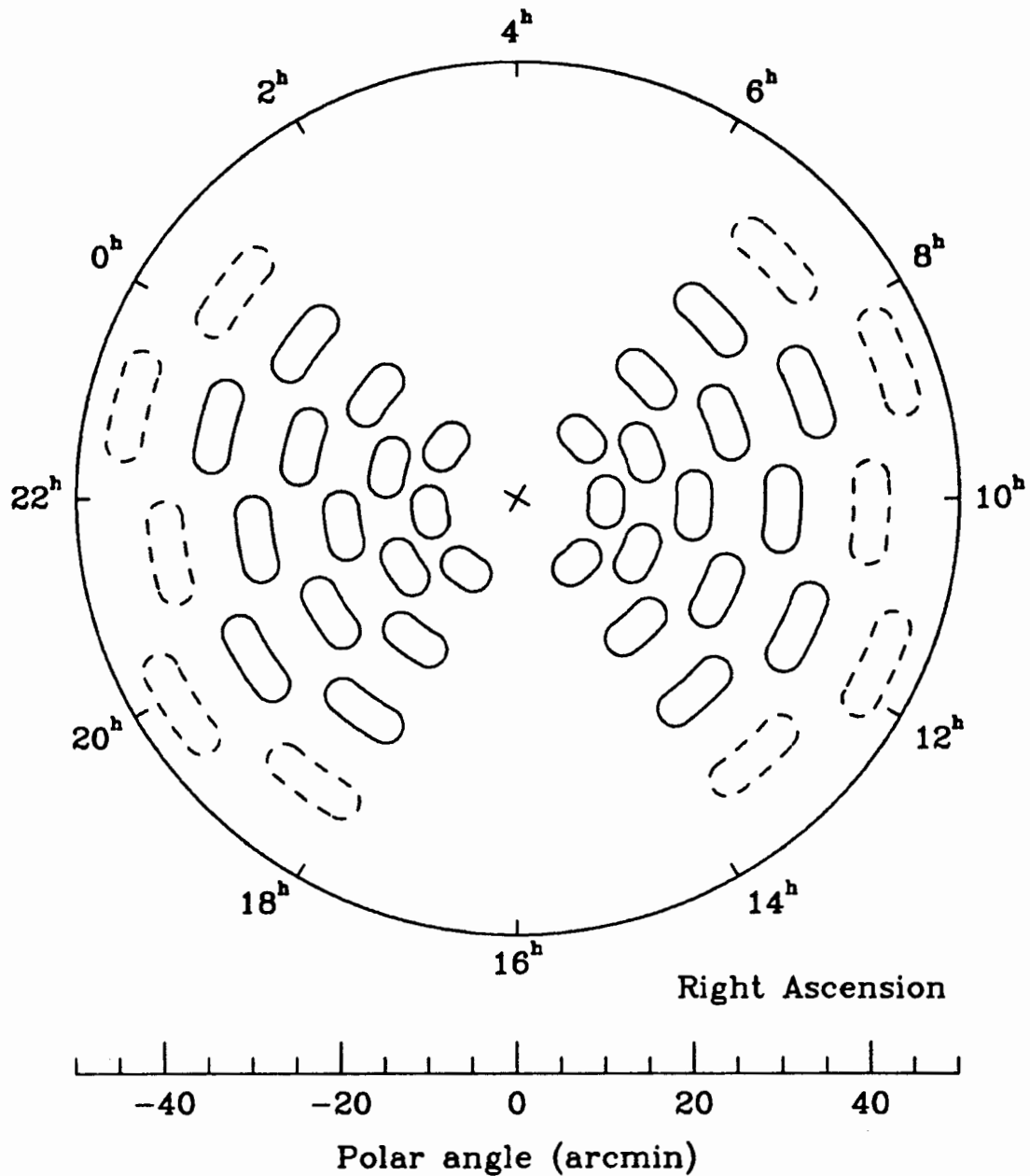


Figure 2.11. Sky sampling pattern near the north celestial pole. The telescope is pointed alternately east and west of the pole and the telescope beam switched and wobbled in azimuth among the four spots in each region. The ten regions observed (Chapter 4) are shown, for a beam size $\theta_b = 4'$, equal switching and wobbling angles $\theta_s = \theta_w = 10'$, and a drift time per region of 45.5^m .

Chapter 3. Experimental Apparatus

The experimental instrumentation was assembled according to the design described in the previous chapter. Three major systems comprise the apparatus: the telescope, the photometer, and the data acquisition system. Radiation from a spot on the sky defined by the telescope beam is concentrated by the telescope onto the entrance aperture of the photometer, which produces an electrical signal proportional to the incident radiation power. One of the telescope's major subsystems is the beam switch, capable of rapidly (~ 10 Hz) pointing the telescope beam back and forth between two (or more) spots on the sky in order to modulate the photometer input. The photometer output signal is synchronously demodulated and recorded by the data acquisition system. These systems are described in the following sections.

Telescope

In the early 1960's the Columbus, Ohio, division of North American Aviation manufactured the telescope (Plate I), which represents one of the first attempts at construction of a large reflector capable of significant performance at millimeter wavelengths. Subsequently, the Battelle Memorial Institute purchased the instrument and installed it in 1973 at the Battelle Observatory on Rattlesnake Mountain, part of the Department of Energy's Hanford Reservation near Richland, Washington. Battelle made the telescope available for dedicated use by this project.

Rattlesnake Mountain is a block uplift ridge with a steep northeast face (Plate II). The telescope site is about 30 m below and 175 m southeast of the summit, 1045 m above mean sea level at north latitude $46^{\circ}23'27.0''$, and west longitude $119^{\circ}35'10.9''$ (fig. 3.1). There are clear views of the northern, eastern, and southern



Plate I: Overall view of Battelle Millimeter Wave Facility.



Plate II: Rattlesnake Mountain from the southeast.

horizon, although the mountain summit rises 10° above the northwestern horizon. This rise does not impede observations, however, and it provides some shelter from strong westerly winds that occur in storms.

With less than 16 cm average annual precipitation, the region's climate is semi-arid.³⁸ The most favorable observing conditions occur when a high pressure ridge develops off the Washington and British Columbia coasts. Then the prevailing winds are dry inland northerlies that bring cold air and clear skies, rather than onshore westerlies that otherwise predominate. Typically, these favorable conditions can be expected for roughly 20 days during the winter season, November through March.

Figure 3.2 illustrates the major parts of the telescope. The parabolic primary mirror, supported by an aluminum truss, is attached to a steerable mount that rests on a concrete pier. At the prime focus, a weatherproof cage houses the nutation mechanism for the hyperbolic secondary mirror. This cage is supported by a tripod attached to the primary mirror truss. At the Cassegrain focus, receivers are mounted in a cabin located behind the primary mirror vertex. Adjacent to the pier, a house trailer contains the control room and some lab and office space. The succeeding paragraphs discuss the telescope's optical design, the construction and condition of its primary and secondary mirrors, its beam switch, its control system, and its pointing performance.

Optical Design

The telescope is a conventional Cassegrain configuration, with a parabolic primary reflector and a hyperbolic secondary reflector. In the course of modifying the telescope for this experiment, the original aluminum subreflector was replaced with a carbon fiber composite mirror. Although construction of a beam switch

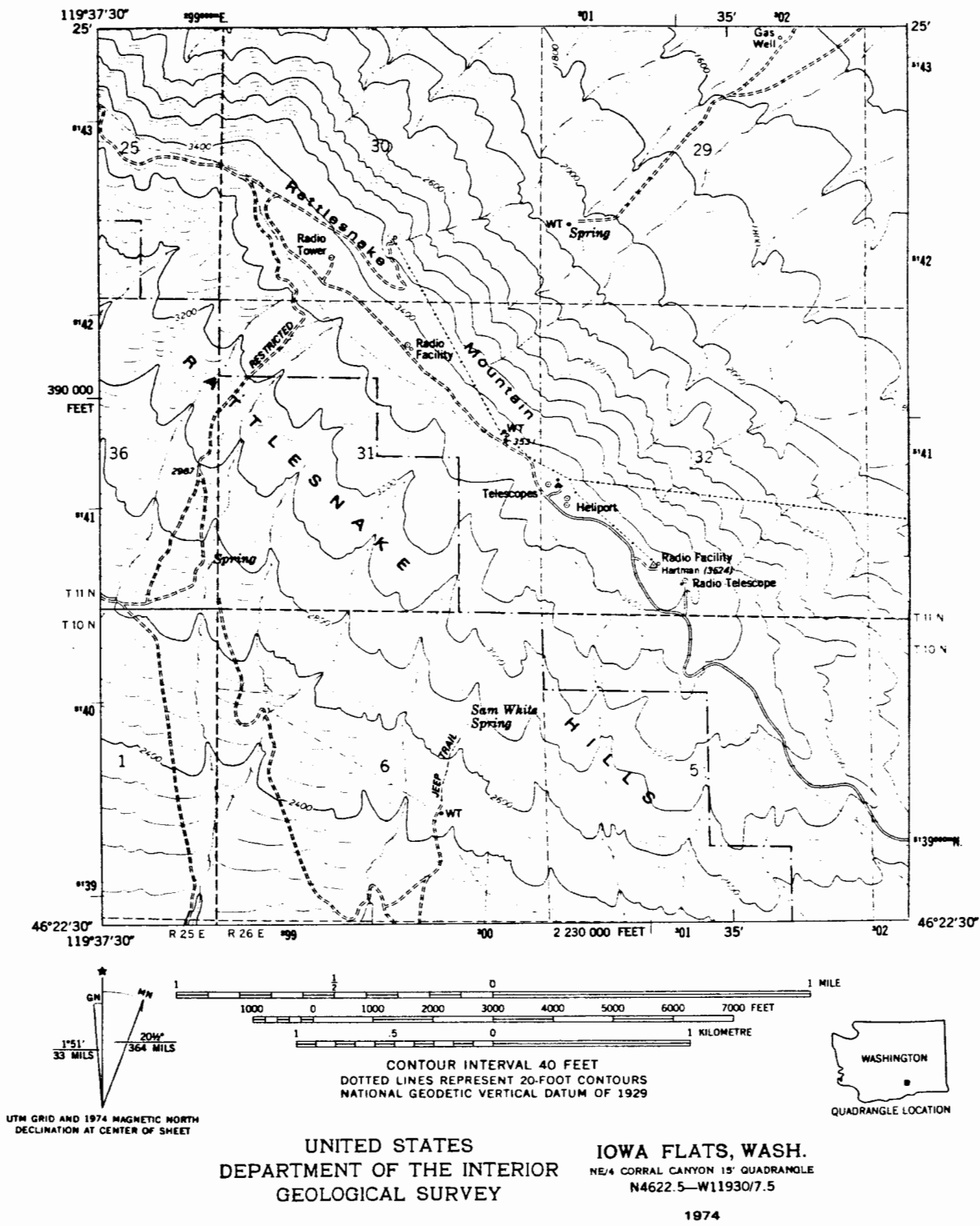


Figure 3.1. Environs of radio telescope site on Rattlesnake Mountain.

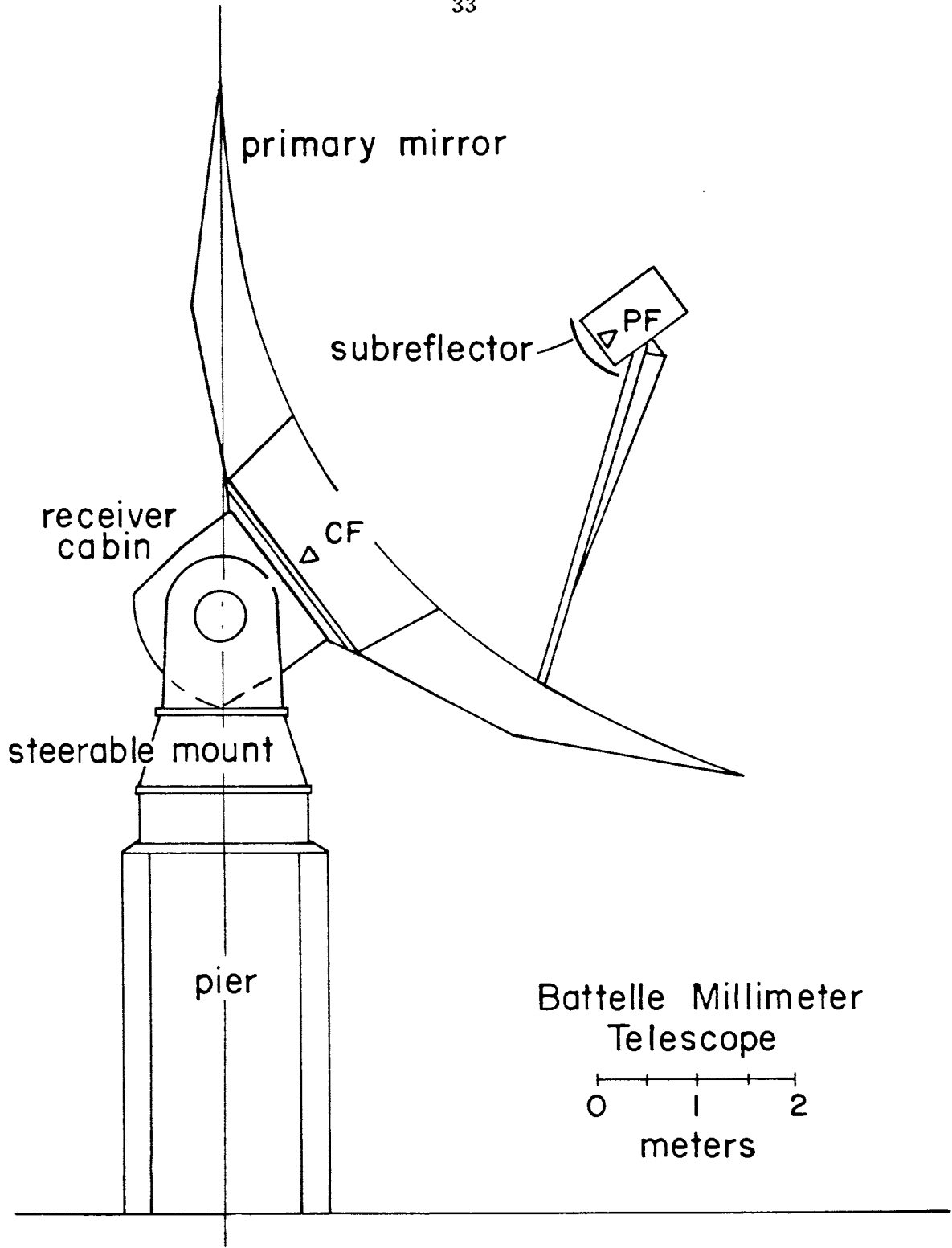


Figure 3.2. Overall view of the Battelle Millimeter Telescope, showing the location of the major components and of the prime and Cassegrain foci (PF and CF).

for modulating the pointing axis of the telescope was the principle motivation for this substitution, the opportunity was taken to modify the optical design to better suit the experimental design. Figure 3.3 illustrates the optical arrangement and table 3.1 lists the telescope's optical parameters.

Table 3.1. Optical Parameters

primary diameter	D	9144.60 mm
primary focal length	f	3200.40 mm
primary focal ratio	f/D	0.35
primary beam deviation factor	BDF	0.75
secondary diameter	d	750.00 mm
secondary focal length	F	39992.60 mm
secondary focal ratio	F/D	4.37
Cassegrain magnification	m	12.50
secondary beam deviation factor	BDF	1.00
secondary vertex to primary focus	ℓ	282.57 mm
secondary vertex to pivot	R	90 mm
primary vertex to secondary focus	L	613.21 mm

A major concern during the optical redesign was the amount of extraneous radiation reaching the detector. Although any radiation that originates at sources outside the main beam is extraneous, particularly troublesome is radiation that is reflected off the secondary mirror and so modulated by the beam switch. For example, if the subreflector overilluminates the primary mirror, then the detector

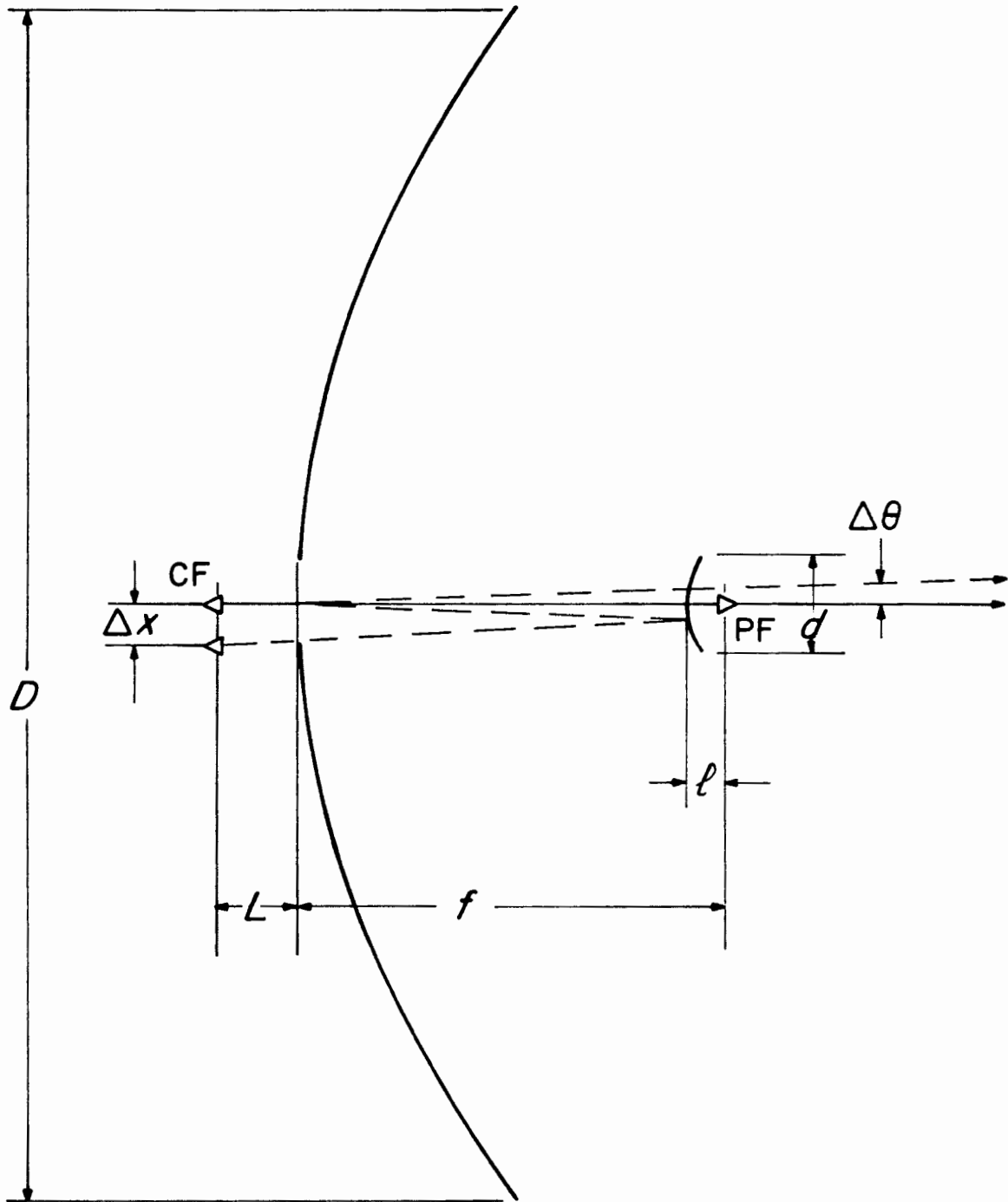


Figure 3.3. Optical arrangement of radio telescope, illustrating the location of the prime and Cassegrain foci (PF and CF), the optical parameters (table 3.1), and the Cassegrain focal plane scale, $\Delta\theta/\Delta x$.

will view some of the ground behind the telescope. As the secondary mirror nutates, the illuminated section of ground will be seen on each side of the telescope alternately. If there were a gradient in the temperature or emissivity of the ground, an offset would result from synchronous demodulation of the photometer output. Although an offset is, in principle, harmless, fluctuations and drifts in the offset can mimic and mask the signal of interest (Chapter 2). Also, the dynamic range of the demodulator is limited and the presence of a large offset reduces the amplification that can be used.

To avoid the pickup of this radiation from the ground behind the telescope, the subreflector was designed to illuminate only the central part of the primary mirror. When measured along the mirror surface, the unilluminated annulus at the primary mirror periphery is 570 mm wide, and it subtends 5.7° from the prime focus. This strip shields the subreflector from ground radiation diffracted at the primary mirror edge. A study³⁹ of the physical optics of this arrangement indicates a gradient of 0.1 K m^{-1} in the temperature of the ground should produce an offset of less than 10^{-4} K for secondary mirror nutations corresponding to beam shifts of $\pm 15'$. Furthermore, only the variations in this offset not cancelled by the sampling strategy affect the measurements.

Another potential source of extraneous radiation is reflection of the ground from the legs of the tripod supporting the prime focus cage. As a precaution against this problem, the tripod legs were covered with fairings designed to reflect only the sky onto the primary or secondary mirrors.

To preclude modulation of the optical throughput by nutation of the secondary mirror, the photometer's condensing cone slightly overilluminates the secondary mirror.

The magnification of the new mirror was chosen to place the Cassegrain focus at a convenient location in the receiver cabin behind the primary mirror. The magnification also determines the Cassegrain focal length and, consequently, the Cassegrain focal plane scale, $\Delta\theta/\Delta x = \text{BDF}/F = 5.2'' \text{ mm}^{-1}$. Here Δx is a displacement in the Cassegrain focal plane, $\Delta\theta$ is the corresponding angle in the sky, F is the Cassegrain focal length, and BDF is the Cassegrain beam deviation factor, which accounts for the finite curvature of the mirror surfaces.⁴⁰ The 45 mm diameter entrance aperture of the photometer's field optics was chosen to define a beam diameter of $3.9'$, and an optical throughput $A\Omega = 0.5 \text{ cm}^2 \text{ steradian}$, where A is the illuminated area of the primary mirror and Ω is the beam solid angle.

Nutation of a Cassegrain telescope's subreflector by an angle, $\Delta\phi$, will shift the telescope's beam direction proportionally,⁴¹

$$\Delta\theta = \left[R \left(\frac{\text{BDf}}{f} - \frac{\text{BDF}}{F} \right) - \frac{\ell}{f} (\text{BDf} + \text{BDF}) \right] \Delta\phi. \quad 3.1$$

where $\Delta\theta$ is the resulting beam shift, f and F are the primary and Cassegrain focal lengths, and BDf and BDF are the corresponding beam deviation factors.⁴⁰ The distances from the subreflector vertex to the primary focus and to the subreflector pivot axis are ℓ and R , respectively. To move the main beam of the Battelle telescope by $10'$, it is necessary to nutate the secondary by almost 1.25° . The geometric arrangement of a beam switch based on this principle is shown in figure 3.4. Appendix A is a detailed discussion of the design, construction and performance of the nutation mechanism used in this experiment.

As the main beam shift increases, coma becomes evident. Because our detector (Appendix B) is a nonimaging photometer, however, our requirements on image quality are not particularly stringent. Ray tracing studies³⁹ of our telescope indicate

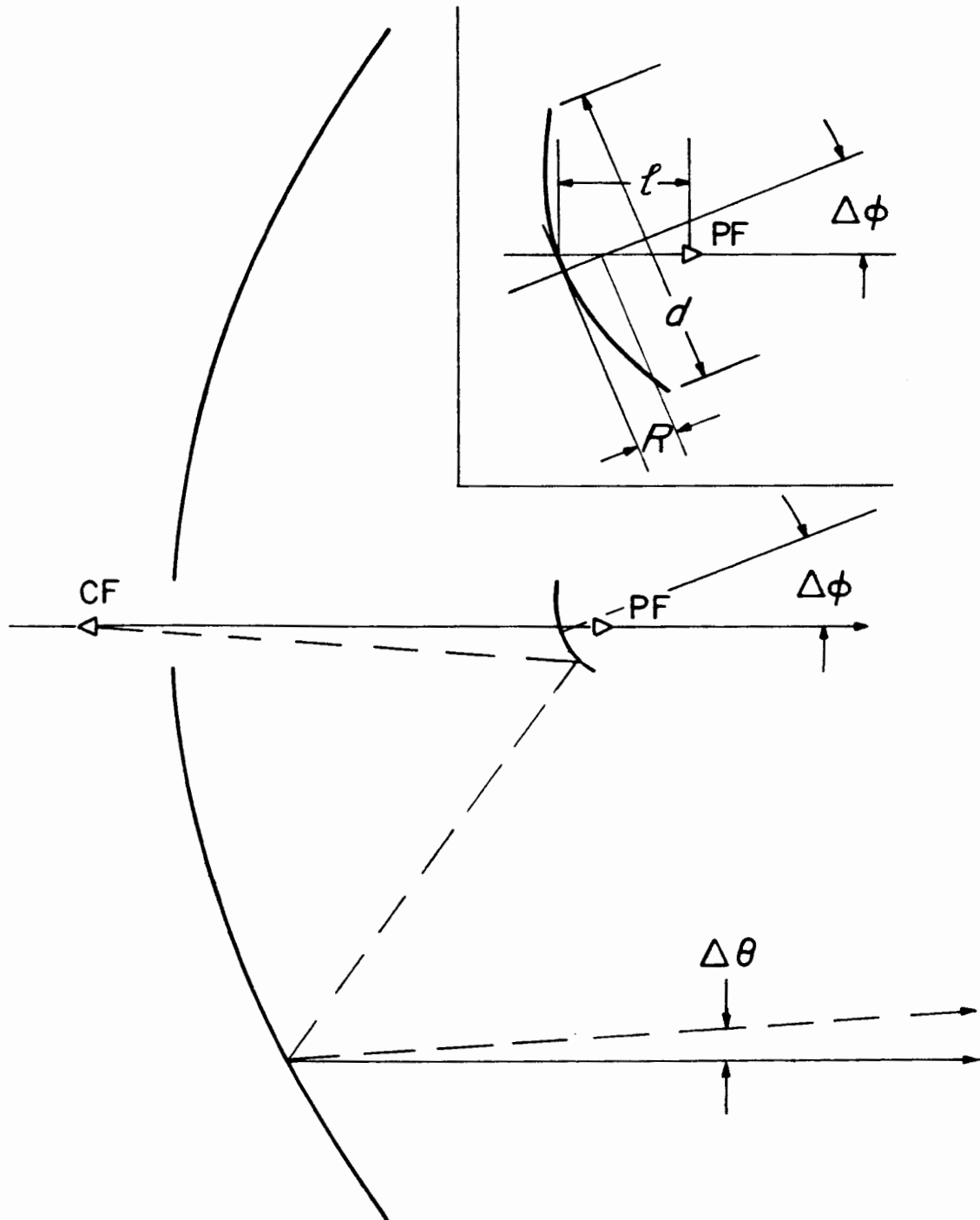


Figure 3.4. Optical geometry of beam switching by nutation of a Cassegrain telescope's secondary mirror. Insert: details of mirror nutation geometry.

more than 95% of the power from a point source remains within the photometer aperture for main beam shifts up to $15'$ from the optic axis.

Nutating the subreflector also shifts the illumination of the primary mirror. For a beam shift of $\Delta\theta = 10'$, the center of the illuminated area shifts by $(f - \ell + R)\Delta\phi(\Delta\theta/\Delta\phi) = -65.4 \text{ mm}(\Delta\theta/10')$, only 10% of the width of the unilluminated annulus at the primary mirror perimeter.

Primary Mirror

The primary mirror is comprised of 13 panels (fig. 3.5) supported by an aluminum truss. These panels are sandwiches of aluminum honeycomb between thin aluminum skins and are about 5 cm thick. They were manufactured by forming the front skin over a mold and then bonding the honeycomb, rear skin and edge pieces in place with an epoxy adhesive. The mirror structure is not a homologous design, but relies on the stiffness of the underlying truss to maintain its alignment under variable gravitational and wind loading. At the time of manufacture, the measured root mean square (rms) deviation of each panel from the equation of the parabola was 0.10 mm normal to the panel surface.⁴²

Upon installation on Rattlesnake Mountain the supporting truss was further stiffened against wind loads by the addition of tension members. The alignment of the reflector panels was measured using photogrammetry, and after appropriate adjustments, the measured rms deviation from the desired surface was less than 0.4 mm on all scales larger than 50 cm.⁴³ These mechanical imperfections in the figure of the primary mirror limit the telescope's optical performance; the nature of this limitation depends on whether a single mode, phase coherent receiver or a multimode, phase incoherent detector is used.

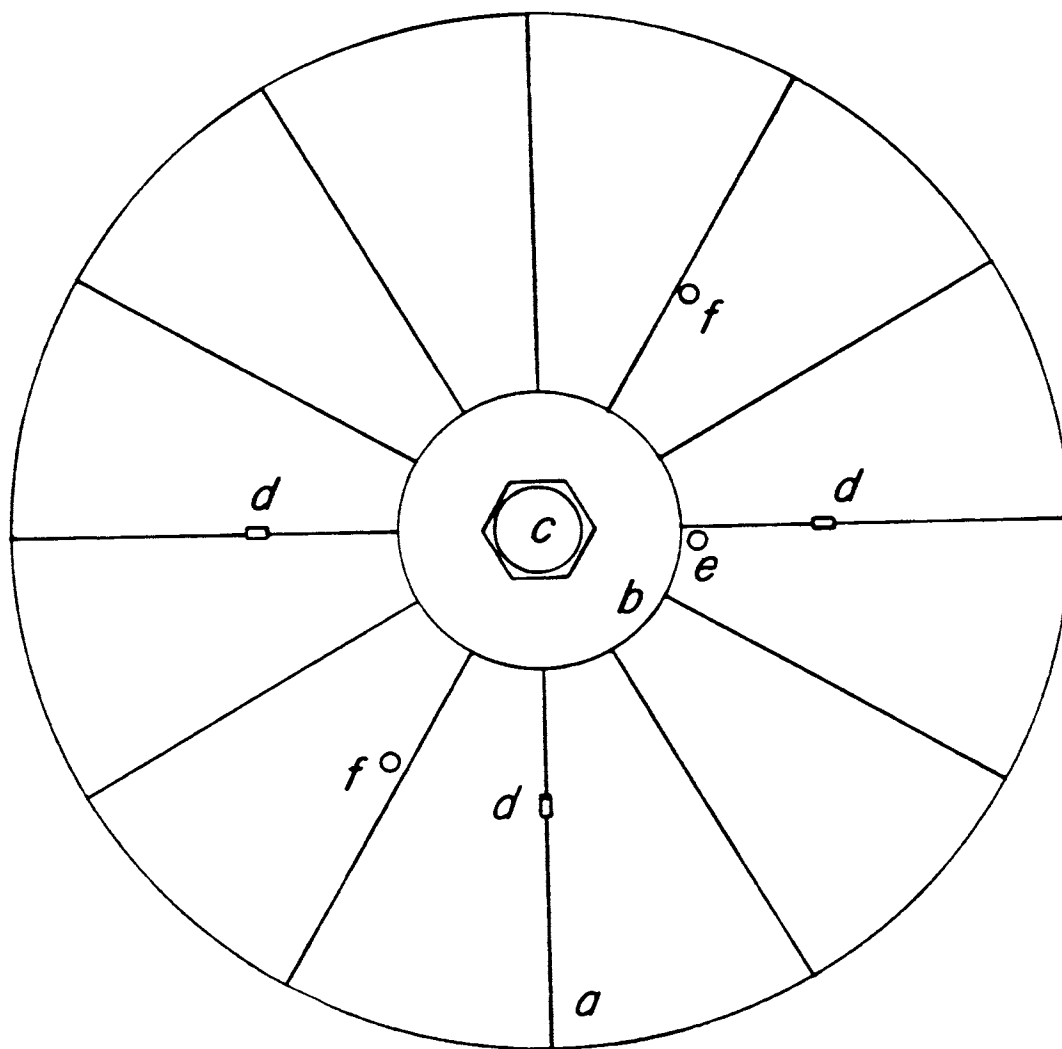


Figure 3.5. Frontal view of primary mirror. Twelve radial panels (a) surround the central panel (b), which is breached by the Cassegrain window (c). The feet of the tripod supporting the prime focus cage attach to the mirror truss at three points (d). The three small apertures for the boresight telescope (e) and cable feedthroughs (f) are covered with aluminum plates during observations.

Diffraction by the primary aperture determines the angular resolution of a single mode system, regardless of the surface state of the reflectors. The main beam response of a circular aperture is the Airy pattern,⁴⁴ which has a HMF_W of $\theta_{\text{diff}} \simeq 1.2\lambda/D$, where D is the aperture diameter and λ is the operating wavelength.

A diffraction limited system's forward gain, however, is directly affected by imperfections in the mirrors. For uncorrelated errors, an imperfect system's efficiency relative to an ideal system is⁴⁵ $\eta = \exp[-(4\pi\epsilon/\lambda)^2]$, where the effective rms surface tolerance, ϵ , is approximately equal to the rms deviation normal to the reflector surface. Figure 3.6 shows this efficiency as a function of wavelength, both for the panel tolerance measured by the manufacturer, $\epsilon \simeq 0.1$ mm, and for the upper limit on deviations of the installed mirror measured by photogrammetry, $\epsilon \geq 0.4$ mm. This indicates the individual panels are accurate enough for diffraction limited operation at $\lambda \geq 2$ mm. but, formally at least, the assembled reflector may only permit single mode operation at $\lambda \geq 7$ mm. The actual situation, however, is probably better than this analysis indicates. Measurements of the beam pattern and telescope efficiency made with a 130 GHz single mode receiver and a down range transmitter indicated an efficiency of roughly 25%.

In the case of a multimode system, the effect of reflector imperfections is to spread the incident power over a larger area in the focal plane, compared with an ideal system. If the detector area is large enough to intercept this power, the system efficiency is independent of wavelength, as is the angular resolution, given by⁴⁶ $\theta_{\text{res}} \simeq 25(\epsilon/\lambda)\theta_{\text{diff}} \simeq 30\epsilon/D$. An angular resolution of $\theta_{\text{res}} \leq 4.5'$ results from $\epsilon \leq 0.4$ mm, the overall deviation measured by photogrammetry.

An accident in 1984 damaged the outer portion of one of the panels. This damage appears not to have affected the performance of the telescope. Measure-

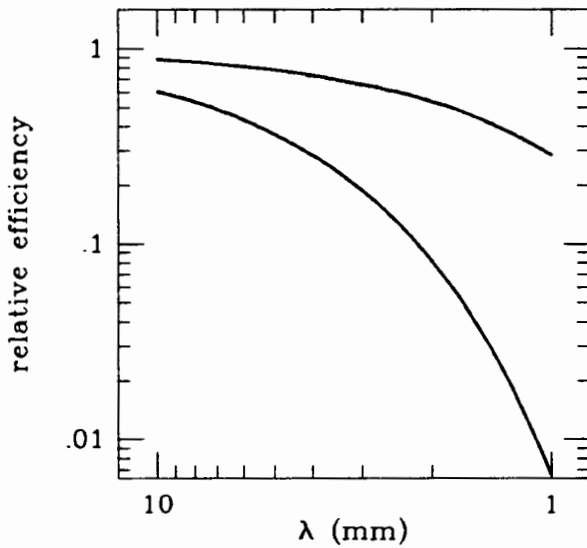


Figure 3.6. Relative efficiency of a diffraction limited, imperfect telescope. The top curve is the efficiency for $\epsilon \approx 0.1$ mm, the panel tolerance measured by the manufacturer and the bottom curve is the lower limit to the efficiency implied by $\epsilon \geq 0.4$ mm, the upper limit on reflector deviations measured by photogrammetry.

ments of the beam shape and efficiency made before and after the accident show no significant change.

The entire telescope, including the reflecting surface of the primary mirror is painted with a titanium dioxide based white paint. Laboratory tests show this paint is essentially transparent at millimeter wavelengths.

Secondary Mirror and Nutation Mechanism

The new secondary mirror and its nutation mechanism were built for rapidly steering the telescope beam through a small angle (fig. 3.7). Two electrodynamic motors nutate the mirror about its center of mass on flexural pivots. For a given motor capacity, higher slew rates are possible with a mirror that has a low moment of inertia, so the mirror was made of carbon fiber fabric impregnated with epoxy resin. This material has a high stiffness to mass ratio and low mass structures of complex shape relatively easy to fabricate from it. The finished mirror has a moment of inertia of 0.3 kg m^2 .

To minimize any possible acoustic coupling between the nutation mechanism and the detector caused by vibration transmitted through the telescope structure, a torque cancelling design was used for mounting the driving motors. Both the mirror and the motors are mounted on pivots so they counterrotate as the mirror is nutated. If the pivot spring constants are chosen properly, there is no net torque on the supporting structure.

The nutation mechanism is operated in a frequency compensated control loop that has a bandwidth close to 50 Hz. In response to a step input, the system's transition time is about 10 ms. Rather than a step input, however, a digitally generated transition waveform with no discontinuous changes in acceleration is used in operation to reduce the peak stresses on the mechanical linkages between the mirror and the motors. Overall, the system is capable of shifting the telescope beam by $10'$, which requires nutating the secondary mirror by 1.25° , in about 10 ms, and sustaining a switching frequency of 10 Hz. Details of the design, construction and performance of the nutation mechanism are discussed in Appendix A.

Control System

The telescope is mounted atop a concrete pier on a fully steerable horizontal mount. The physically allowed range of motion is $\pm 270^\circ$ about northeast in azimuth, and from 5° below the horizon to 10° beyond the zenith in elevation. Electrically controlled, hydraulically powered, servo motors drive the rotation about each axis with a maximum slew rate of 3° sec^{-1} . The angular velocity of the telescope is sensed by four optical encoders, two per axis. These are attached to pinions in the two gear boxes on each axis.

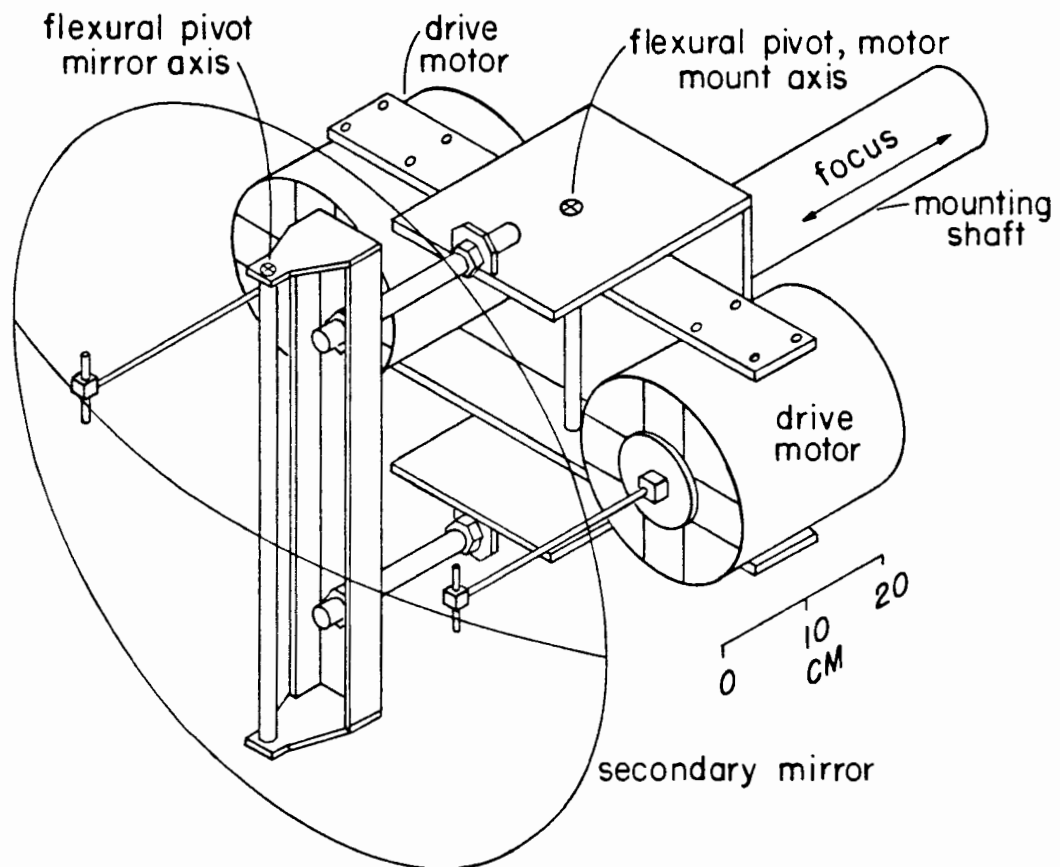


Figure 3.7. Secondary mirror nutation mechanism, illustrating the mirror and motor mount flexural pivots, the electrodynamic drive motors and the focus travel carriage. The mirror backstructure and translation stage are omitted for clarity.

A control program operating in a Perkin Elmer model 70 computer directs the telescope pointing. The program determines the current telescope position by integration of the encoder signals and develops appropriate control signals for the servo valves through digital to analog converters. A stable oscillator provides the local sidereal time, necessary for converting astronomical coordinates to azimuth and elevation. The current and desired telescope positions are displayed in both astronomical and horizon coordinates on a video display terminal, along with telescope status information. Pointing commands are accepted from either the terminal keyboard or the data acquisition system (see below).

The observing strategy involves long periods of integration with the telescope stationary. Unbalanced gravitational and wind loads shift the orientation of the telescope, however, when the hydraulic system is not running. Because of the microphonic sensitivity of the photometer, vibration generated by the 30 hp electric motor and pump precludes operation of the hydraulic drive during data integration. Independent electromechanical brakes were designed, constructed and installed, therefore, to hold the telescope fixed in any desired orientation. Four brake units are used, one in each of the two gear boxes on each axis. These brakes operate by engaging a delrin rack with a steel pinion in the gear box (Plate III) with manual or computer control possible through an electronic interface.

Pointing Performance

There are inevitable imperfections in any telescope mount that affect its pointing performance. The mount axes, for example, will not be perfectly orthogonal, nor will the azimuth bearing be absolutely level. The elevation and optic axes will not be exactly perpendicular, and the optic axis may also shift as the gravitational loads

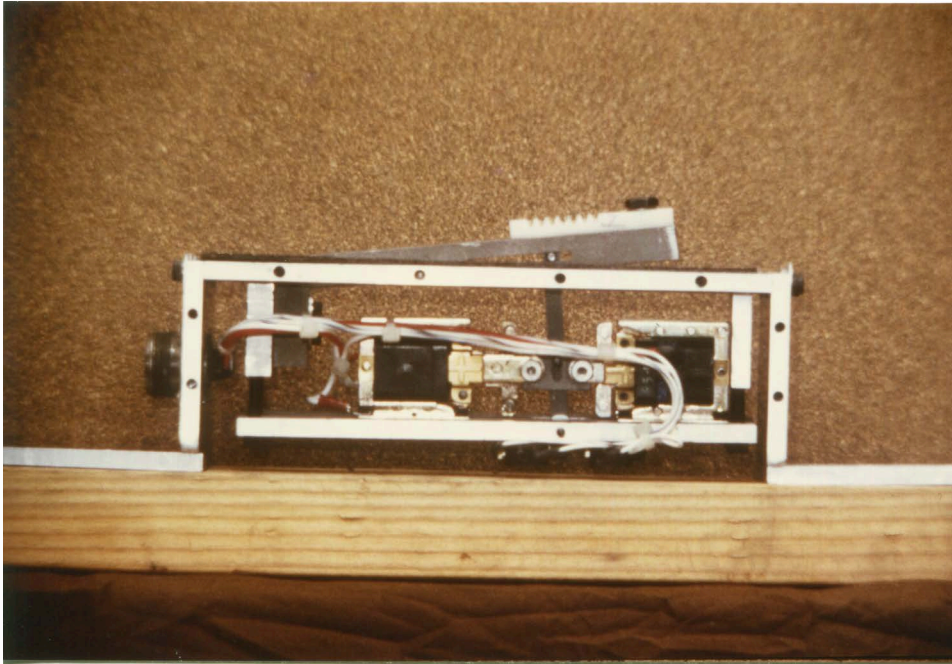


Plate III: Telescope Brake. The white delrin rack on the lever arm engages a steel pinion in the gear train, preventing telescope motion.

on the mirror structure vary in different orientations. Once measured, however, these effects may be successfully modeled and the model parameters used by the telescope control program to correct the telescope pointing. If the pointing errors are small, the linear model of table 3.2 satisfactorily describes these imperfections.⁴⁷

To measure misalignments of the mount axes, the positions of stars were observed with an optical telescope co-mounted on the radio telescope mount (fig. 3.8). During preliminary beam pattern tests with a 130 GHz receiver and downrange transmitter, the optical and radio axes were coaligned within 5', and this alignment was checked later during focussing observations of Saturn (Chapter 4). This boresight telescope is a refractor with a 15 cm diameter objective lens and a vidi-con television camera⁴⁸ was mounted on the telescope's eyepiece so observations could be carried out from the comfort of the control trailer. In conjunction with

Table 3.2. Telescope Mount Imperfection Model

$$A^* = A - \Delta A, \quad E^* = E - \Delta E,$$

$$\begin{aligned} \Delta \tilde{A} \equiv \Delta A \cos E &= A_0 \cos E + S_A A \cos E + C + C' \sin E \\ &\quad + I \cos A_T \sin E \sin A + I \sin A_T \sin E \cos A, \end{aligned}$$

and

$$\begin{aligned} \Delta E &= E_0 + S_E E + B \cos E + R \cot E \\ &\quad + I \cos A_T \cos A + I \sin A_T \sin A, \end{aligned}$$

where $A \equiv$ source azimuth, $E \equiv$ source elevation, $A^* \equiv$ azimuth encoder reading, $E^* \equiv$ elevation encoder reading, $\Delta A \equiv$ azimuth encoder correction, $\Delta E \equiv$ elevation encoder correction, $\Delta \tilde{A} \equiv$ cross elevation encoder correction, $A_0 \equiv$ azimuth encoder offset, $E_0 \equiv$ elevation encoder offset, $S_A \equiv$ calibration error of azimuth encoder, $S_E \equiv$ calibration error of elevation encoder,

$C \equiv$ collimation error of optic axis (the angle between the observer's left end of the horizontal axis and the optic axis is $90^\circ - C$),

$C' \equiv$ mount collimation error (the angle between the observer's left end of the horizontal axis and the upper vertical axis is $90^\circ - C'$),

$I \equiv$ tilt of the upper azimuth axis from the astronomical zenith,

$A_T \equiv$ azimuth toward which the upper azimuth axis is tilted,

$B \equiv$ gravitational flexure elevation correction at the horizon,

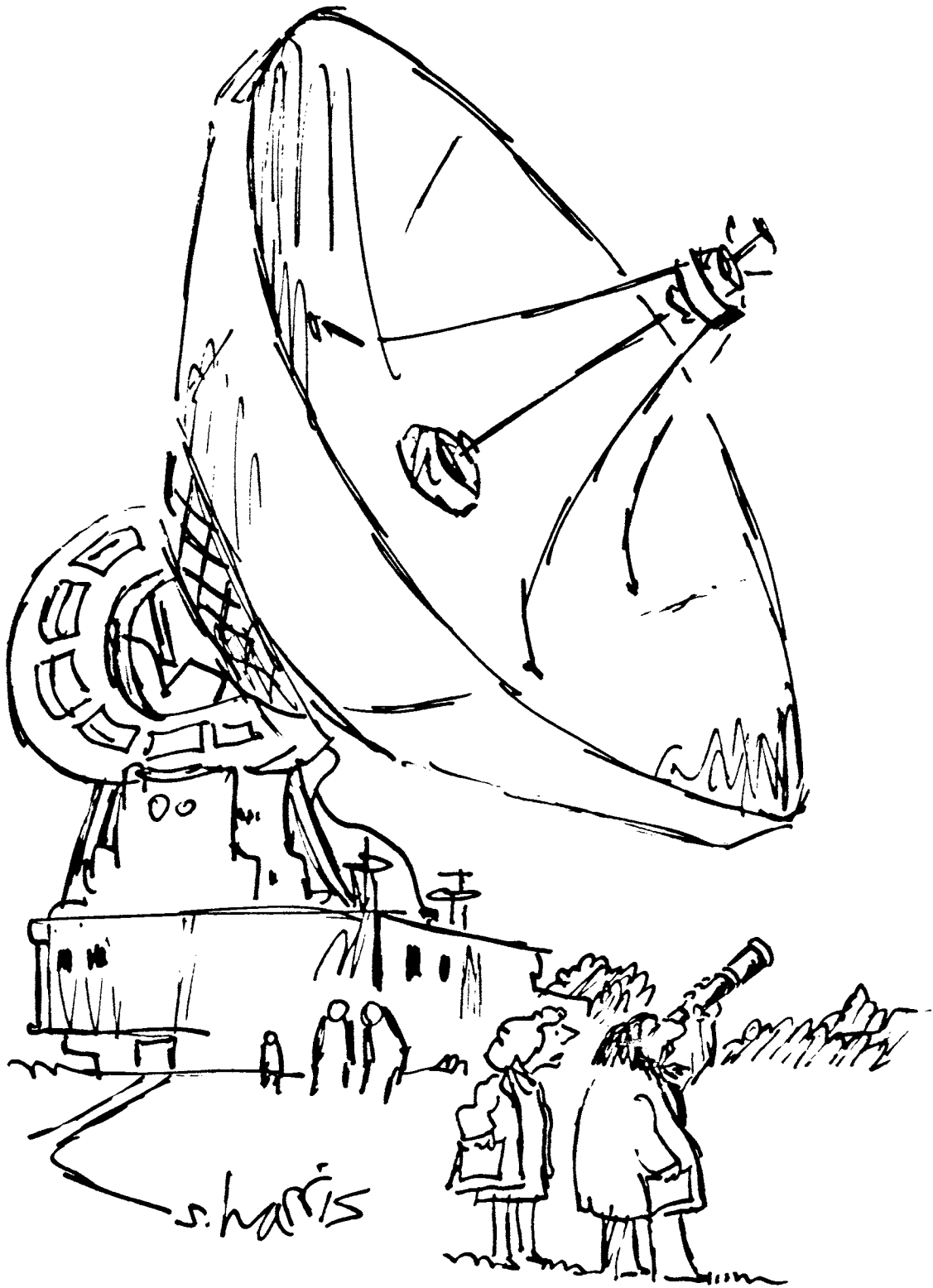
and $R \equiv$ refraction coefficient.

the telescope, this camera is sensitive enough to detect easily stars brighter than $m_V \simeq 2.5$.

About forty stars spread over the whole sky were observed in a typical pointing trial (fig. 3.9), and three independent measurements of each star's position were made. The coefficients of the pointing model were determined by a linear least squares fit to the recorded stellar positions. Figures 3.10 through 3.15 display the pointing residuals after subtraction of the best fit model for two pointing trials, February 20 and March 13, 1986. Within the statistical uncertainty, the two sets of parameters from the two nights' data are identical. On neither night is there any obvious elevation dependence in the residuals (figs. 3.11 and 3.14), but both nights' data show systematic azimuth dependences (figs. 3.10 and 3.13).

Wind is the likely cause of this effect; a strong breeze ($\approx 50 \text{ km hr}^{-1}$) blew from the northwest on March 13. When the telescope is pointed at an arbitrary angle to the prevailing wind, unbalanced wind loads exert torques about both axes. Only when the telescope is perpendicular to the wind is there no torque about the elevation axis, and the azimuth torque is zero only when the telescope is pointed up- or downwind. In figure 3.13, a sinusoidal variation of the elevation residuals with azimuth is apparent; an extremum is in the northwest ($A \approx 315^\circ$). Wind effects in the cross-elevation direction are larger, but less systematic. If an anemometer and a wind vane were connected to the telescope control computer, further improvement in the telescope's pointing performance might be made by applying a correction for wind loading.

Even neglecting the wind problem, the overall pointing error is quite small (figs. 3.12 and 3.15). If the elevation and cross-elevation residuals are uncorrelated – not exactly true because of the wind problem – and their means are zero, the mean radial error is $\langle \rho \rangle = (\sqrt{2}\sigma_E\sigma_A)^{1/2}$, where σ_E and σ_A are the standard deviations of



"Just checking."

Figure 3.8. Pointing Measurements.

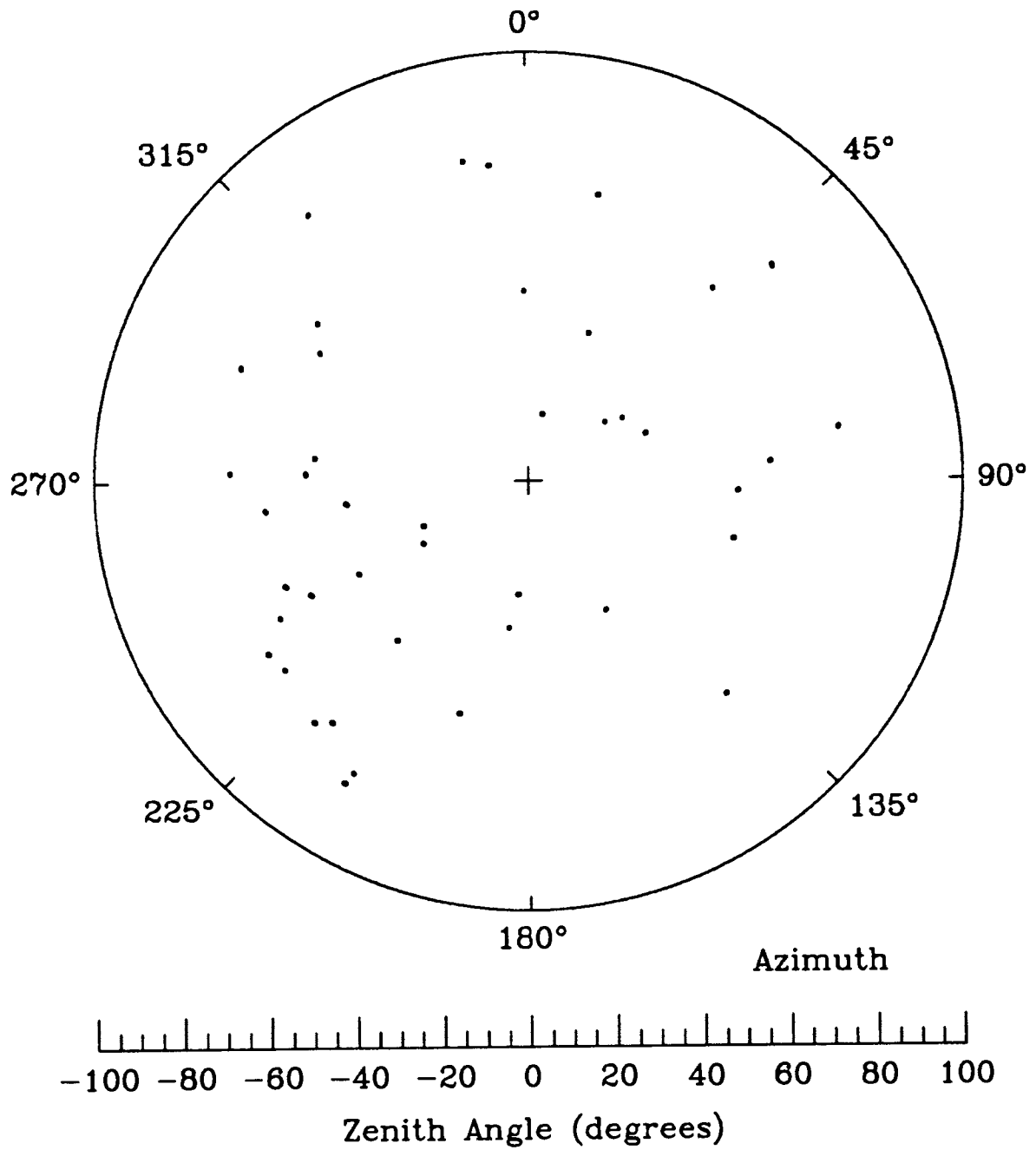


Figure 3.9. Distribution of pointing reference stars on the celestial sphere.

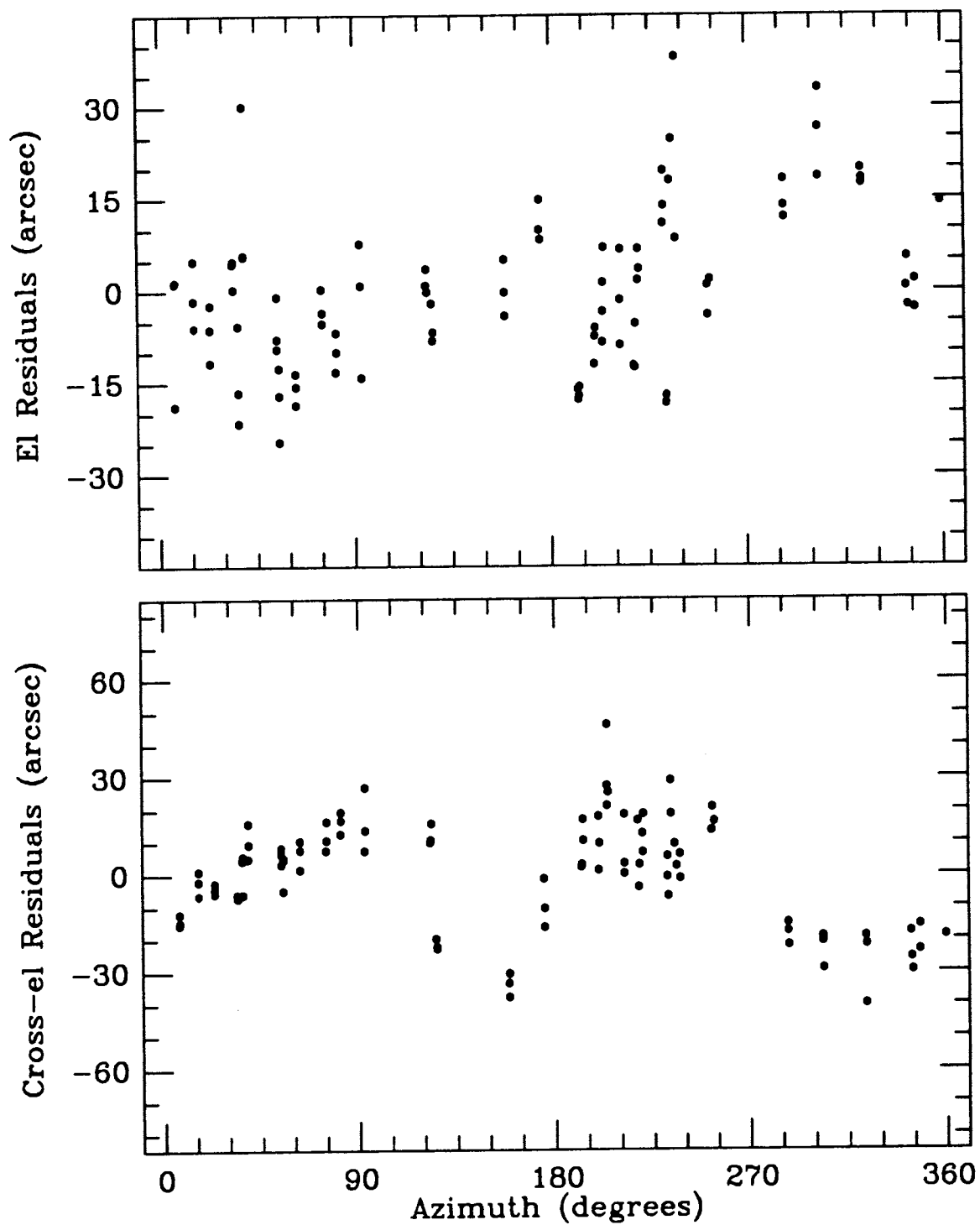


Figure 3.10. Pointing residuals vs. azimuth after least squares fit to the data from February 20, 1986

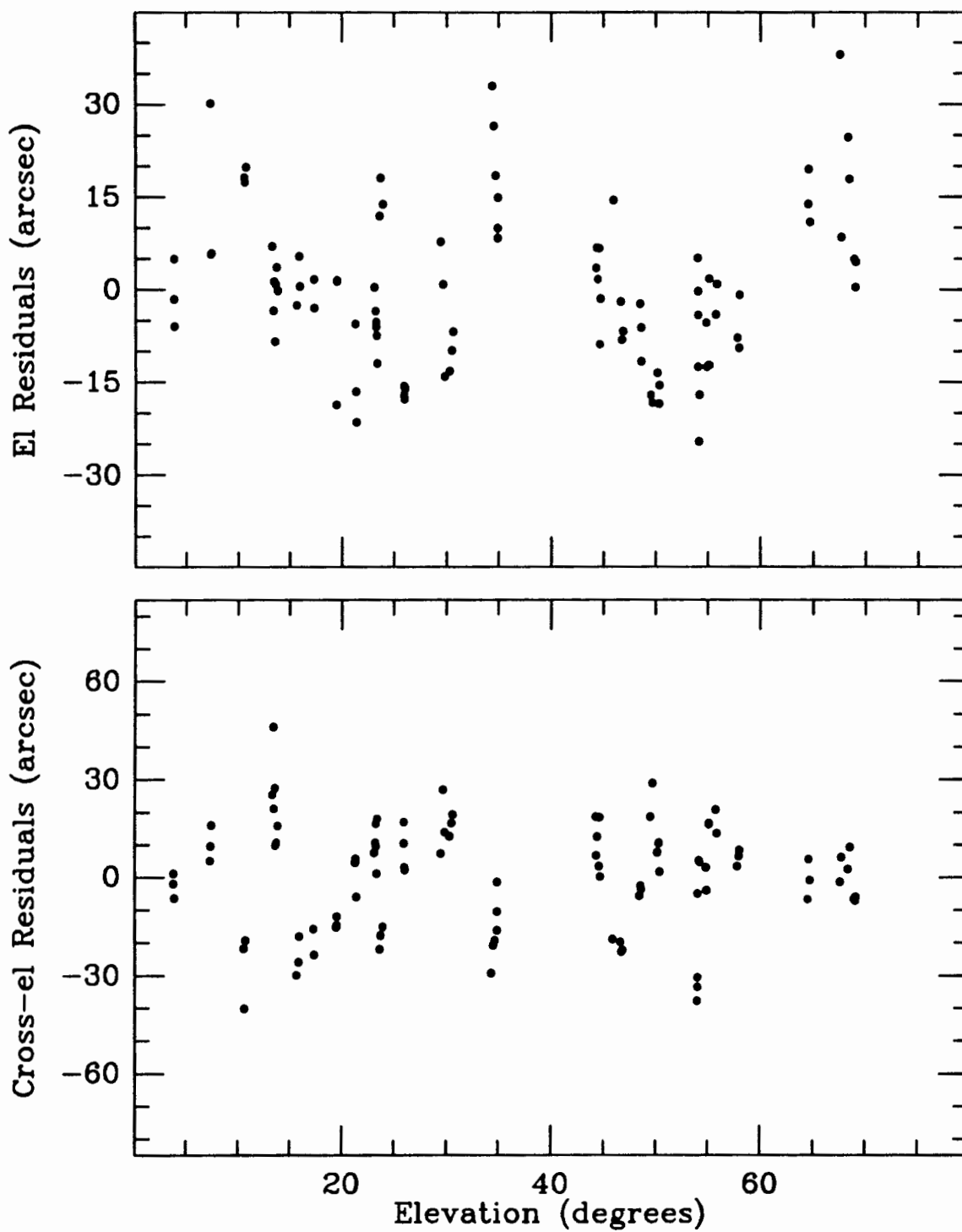


Figure 3.11. Pointing residuals vs. elevation after least squares fit to the data from February 20, 1986

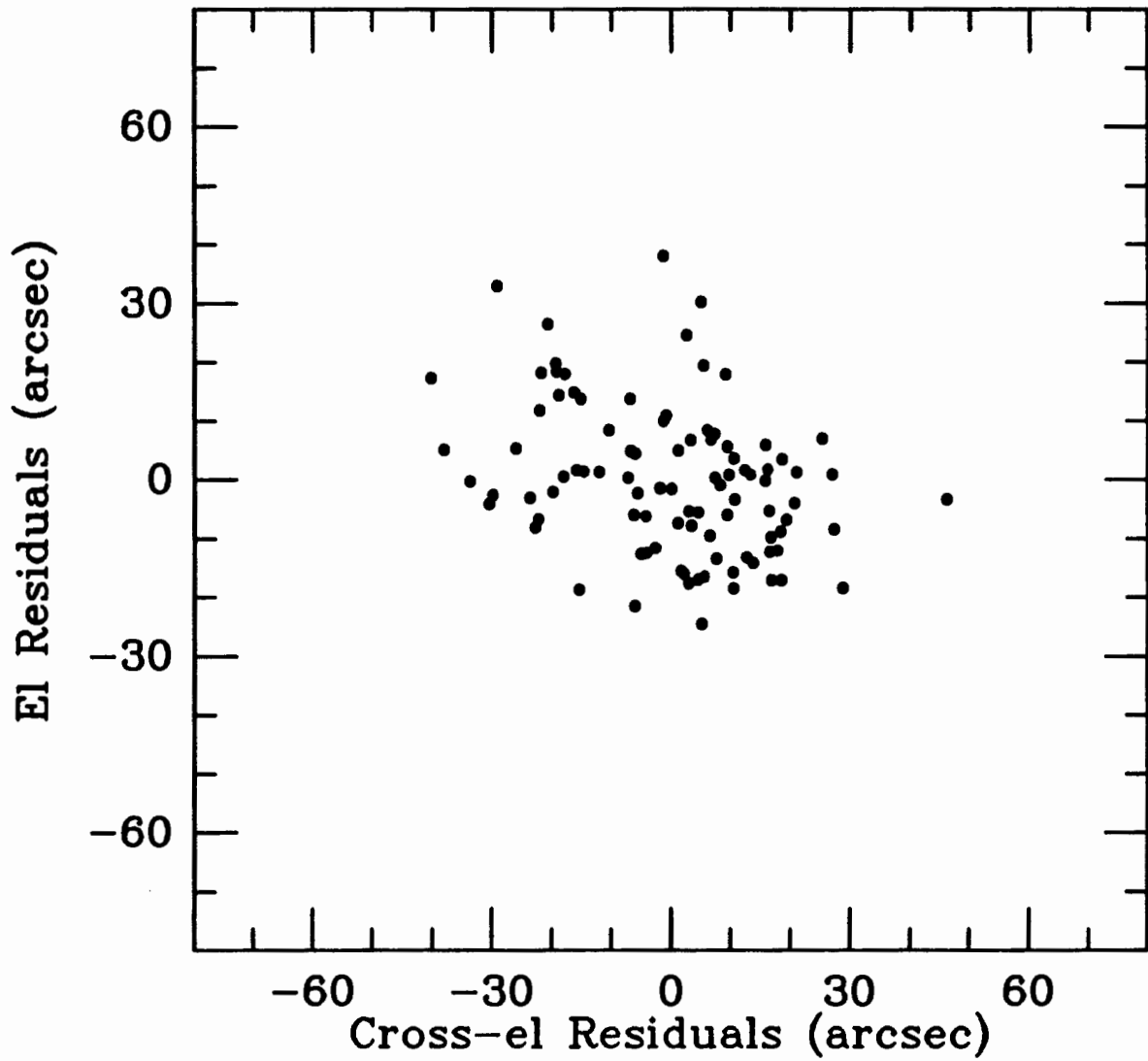


Figure 3.12. Elevation residuals vs. cross-elevation elevation residuals after least squares fit to the data from February 20, 1986

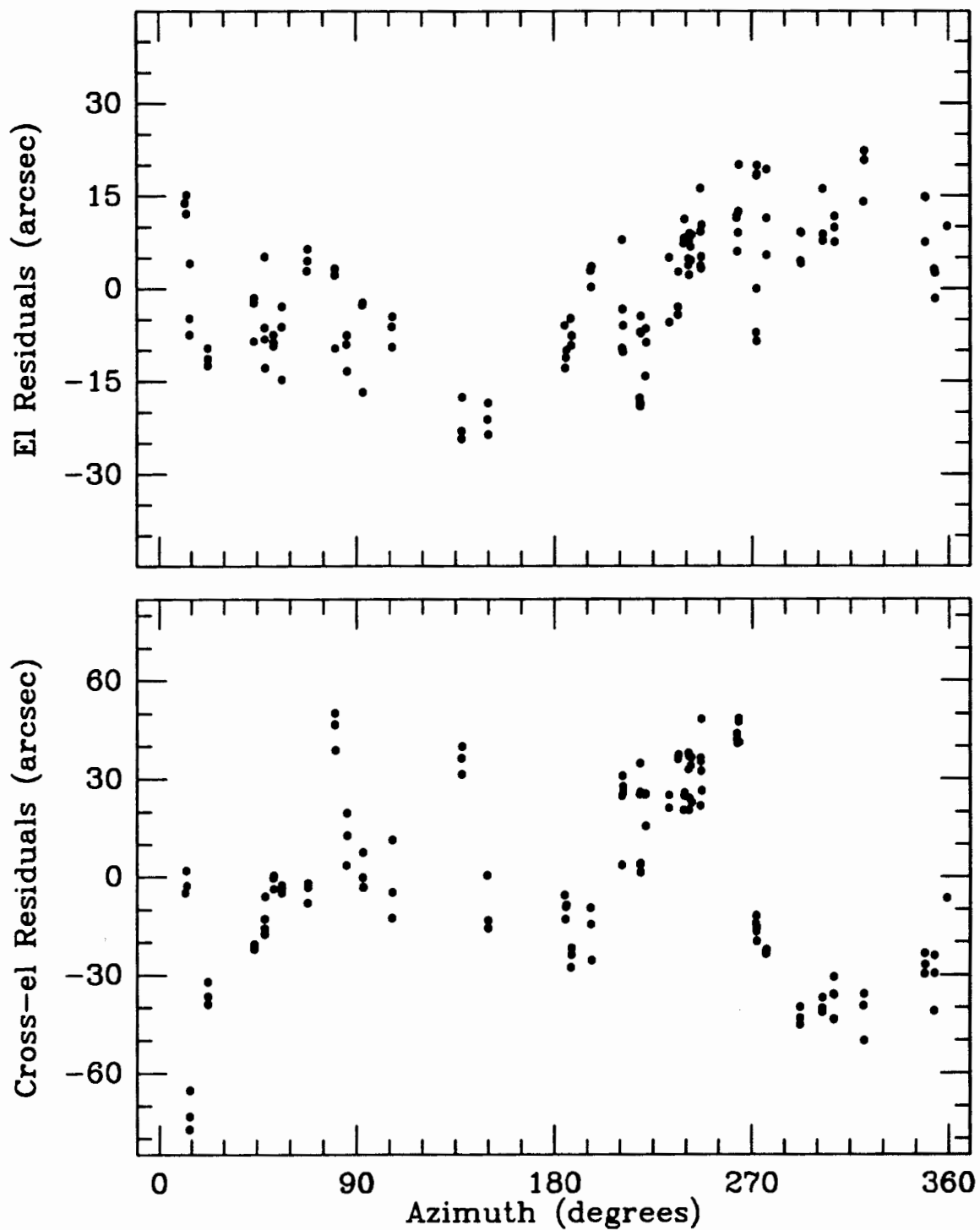


Figure 3.13. Pointing residuals vs. azimuth after least squares fit to the data from March 13, 1986

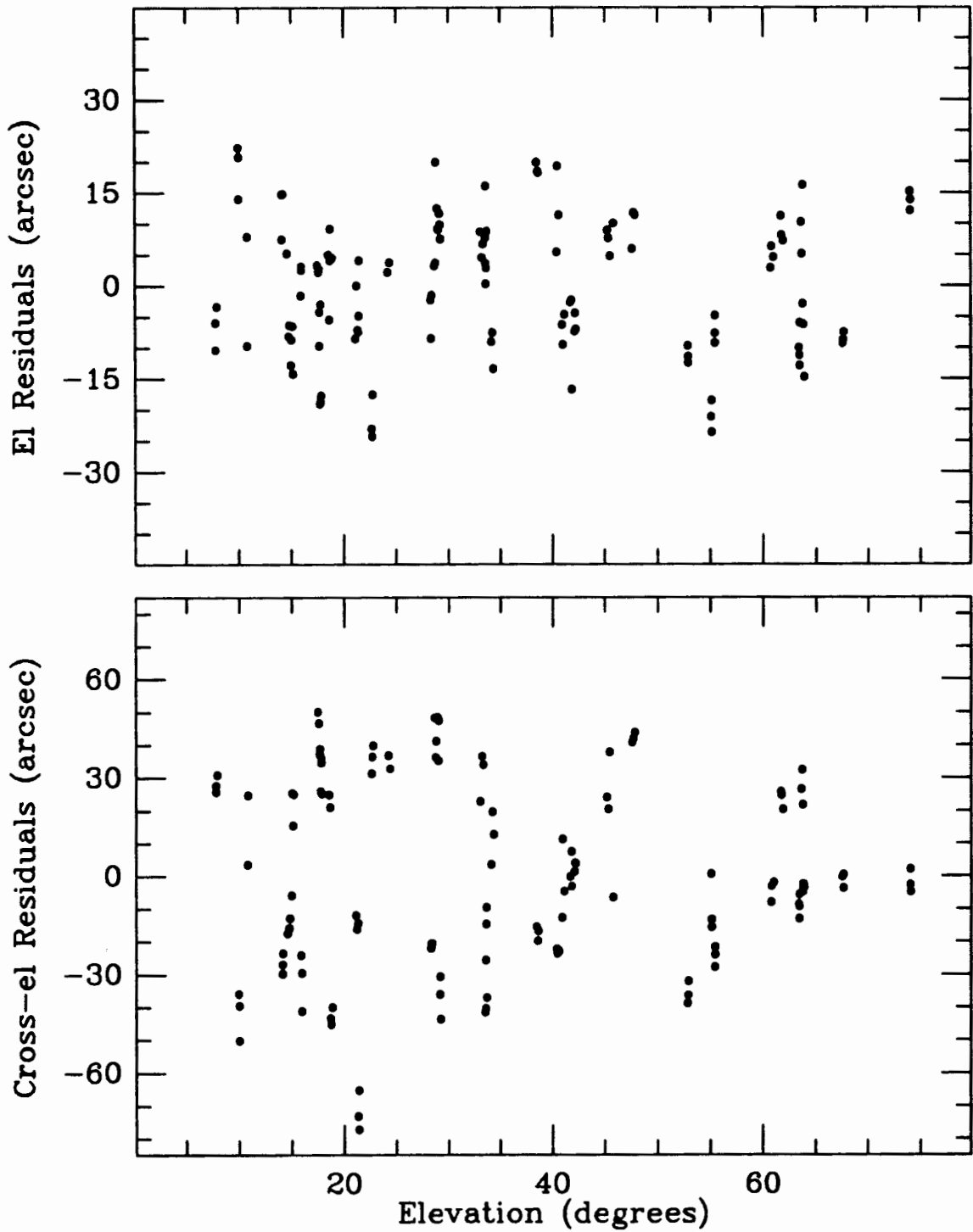


Figure 3.14. Pointing residuals vs. elevation after least squares fit to the data from March 13, 1986

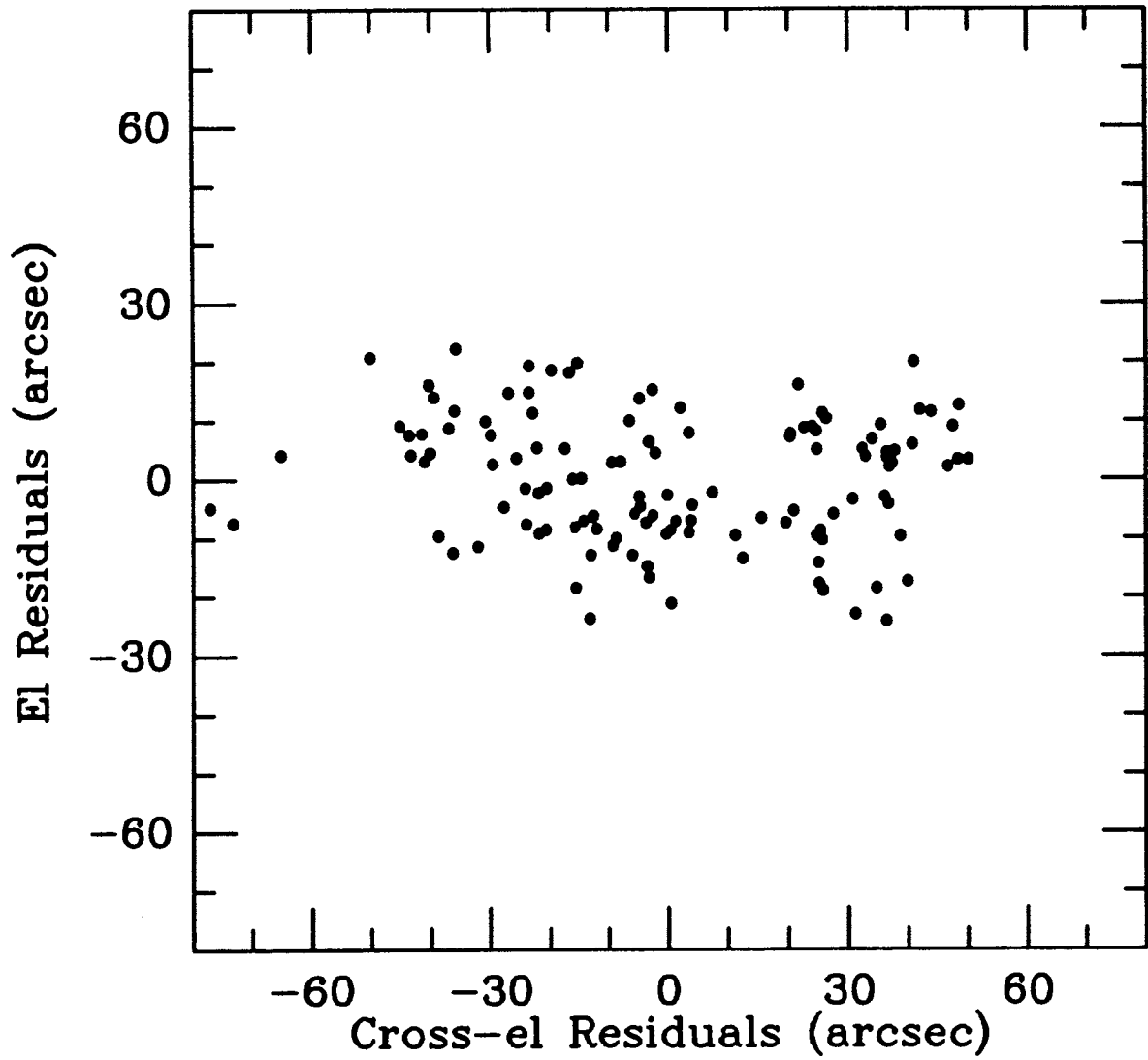


Figure 3.15. Elevation residuals vs. cross-elevation elevation residuals after least squares fit to the data from March 13, 1986

the elevation and cross-elevation residuals, respectively.⁴⁷ In table 3.3 the standard deviations of the residuals are listed, along with the mean radial pointing error, $\langle\rho\rangle$. For observation of the cosmic background radiation, an ubiquitous source, with a 4' diameter telescope beam that is switched by 10', this level of pointing performance, $\langle\rho\rangle < 0.5'$, is entirely adequate.

Table 3.3. Pointing Performance

Date		2/20/86	3/13/86
Cross-elevation standard deviation	$\sigma_{\bar{A}}$	17''	29''
Elevation standard deviation	σ_E	13''	11''
Mean radial error	$\langle\rho\rangle$	18''	21''

Photometer

The photometer produces an output voltage proportional to the brightness of a radiation source in the telescope beam. This voltage signal is demodulated and recorded by the data acquisition system. There are five major photometer subsystems:

- The detector is a large area composite bolometer – a doped germanium thermometer bonded to a 25 mm² diamond substrate – with an electrical responsivity of 7×10^6 V/W and an equivalent noise voltage of $10 \text{ nV}/\sqrt{\text{Hz}}$;
- The filters determine the instrument's passband, $4.5 \pm 0.5 \text{ cm}^{-1}$, and block all unwanted near infrared radiation;

- A compound parabolic concentrator efficiently couples the detector to the telescope optics;
- A low noise, high gain preamplifier matches the high impedance bolometer circuit to the input circuit of the data acquisition; and
- A ^3He evaporation refrigerator is the backbone of the instrument, cooling the detector, concentrator, and some of the filters to 0.35 K.

A detailed description of the design, construction, and performance of these systems is given in Appendix B.

Data Acquisition System

Overall control of the experiment and signal processing are the functions of the data acquisition system, resident in a microcomputer based on the Zilog Z80 microprocessor. A multitasking, real time operating system was developed to manage these functions. This program has three major divisions: the acquisition section records the photometer output for later analysis, the utility section manages the computer's resources and provides some simple data analysis and display procedures, and the control section synchronizes telescope motion and data acquisition with the observing plan.

Signal processing is carried out by a mixture of hardware and software. A lock-in amplifier⁴⁹ driven by the beam switch trigger signal, synchronously demodulates the signal from the photometer. After passing through a low pass filter, the lock-in's output is monitored on a strip chart recorder. Every 10 ms, an 8 bit analog to digital converter in the microcomputer evaluates the filtered output. Depending on the particular observation, from 10 to 2550 of these values are accumulated by the acquisition program and averaged to form a sample. Groups of up to 255 of

these samples are recorded, together with the telescope position and other pertinent information, on flexible magnetic disks.

The series combination of the low pass filter at the output of the lock-in amplifier and the averaging of the digital values in the acquisition program determines the effective integration time for each sample. The low pass filter, with a 12 dB per octave rolloff and a time constant, τ_{rc} , has a voltage response of:

$$G_{LP} = (1 - s^2 \tau_{rc}^2)^{-1}, \quad 3.2$$

where s is the complex angular frequency. Averaging of the digital samples is equivalent to integration over a time interval, t , and the Laplace transform of a rectangular aperture gives the voltage response of this averaging:

$$G_A = \frac{\sinh(st/2)}{st/2} e^{-st/2}. \quad 3.3$$

The effective integration time, τ_{eff} , of an arbitrary filter is defined as the integration interval of an equivalent ideal integrator with the same frequency integrated power response,

$$\int_0^{i\infty} ds |G_{eff}|^2 = \int_0^{i\infty} ds \left| \frac{\sinh(st_{eff}/2)}{st_{eff}/2} e^{-st_{eff}/2} \right|^2 = \frac{2}{\tau_{eff}} \int_0^{\infty} dx \frac{\sin^2 x}{x^2} = \frac{\pi}{\tau_{eff}}. \quad 3.4$$

For the series combination of low pass filter and digital averaging, this effective integration time is calculated from the filters' frequency responses by setting $x = ist$ and $\alpha = t/2\tau_{rc}$. Then

$$\tau_{eff} = \pi \left\{ \int_0^{i\infty} ds |G_{LP} G_A|^2 \right\}^{-1} = \pi \left\{ \frac{2\alpha^4}{t} \int_0^{\infty} dx \frac{\sin^2 x}{x^2(\alpha^2 + x^2)^2} \right\}^{-1}, \quad 3.5$$

which can be integrated using

$$\int_0^{\infty} dx \frac{\sin^2 ax}{x^2 (x^2 + b^2)^2} = \frac{\pi}{4b^4} \left[2a - \frac{3}{2b} + \left(\frac{3}{2b} + a \right) e^{-2ab} \right] \quad 3.6$$

to get

$$\tau_{\text{eff}} = t \left\{ 1 - \frac{3\tau_{\text{rc}}}{2t} + \frac{1}{2} \left(\frac{3\tau_{\text{rc}}}{t} + 1 \right) e^{-t/\tau_{\text{rc}}} \right\}^{-1}, \quad 3.7$$

shown in figure 3.16. This effective integration time was used at each step in the data analysis to calculate the noise equivalent voltage of the photometer from the sample variance of the data.

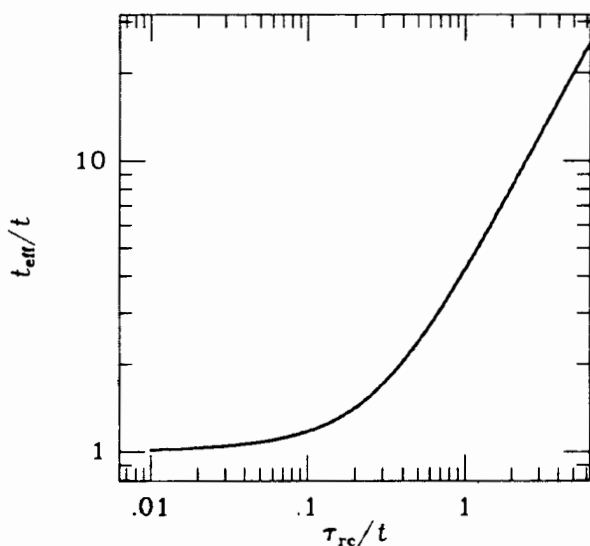


Figure 3.16. The ratio of effective integration time to digital integration time, τ_{eff}/t , as a function of the ratio of filter time constant to digital integration time, τ_{rc}/t , for a 12 dB per octave low pass filter cascaded with a digital integrator.

A serial communications link connects the data acquisition system with the telescope control computer. Following the predetermined observing plan, the experiment control program generates telescope pointing commands and transmits them over this link. After completing the pointing task, the telescope computer

replies, returning the telescope coordinates and the sidereal time. Upon receipt of this information, the control program starts the data acquisition program to begin an observation. Programmed observing plans include several anisotropy sampling patterns near the north celestial pole and a tipping routine to measure atmospheric opacity.

Chapter 4. Operation and Observations

Begun before 1980, assembly of the experimental apparatus was finally completed in December, 1985. Before measurements of the CBR could be undertaken, though, observations of the Moon and Saturn were required to evaluate and optimize the performance of the integrated system of photometer and telescope. Focussing the telescope was accomplished by adjusting the position of the secondary mirror to maximize the signal from an astronomical source. Initially, a course focus setting was made by observing the Moon and then Saturn, essentially a point source, was observed to refine the focus. Once the telescope was focussed, the beam profile was probed using Saturn, and the beam position relative to the boresight telescope cross hairs and the separation of the switched beams were also measured. Finally, the overall calibration of the system sensitivity for observations of extended objects was determined from observations of the Moon, which fills the telescope beam with a constant brightness source. The atmospheric attenuation was found by "tipping" the telescope and measuring the variation with zenith angle of the brightness of the sky. Following completion of these tests, the fine scale isotropy of the CBR was examined.

Telescope focus

Two focus adjustments are necessary with a Cassegrain telescope: the near focus of the hyperbolic secondary mirror must be coincident with the focus of the parabolic primary mirror, and the detector must be positioned at the far focus of the hyperboloid. These two adjustments have quite different tolerances.

Since the optical elements of a phase coherent, diffraction limited system must be positioned more carefully than those of a phase incoherent system, the diffraction

limited focal tolerance is a conservative gauge of the necessary focusing precision. The diffraction pattern near the focus of a telescope with a circular aperture is well known.⁴⁸ In particular, the intensity along the optic axis varies as $I(u) = I_0 [\sin(u/4)/(u/4)]^2$, for $u = (2\pi/\lambda) (D/2f)^2 y$. Here λ is the operating wavelength, D is the diameter of the diffracting aperture, f is the focal length, y is the distance along the optic axis from the focal point, and I_0 is the intensity at the focal point. The focal tolerance may be estimated as the axial displacement where the intensity is reduced by 20%. This occurs at $u \simeq 3.2$, giving $\Delta y = \pm(3.2\lambda/2\pi) (2f/D)^2 \simeq 2\lambda(f/D)^2$. At the experiment's operating wavelength, $\lambda = 2.2$ mm, the permissible defocusing at the Cassegrain focus of the Battelle telescope is $\Delta y_c = \pm 84$ mm, but at the prime focus, however, the secondary mirror must be positioned within $\Delta y_p = \pm 0.5$ mm.

Finding the optimum position for the secondary mirror required photometric observations of bright sources, first the Moon and then Saturn. Because the Moon's diameter exceeds the beam separation as well as the beam size, beam switching adds unnecessary complications to lunar observations intended to focus the telescope. Instead, these observations were made using an alternative modulation scheme, load switching, where the incoming radiation is compared with the radiation from a local reference source. A two blade, "butterfly" chopper wheel was mounted in front of the photometer and spun so the photometer aperture was covered and uncovered at a frequency of 10 Hz. On the side facing the photometer, the chopper blades were covered with a 10 mm thickness of Eccosorb,⁴⁹ a conductive, carbon loaded urethane foam with high emissivity at microwave wavelengths, to provide an ambient temperature reference source.

The atmosphere is less emissive and colder than the reference source, so a sourceless region of the sky will give a sizable signal when load switching is used. Since the

atmosphere is always present between the telescope and a celestial source, determining the source brightness involves measuring the difference between this sourceless atmospheric signal and the signal from the source and atmosphere together. The usefulness of load switching is limited, therefore, to observations of strong sources, such as the Moon, by the finite dynamic range of the demodulator.

To focus the telescope, a series of lunar drift scans were made with the subreflector at different positions along the optic axis. In these drift scans, the telescope was pointed just ahead of the Moon and stopped, whereupon sidereal motion swept the Moon through the telescope beam. The drift scan angular scale was determined from the sidereal rotation rate. Figure 4.1 illustrates the variations with subreflector position of the lunar signal amplitude and in the measured drift profile width. As the subreflector approaches the focus position from either side, the drift profile width decreases and the signal amplitude increases. Near the focus position, however, the lunar disk is resolved and the drift profile width is equal to the lunar disk diameter. From the lunar measurements the optimum subreflector position can be estimated as the center of the range, $+15 \text{ mm} > y > -10 \text{ mm}$, within which the lunar disk is resolved.

To determine the best subreflector position more precisely, a similar set of measurements were made of Saturn. Unlike the Moon, however, Saturn was observed using beam switching to modulate the incoming radiation because Saturn's angular diameter, $16''$ when these measurements were made, is much less than the beam size, $4'$. Furthermore, Saturn appears in only one of the switched beams at a time, so the beam profile may be directly mapped. In any event, beam switching is the only feasible modulation scheme for Saturn, since the planet's small size makes it a much weaker source than the Moon, even though their brightness temperatures at $\lambda = 2.1 \text{ mm}$ are similar.⁵⁰

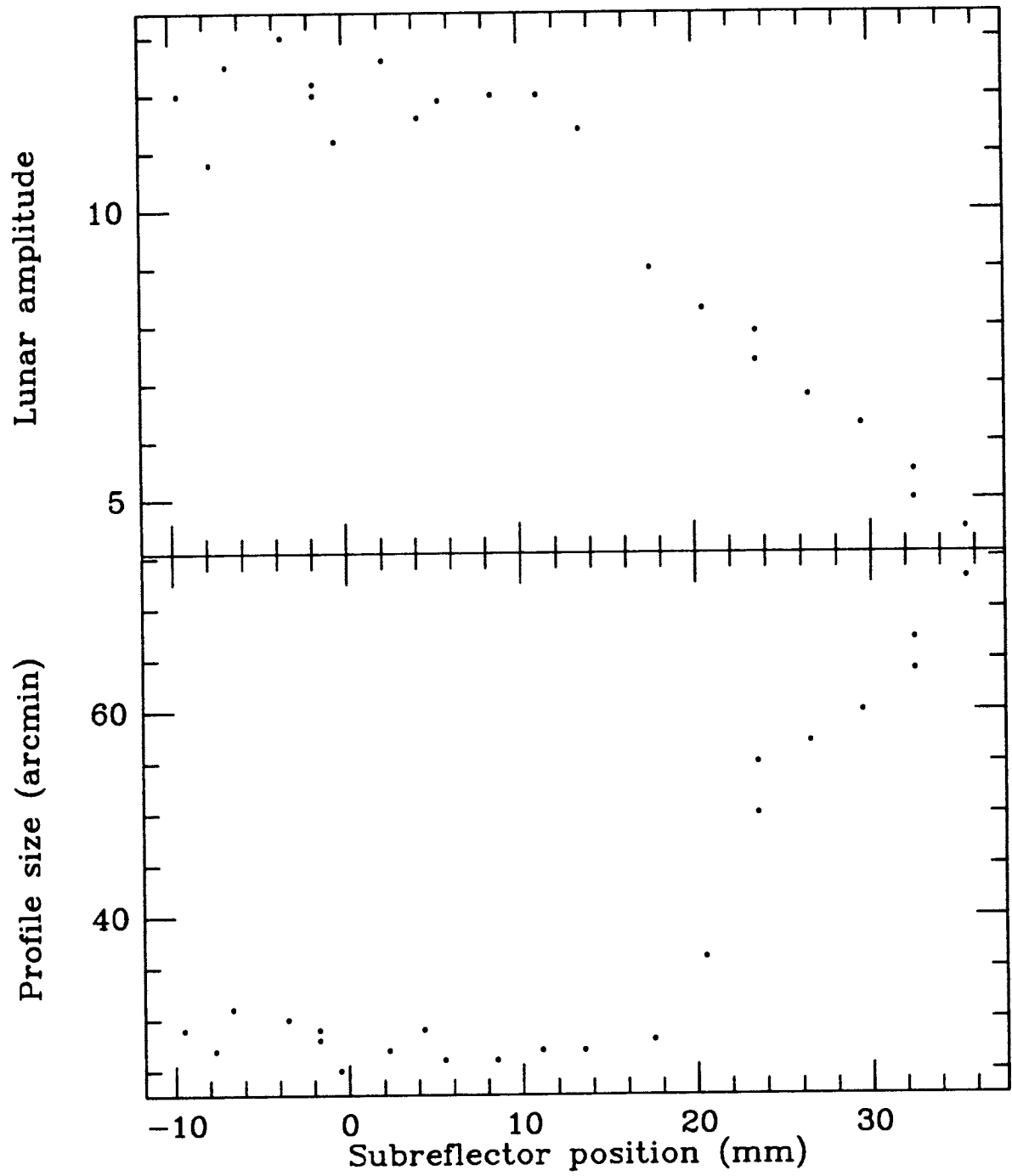


Figure 4.1. Amplitude and width of lunar drift scans vs. subreflector position.

Drift scans of Saturn were made the same way as the lunar observations, moving the subreflector between scans. Figure 4.2 shows the variations of the peak amplitude and of the scan profile width. During these scans, Saturn traversed a chord across the beam that was close, but not identical to the diameter. The measured scan profile width is, therefore, slightly smaller than the beam size. In figure 4.2, a minimum in the profile width is apparent near $y = 0$, † with an accompanying maximum in the amplitude. These extrema are about 2 mm wide, indicating the system's focal tolerance range. For the observations described below, $y = 0$ was chosen as the focus position.

Placing the detector at the telescope's Cassegrain focus to the required precision was accomplished with a steel measuring tape. A subsequent photometric test with Saturn confirmed this mechanical setting; moving the detector ± 10 cm along the optic axis reduced the signal strength less than 10%.

Beam profile

After determining the focus, a series of drift scans was made to characterize the beam profile. Twelve successive scans were averaged in order to increase the signal to noise ratio; figure 4.3 illustrates the result. Saturn is effectively a point source, so the drift scan profile directly maps the telescope beam pattern, which is well approximated by a Gaussian profile with FWHM $\theta_b \approx 3.5'$. At the time these scans were made, Saturn was near its meridian transit, so it appears in each of the switched beams sequentially during a scan. Because the parallactic angle was not exactly zero, though, Saturn traversed different chords through each beam and the signal amplitude in the minus beam is smaller.

† The zero point of y was defined *a posteriori*.

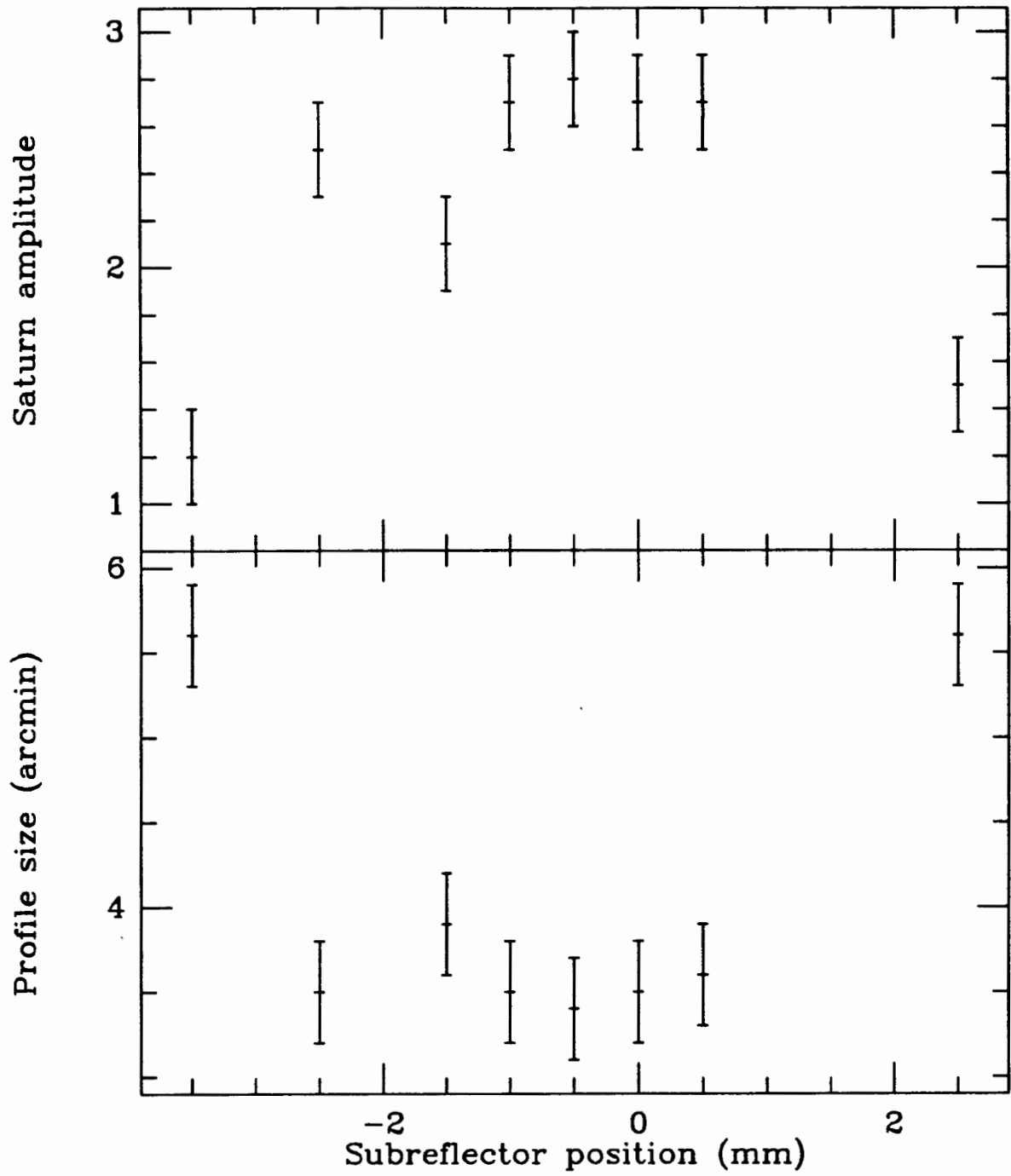


Figure 4.2. Amplitude and width of drift scans of Saturn vs. subreflector position.

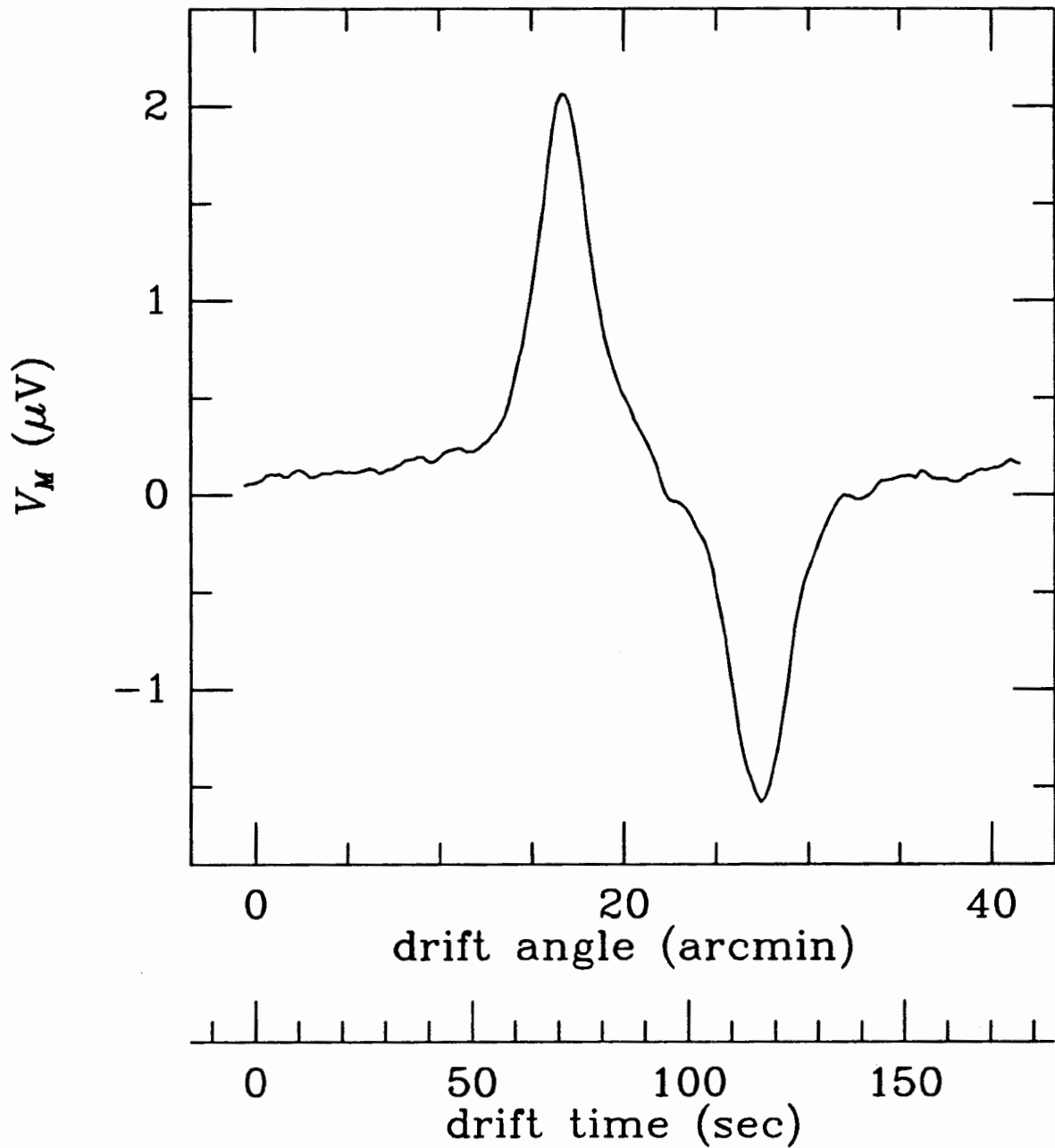


Figure 4.3. Average of twelve successive drift scans of Saturn shortly after transit on February 8, 1986, mapping the telescope beam profile. the angular scale was calibrated from the drift time using the relation $\Delta\alpha = \Delta t \cos \delta_S$, where $\delta_S = -20^\circ$ was Saturn's declination on that night.

The beam separation measured in these scans, $\theta_s = 11'$, was used to calibrate the secondary mirror nutation transducer. Also, these scans were used to determine the beam position relative to the optical boresight telescope cross hairs.

Calibration and Atmospheric Transparency

Further lunar observations were undertaken to determine the system's sensitivity to extended sources. Again, drift scans and load switching were used to make the observations. Since the beam diameter, $3.5'$, is much less than the lunar diameter, $30'$, the Moon fills the beam with a constant brightness source. The difference between the peak lunar signal and the atmospheric signal – the drift scan baseline – is

$$\begin{aligned} V_M &= \left\{ K \left[T_M e^{-\tau \sec z_M} + T_A \left(1 - e^{-\tau \sec z_M} \right) \right] + V_e \right\} \\ &\quad - \left\{ K \left[T_{\text{CBR}} e^{-\tau \sec z_M} + T_A \left(1 - e^{-\tau \sec z_M} \right) \right] + V_e \right\} \\ &\simeq K T_M e^{-\tau \sec z_M}, \end{aligned} \tag{4.1}$$

where V_M is the recorded voltage from the demodulator, K is the overall calibration constant to be determined, T_M , T_A , and T_{CBR} are the lunar, atmospheric, and cosmic background radiation brightness temperatures at $\lambda = 2.1$ mm, τ is the atmospheric opacity at the zenith, z_M is the zenith angle of the Moon during the observations, and V_e is a constant representing the emission from the eccosorb reference source.

The atmospheric transparency, τ , can be determined by measuring the variation of the atmospheric signal with zenith angle as the telescope is tipped from the zenith to $z = 60^\circ$,

$$\begin{aligned} V(z) &= K \left[T_A \left(1 - e^{-\tau \sec z} \right) + T_{\text{CBR}} e^{-\tau \sec z} \right] + V_e \\ &\simeq K T_A \left(1 - e^{-\tau \sec z} \right) + V_e. \end{aligned} \tag{4.2}$$

Since the range of $\sec z$ covered by the tipping runs is small, $1 \leq \sec z \leq 2$, equation 4.0 can be approximated by a linear equation,

$$V(z) = V_A \sec z + V_e, \quad 4.3$$

and the coefficient, $V_A = KT_A\tau'$, can be found from linear regression on the tipping results.

So long as they remain constant, the emission characteristics of the load switching reference source do not affect this procedure. If the atmospheric and lunar temperatures are known, the overall calibration, K , and the effective linear atmospheric opacity, τ' , are determined from the measured values of V_M and V_A . Then, if the atmospheric attenuation were small, $\tau \leq 0.1$, the true opacity would be $\tau \approx \tau'$. This was not the case, however, for these observations. In order to determine the true opacity, therefore, the true attenuation was set equal to the approximate linear attenuation at the center of the tipping range, $\sec z_c = 1.5$. Then K , τ , and τ' were determined by simultaneous solution of the system of equations.

$$V_M = KT_M e^{-\tau \sec z_M}, \quad V_A = KT_A \tau', \quad \text{and} \quad \tau' \sec z_c = 1 - e^{\tau \sec z_c}. \quad 4.4$$

The primary source of atmospheric emission at $\lambda = 2.2$ mm is water vapor in the troposphere, which has a thermodynamic temperature of $T_A = 10 \pm 10 \text{ C} \approx 280 \pm 10 \text{ K}$, under typical atmospheric conditions.⁵¹ Since it leads to fractional uncertainties of less than 1% in K and less than 4% in τ , the uncertainty in the atmospheric temperature is unimportant.

At millimeter wavelengths, the lunar brightness temperature varies significantly with lunar phase. Measurements at $\lambda = 3.1 \text{ mm}$ ⁵² and at $\lambda = 1 \text{ mm}$ ⁵³ show a minimum temperature just prior to the lunar dawn and indicate the emissive material

has a thermal time constant of several days. The new Moon brightness temperature measured at $\lambda = 2.1$ mm, is $T_M(\text{new}) = 145$ K.⁵¹ Since no observations of the full moon at this wavelength are published, interpolation between the $\lambda = 3.1$ mm and the $\lambda = 1$ mm measurements was used to estimate the full Moon temperature, $T_M(\text{full}) = 340$ K (fig. 4.4). For the new Moon, the interpolated and measured temperatures agree very well, confirming the method.

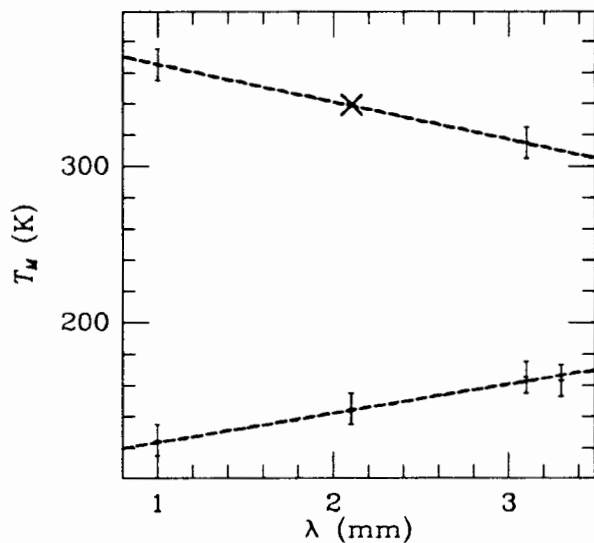


Figure 4.4. Interpolation of the full moon brightness temperature at $\lambda = 2.1$ mm, $T_M = 340$ K from $\lambda = 3.1$ mm⁵³ and $\lambda = 1$ mm⁵⁴ measurements (top line). Measured new Moon brightness temperatures at those wavelengths and at $\lambda = 2.1$ mm⁵¹ and $\lambda = 3.3$ mm⁵⁴ are also shown (bottom line).

Lunar calibrations made on four nights that bracket the dates of anisotropy observations are summarized in table 4.1. Three nights were just before full moons, and drift scans on these nights show a marked gradient across the lunar disk. This is expected, as one edge of the moon had been lit for the entire lunar day while the other edge had only recently been illuminated. In these cases, the maximum amplitude of the drift scan was taken for V_M , and the full moon temperature was used. The three nights' calibrations agree within 16%.

The remaining calibration night was just after a new moon, and this night's drift scan shows a uniform lunar temperature. An anomalously large value of K results, however, if the new moon temperature is used to calculate this night's system calibration. Indeed, to make this night's K consistent with the other three calibration nights, the full moon temperature must be used in the calculation. The last three lines of table 4.1 explore the effect on this night's K of assuming different values of T_M . The most likely explanation of this discrepancy is the large zenith angle of the lunar measurement, $z_M = 69^\circ$. This is well outside the tipping measurement range so a small error in determining V_A could have a large effect on the resulting value of K . For these reasons, this measurement was not used to calibrate the anisotropy data.

Both as a check of photometer sensitivity and because the Moon was not visible on the majority of the anisotropy observation nights, a secondary calibration measurement was made on all nights. A styrofoam bucket filled with steel wool and liquid nitrogen was placed in front of the photometer's aperture, filling its field view. Radiation from this cold load was modulated with the load switching chopper wheel. The secondary calibration coefficient, K' , was then calculated as the ratio of the voltage measured with this arrangement to the nominal temperature difference, 200 K, between the cold load and the ambient temperature Eccosorb reference source.

The average of the ratio of primary to secondary calibrations on the three full moon calibration nights was $\langle K/K' \rangle = 0.63$. In conjunction with the K values on the observation nights, this average ratio was used to calibrate the anisotropy data and determine the atmospheric opacity. This ratio also gives a rough measure of the telescope efficiency, but its physical significance should be taken in a spirit of *caveat emptor* since, for example, the angle subtended by the secondary calibration

Table 4.1. System Calibrations and Atmospheric Opacity

Observation Date	Anisotropy Observations?	Lunar Illumination	Lunar Zenith Angle z_M	Lunar Temperature T_M	Lunar Signal V_M (μV)	Tip Slope V_A (μV)	Lunar Calibration K ($\mu\text{V/K}$)	Secondary Calibration K' ($\mu\text{V/K}$)	Calibration Ratio K/K'	Linear Atmospheric Opacity τ'	True Atmospheric Opacity τ
1/26/86	No	100%	40°	340 K	163	91	0.92	1.33	0.69	0.35	0.50
3/20/86	Yes	63%	30°	340 K	180	80	0.88	1.51	0.58	0.32	0.44
3/22/86	No	80%	50°	340 K	200	80	1.03	1.65	0.62	0.28	0.36
4/ 3/86	Yes	79	...	1.71	(0.63)	0.26	0.33
4/ 6/86	Yes	60	...	1.85	(0.63)	0.18	0.21
4/ 7/86	Yes	117	...	1.86	(0.63)	0.36	0.51
4/ 8/86	Yes	110	...	1.53	(0.63)	0.41	0.63
4/14/86	No	20%	69°	150 K	60	107	1.25	1.60	0.78	0.30	0.41
4/14/86	No	20%	69°	200 K	60	107	1.13	1.60	0.70	0.34	0.47
4/14/86	No	20%	69°	340 K	60	107	0.96	1.60	0.60	0.40	0.61

cold load may not have been exactly the same as that subtended by the secondary mirror. Even though systematic effects of this nature were not addressed, the secondary calibration provides a reliable estimate of the system sensitivity on those nights when the lunar calibration was not possible.

The beam profile observations of Saturn on February 8, 1986, provide a further check on the system calibration. Except that Saturn is much smaller than the beam and that beam switching was used, the calibration calculation is the same as in the lunar case. The drift scan amplitude is

$$\begin{aligned}
 V_S &= K_S \left[T_S \frac{\Omega_S}{\Omega_b} e^{-\tau \sec z_S} + T_{\text{CBR}} \left(1 - \frac{\Omega_S}{\Omega_b} \right) e^{-\tau \sec z_S} + T_A \left(1 - e^{-\tau \sec z_S} \right) \right] \\
 &\quad - K_S \left[T_{\text{CBR}} e^{-\tau \sec z_S} + T_A \left(1 - e^{-\tau \sec z_S} \right) \right] \\
 &\simeq K_S T_S \frac{\Omega_S}{\Omega_b} e^{-\tau \sec z_S}, \tag{4.5}
 \end{aligned}$$

where Ω_S and Ω_b are the solid angles of Saturn and the telescope beam, respectively, and $T_S = 165 \pm 10 \text{ K}$ at $\lambda = 2.1 \text{ mm}$.⁵² Using the same equations for the atmospheric opacity gives the results listed in table 4.2, in general agreement with the lunar calibrations. It should be noted, however, that the Saturnian calibration K_S , is directly proportional to the assumed beam solid angle, so underestimating Ω_b also underestimates K_S .

Atmospheric Noise Reduction

The effectiveness of higher order, high frequency beam switching in suppressing atmospheric noise is illustrated by comparison measurements made on April 14, 1986. For these tests, the beam switching angle was $\theta_s = 10'$, the modulation frequency was $f_s = 10 \text{ Hz}$, and the telescope was pointed at the north celestial pole

Table 4.2. Saturn Observation of February 8, 1986

Zenith angle	z_S	55°
Solid angle of Saturn	Ω_S	$186 (\text{arcsec})^2$
Solid angle of the beam	Ω_b	$18 (\text{arcsec})^2$
Saturnian signal	V_S	136 nV
Tip slope	V_A	$99.5 \mu\text{V}$
Saturnian calibration	K_S	$0.87 \mu\text{V/K}$
Secondary calibration	K'	$1.84 \mu\text{V/K}$
Calibration ratio	K_S/K'	0.5
Linear atmospheric opacity	τ'	0.41
Atmospheric opacity	τ	0.64

($z = 90^\circ - \text{north latitude} = 43.6^\circ$). The results for single and double differencing are shown in figure 4.5, together with the intrinsic detector noise, which was measured with the modulator operating by blocking the photometer entrance aperture with a brass plate. Relative to the single differencing noise level, $50 \text{ nV}/\sqrt{\text{Hz}}$, the double differencing noise level, $13 \text{ nV}/\sqrt{\text{Hz}}$, was a factor of almost four smaller, and was not significantly larger than the detector noise, $10 \text{ nV}/\sqrt{\text{Hz}}$. On the basis of these photometric tests, double differencing appears to provide adequate noise suppression under typical atmospheric conditions.

Anisotropy Observations

Observations of the cosmic background radiation were undertaken on five nights in late March and early April, 1986. These dates were the first period with acceptable weather conditions following completion of the photometric tests described

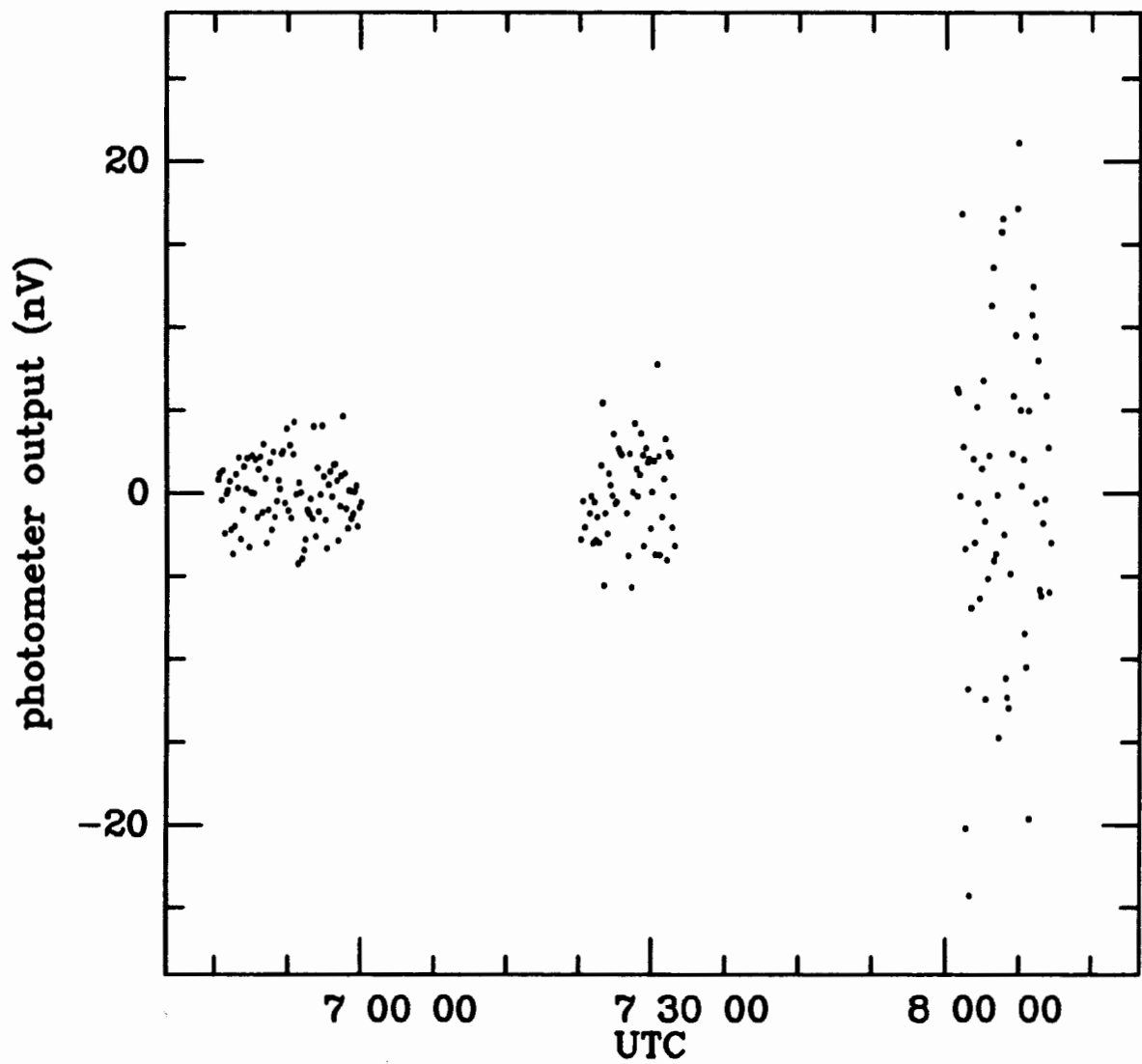


Figure 4.5. Comparison of intrinsic detector noise (left) with double and single differencing (center and right, respectively). The data points are 10s integrations of the demodulated photometer output, expressed as brightness temperature differences above the atmosphere.

above. In mid-April, operating funds were exhausted, precluding further observations. This section describes the observing particulars; the results of the measurements are discussed in the next chapter.

Sampling Pattern: Double difference beam switching was used together with single difference telescope wobbling. The beam switching frequency and angle were $f_s = 10\text{ Hz}$ and $\theta_s = 10'$, the maximum values at which the nutation mechanism could reliably operate. The wobble frequency, $f_w = (4^m 20^s)^{-1}$, represents a compromise between the better suppression of instrumental noise possible at higher frequencies and the reduced telescope overhead at lower frequencies. Although the intended wobble angle was the switching angle, $10'$, the actual wobble angle was $\theta_w = 6.9'$ due to miscalculation of the necessary azimuth movement. This caused misalignment of the sampling pattern's central spots (fig. 4.6), resulting in reduction of the pattern's statistical efficiency.

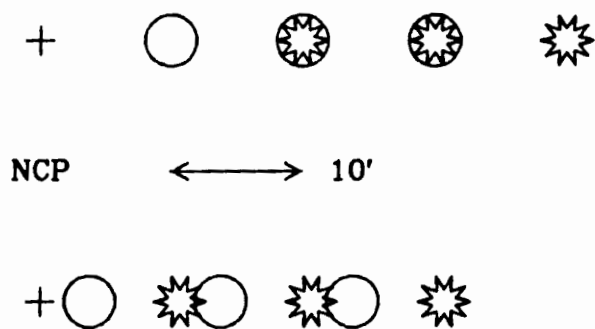


Figure 4.6. Intended switching and wobbling pattern (top) and actual sampling pattern. High frequency (10 Hz) beam switching takes place between the three spots in each group, and low frequency $(4^m 20^s)^{-1}$ telescope wobbling between the circled and starred groups.

In the notation of chapter 2, the power transfer function of the filter defined by the misaligned sampling pattern is (fig. 4.7)

$$\tau_{2+1}(k) = \pi^{-2} \sin^4(k_x \theta_s / 2) \sin^2(k_x \theta_w / 2) \exp(-k^2 \theta_b^2 / 8 \ln 2), \quad 4.6$$

and its autocovariance is (fig. 4.8)

$$C_{2+1}(\theta) = \frac{\ln 2}{8\pi\theta_b^2} \sum_{j=-2}^2 \sum_{j'=-1}^1 (-1)^{j+j'} \binom{4}{2-j} \binom{2}{1-j'} \\ \times \exp \left\{ - \left[\theta_y^2 + (\theta_x - j\theta_s - j'\theta_w)^2 \right] \frac{2 \ln 2}{\theta_b^2} \right\}. \quad 4.7$$

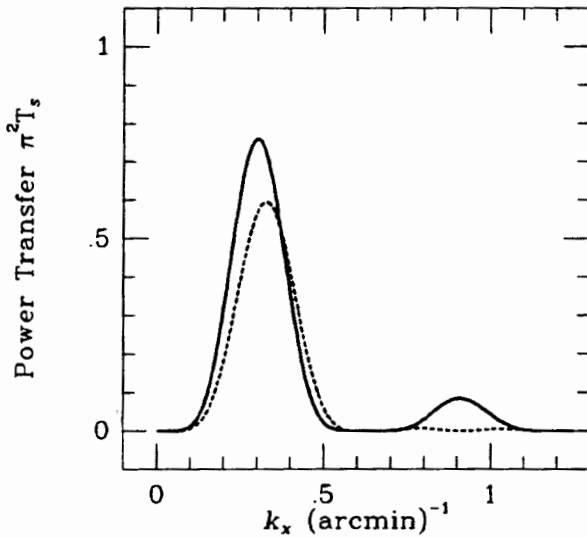


Figure 4.7. The power transfer function of the intended sampling pattern (solid curve) and of the actual, misaligned pattern (dashed curve). The intended wobbling angle is $\theta_w = 10'$, while it is $\theta_w = 6.9'$ in the misaligned pattern. In both cases, $\theta_b = 4'$ and $\theta_s = 10'$.

The major effects of this misalignment, apparent in figure 4.8, are reduction of the effective sampling scale to about $8'$ and reduction of the overall sampling coefficient, β , to about three quarters the coefficient for the aligned pattern in the context of models of a cold dark matter dominated universe.⁵⁵ The resulting sky sampling pattern is shown in figure 4.9.

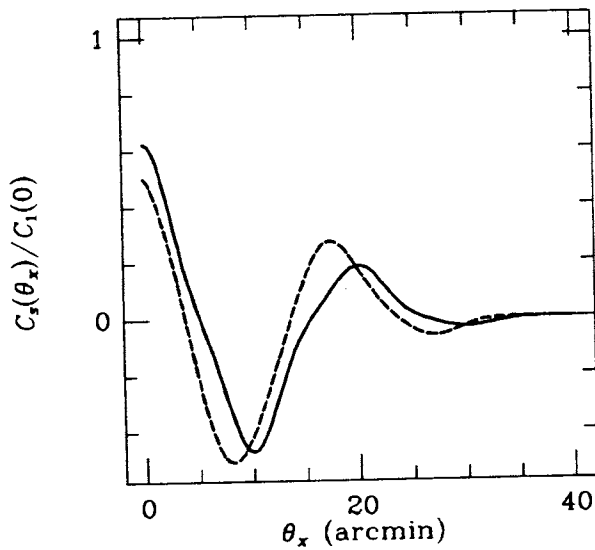


Figure 4.8. The spatial autocovariance of the intended sampling pattern (solid curve) and of the actual, misaligned pattern (dashed curve). The intended wobbling angle is $\theta_w = 10'$, while it is $\theta_w = 6.9'$ in the misaligned pattern. In both cases, $\theta_b = 4'$ and $\theta_s = 10'$.

Observing Sequence: During these observations, the data acquisition system integrated each sample of the demodulated photometer output for 10 s. Since the time constant of the lockin amplifier output filter was set at $\tau_{TC} = 1.25$ s, the effective integration time for each sample was 12.35 s. Groups of 13 samples were recorded together as a scan, and wobbling occurred after every second scan:

L R R L L R R L L R R L L R R L L R R L,

where *L* and *R* are the left and right wobble positions. After every 20 scans, the telescope was moved to an independent region of the sky on the other side of the pole. Each region was observed once per night.

A total of 36 hrs of usable data, spread over 10 sky regions, was recorded according to this sequence during the five nights of CBR observation. The analysis of that data is discussed in the next chapter.

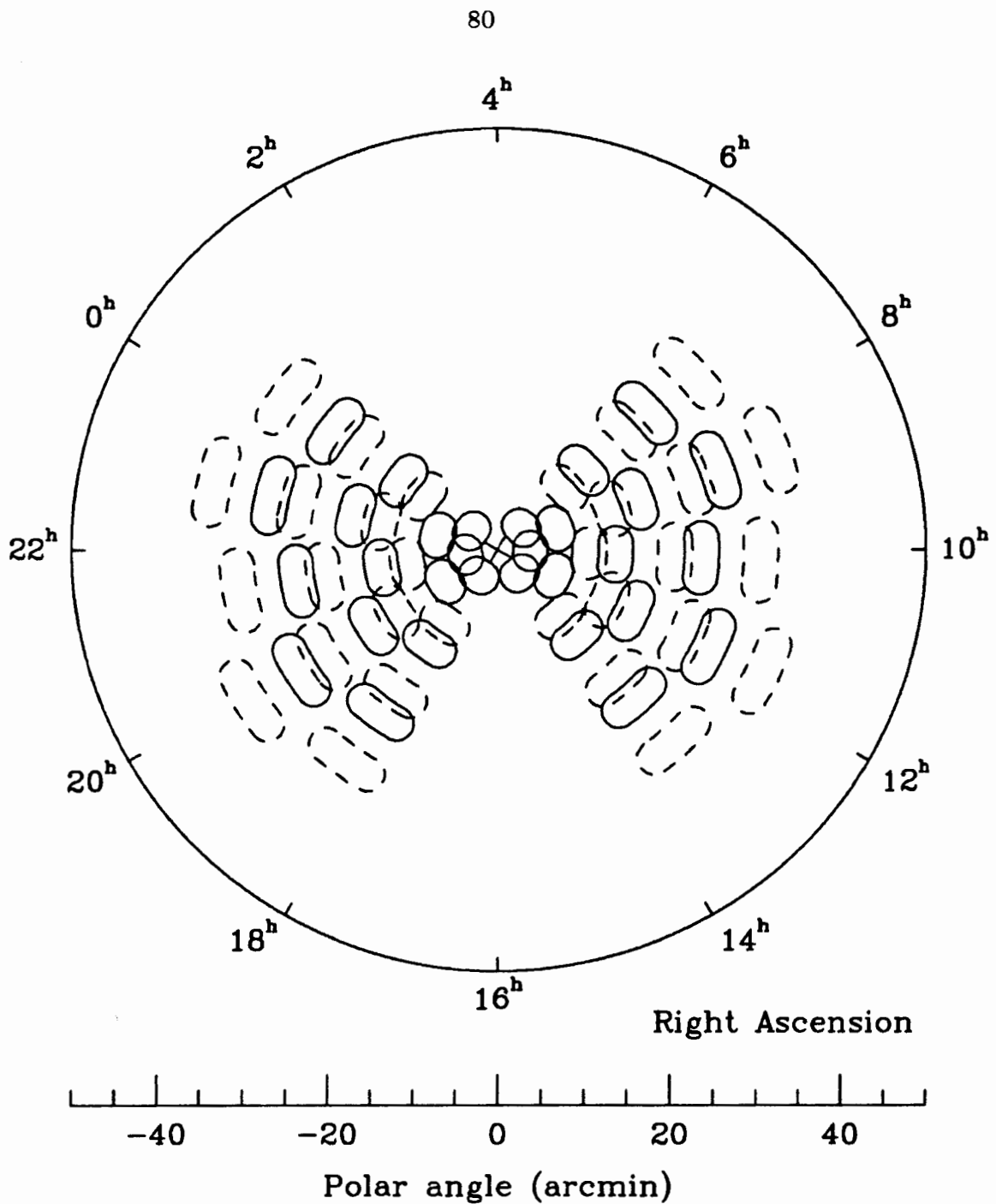


Figure 4.9. Actual sky sampling pattern used in anisotropy observations. Due to miscalculation of the necessary amount of azimuth motion, the wobbled beams do not overlap properly, and the overall pattern is more compact than intended. The beam size $\theta_b = 4'$, the switching angle $\theta_s = 10'$, and the wobble angle $\theta_w = 6.9'$.

Chapter 5. Data Analysis

To determine the amplitude of fine scale CBR anisotropies, or an upper limit to the amplitude if none are detected, the data were analyzed by the procedure described in this chapter.

Each night's raw data are a time series of integrated samples of the filtered lock-in output voltage that represent the demodulated photometer signal. The following analysis steps were performed on these data:

- Deleting those samples contaminated by electronic interference;
- Calculating the average voltage for each scan;
- Removing the low frequency drift in the instrumental offset by subtracting a best fit polynomial from each night's time series of scan averages;
- Demodulating the telescope wobble motion for each pair of successive scans by subtracting the right scan's average voltage from that of the left scan;
- Calculating the average voltage difference within each sky region;
- Calibrating each night's measurements;
- Averaging all the night's observations of each region; and
- Applying a statistical hypothesis test to determine the presence of fine scale anisotropies.

Preliminary Analysis

The results of the first six, preliminary analysis steps, applied independently to each night's data, are presented graphically in figures 5.2 through 5.6 and described below.

Data Editing: A small percentage of the data samples were contaminated by electronic interference. For instance, on several occasions the photometer preamplifier output displayed large voltage “spikes” of unknown origin. These spikes were always in pairs, first positive, then negative – or vice versa – with a time delay between the two spikes that varied from 0.2s to 10s. When a spike occurred, it would saturate the lock-in amplifier’s output, resulting in an outlying sample. Since this problem occurred whether or not the photometer entrance aperture was covered, it is a purely instrumental effect and deleting the contaminated samples is justified. Also, starting and stopping the hydraulic drive’s pump motor when the telescope was wobbled produced electrical transients that sometimes caused similar spikes in the preamplifier output.

To remove samples contaminated by this sort of problem, a “shaver” was constructed to delete outlying samples. When applied to a night’s time series of raw data samples, this shaver first subtracted the best fit cubic polynomial and then joined together the ends of the series to form a circular list. Next, each point was tested in turn against the mean and sample variance of those neighboring points lying within a sliding window centered on the test point (fig. 5.1). Two constraints were used to determine the boundaries of this window. First, since the outlying samples showed a positive correlation on short time scales, the five points on either side of the test point were excluded from the window. Second, drifts in the instrumental offset that remain after subtracting the cubic polynomial inflate the variance on long time scales. An outer window boundary of ± 20 points is small enough to avoid this drift problem, yet large enough to provide adequate stability in the variance estimate. If the test point was more than three standard deviations from the mean in this window, the point was deleted. For data drawn from a true Gaussian population less than 0.3% of the samples should have been deleted by this

shaving; in practice, between 0.8% and 3.1% of them were. The shaving procedure was applied only once to each time series.

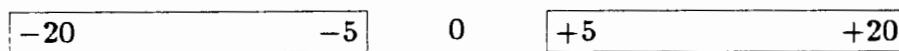


Figure 5.1. Window used in the shaving procedure to calculate the local mean and variance for deleting outliers. The window was centered on the test point and the points within the boxes included in the calculation.

Scan Averaging: Next, an unweighted average of the samples within each scan was computed, $v_{i\bullet} = \sum_j v_{ij}/J_i$, where v_{ij} are the edited voltage samples, $v_{i\bullet}$ is the average voltage in scan i , and J_i is the number of samples in that scan. Because of outlier deletion, not all the scans had the same number of samples, so the number of samples entering into each scan average was recorded at this step for reference in later steps.

Computed for each scan individually, the sample variance, $s_i^2 = \sum_j (v_{ij} - v_{i\bullet})^2 / (J_i - 1)$, is rather unstable, since so few samples go into each average ($J_i \leq 13$). Other than the variation due to deleted samples, however, there is no *a priori* reason to expect the variances of the scan averages to be different. Therefore, a more stable estimate of the variance was computed by pooling the data from all of the

scans to get the average sample variance

$$\tilde{s}^2 = \sum_i \frac{s_i^2}{I} = \sum_i \frac{\sum_j (v_{ij} - v_{i\bullet})^2}{I(J_i - 1)}, \quad 5.1$$

where I is the total number of scans. The variance of each scan average was then assigned by dividing this pooled variance by the number of samples in the scan, $\tilde{s}_i^2 = \tilde{s}^2/J_i$. It is important to note that the variance estimated by this pooling process does not contain information about the variation between the scan averages, but only information about the variation among the samples within each scan.

Polynomial Fitting: Very low frequency instrumental noise of the type discussed in Chapter 2 produced slow drifts in the instrumental offset during the measurements. Telescope wobbling and subsequent demodulation define a filter that attenuates this noise component, but if the noise spectrum is sufficiently red, low frequency noise power will still leak through this filter. Removing a polynomial trend from each night's time series of scan averages before demodulating the telescope wobble is the most effective means of reducing the effects of these offset drifts. This trend removal will not attenuate a true differential signal because the telescope wobbling time scale is much shorter than the time scale of the highest order polynomial term.

To determine the appropriate polynomial, successively higher order polynomials were fit to each time series until the variance of the residuals reached a constant value. In cases where there were discrete shifts in the offset – due, for instance, to readjustment of the lock-in amplifier's offset control to keep the signal on scale – separate constant terms were used before and after the shift, but all other terms were held common across the shift. In the resulting best fit polynomials, the power

of the highest order term was between 10 and 20, and there were 200 to 300 degrees of freedom in each fit.

Wobble Demodulation: During the observations the telescope was wobbled every other scan between a *left* and a *right* position. To demodulate this motion, the voltage difference between each pair of successive scans was computed by subtracting the right scan's average voltage from that of the left scan,

$$\Delta v_{i\bullet} = \frac{1}{2}(-1)^i (v_{(2i)\bullet} - v_{(2i-1)\bullet}). \quad 5.2$$

Here the even scans, $v_{(2i)\bullet}$, are the right scans, the odd scans, $v_{(2i-1)\bullet}$, are the left ones, and the factor $(-1)^i$ accounts for the *L R R L* wobble pattern. For calculating the total integration time, the accumulated number of samples in each difference was taken as the sum of the number of samples in each constituent scan. Then the factor of one half gives the same amplitude normalization as in the discussion of the sampling coefficient in Chapter 2.

Region Averages: All the differences obtained in each sky region on each night were then averaged in the same manner as the scan averages were calculated, $\Delta v_{nr\bullet\bullet} = \sum_i \Delta v_{nri\bullet} / I_{nr}$, where labels for the observation night, n , and sky region, r , have been introduced, and I_{nr} is the number of differences recorded in a particular sky region. Again, the data were pooled to provide a reliable variance estimate.

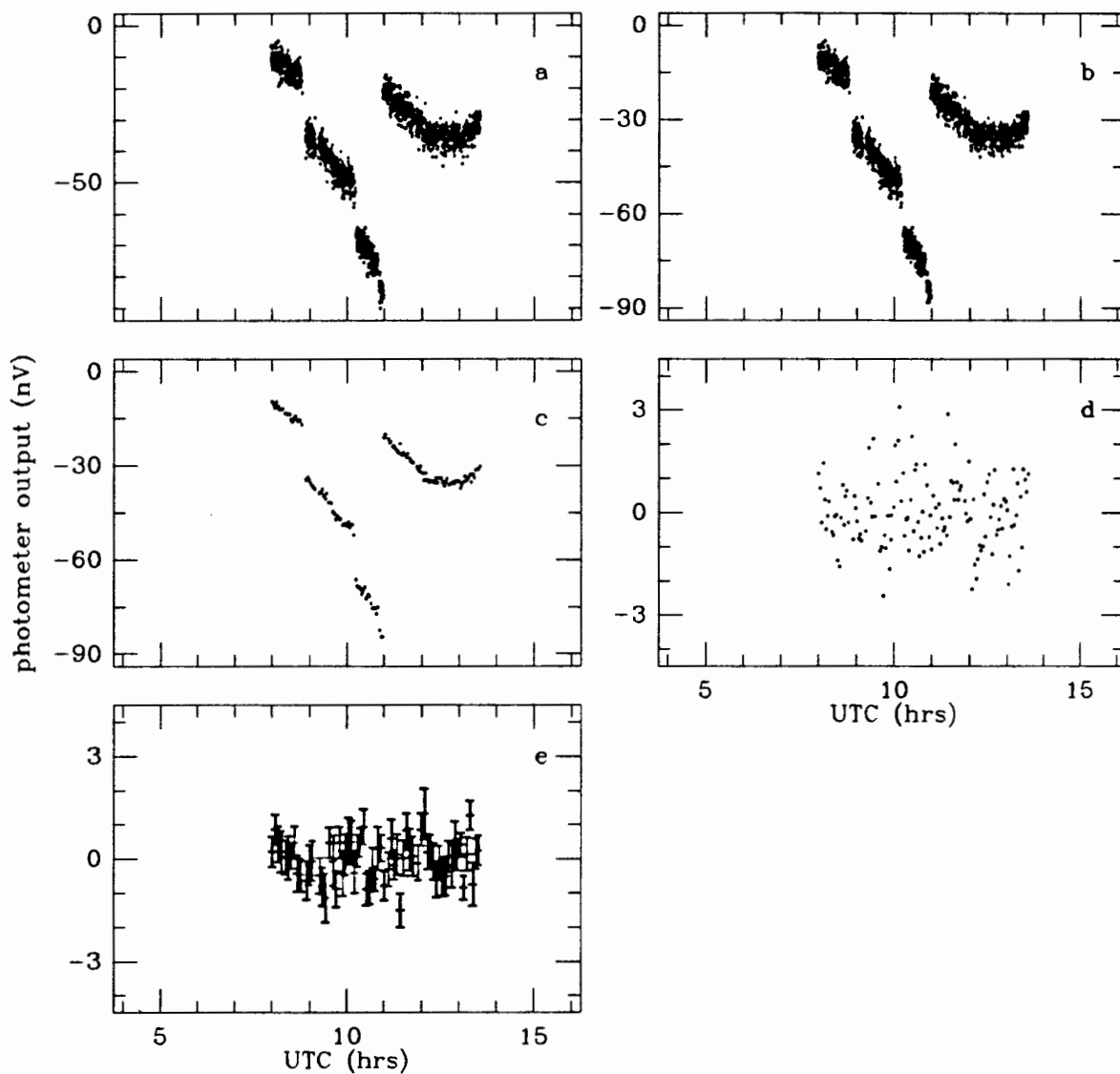


Figure 5.2. Preliminary analysis steps for data of March 20, 1986. Panel (a) is the raw data, panel (b) is the data after outlier deletion, panel (c) is the average voltage in each scan, panel (d) is the residuals after subtracting the best fit polynomial, and panel (e) is the differences between successive left and right scans after demodulating the telescope wobble motion.

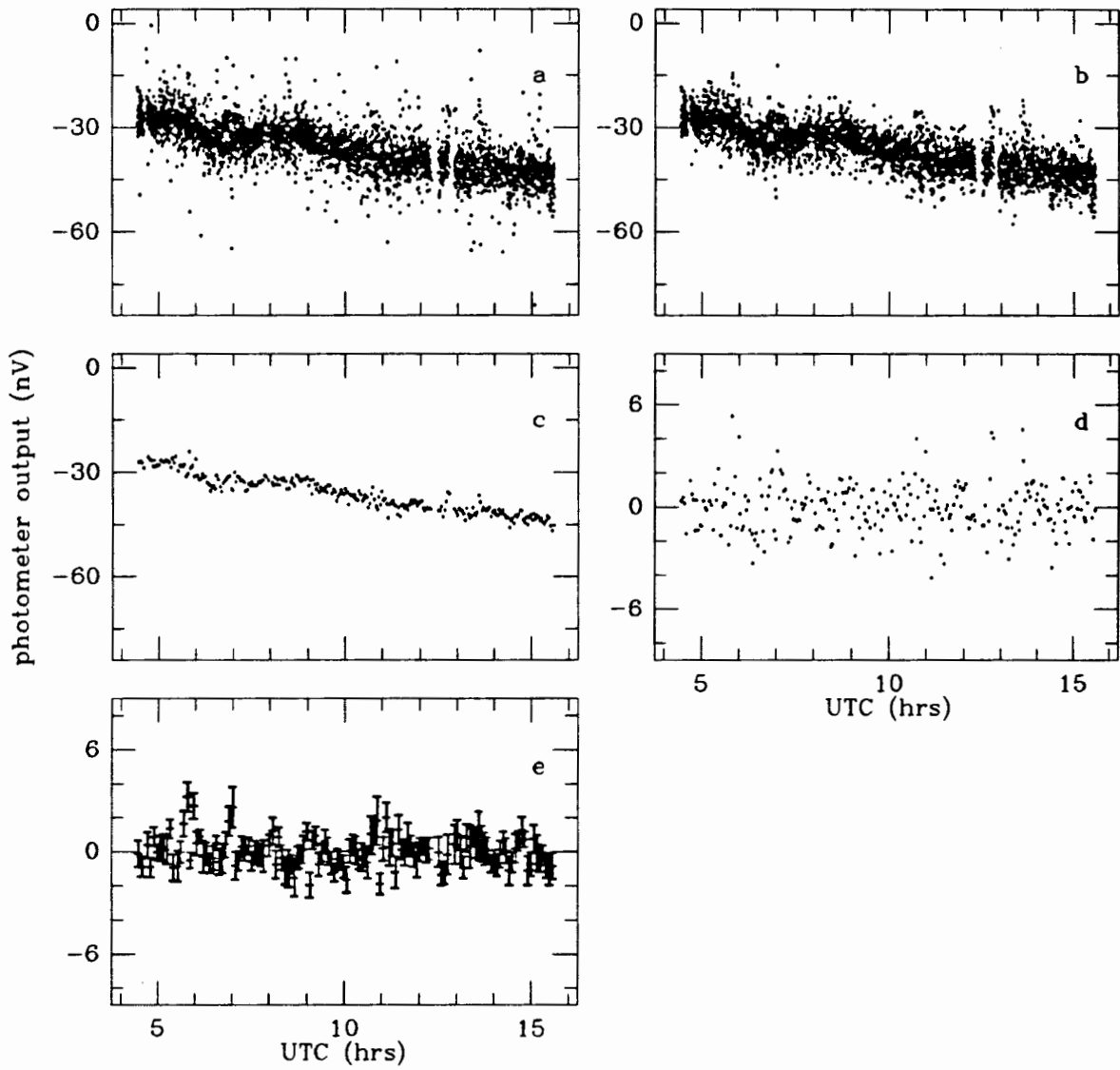


Figure 5.3. Data analysis steps for data of April 3, 1986. Panel (a) is the raw data, panel (b) is the data after outlier deletion, panel (c) is the average voltage in each scan, panel (d) is the residuals after subtracting the best fit polynomial, and panel (e) is the differences between successive left and right scans after demodulating the telescope wobble motion.

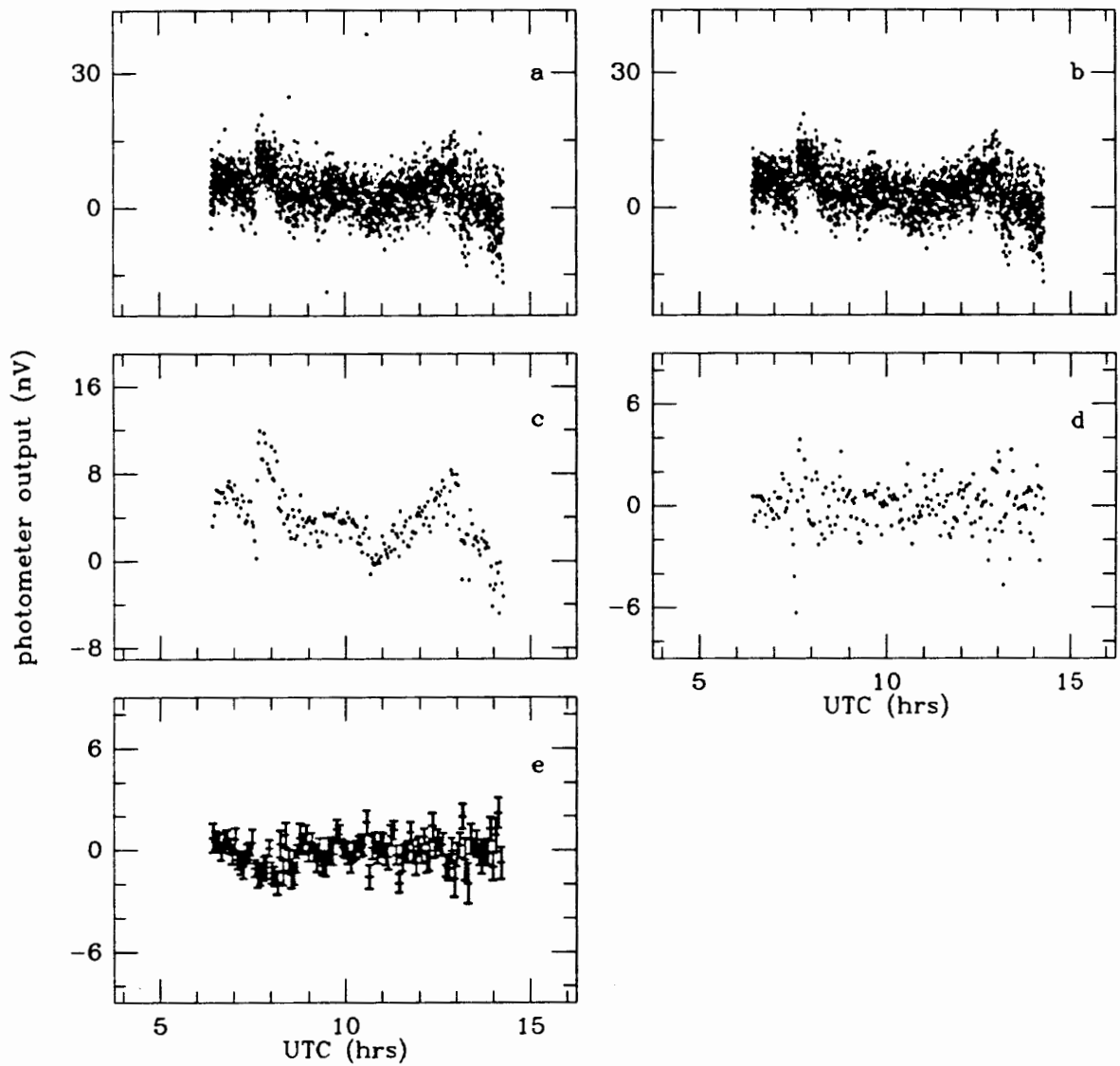


Figure 5.4. Data analysis steps for data of April 6, 1986. Panel (a) is the raw data, panel (b) is the data after outlier deletion, panel (c) is the average voltage in each scan, panel (d) is the residuals after subtracting the best fit polynomial, and panel (e) is the differences between successive left and right scans after demodulating the telescope wobble motion.

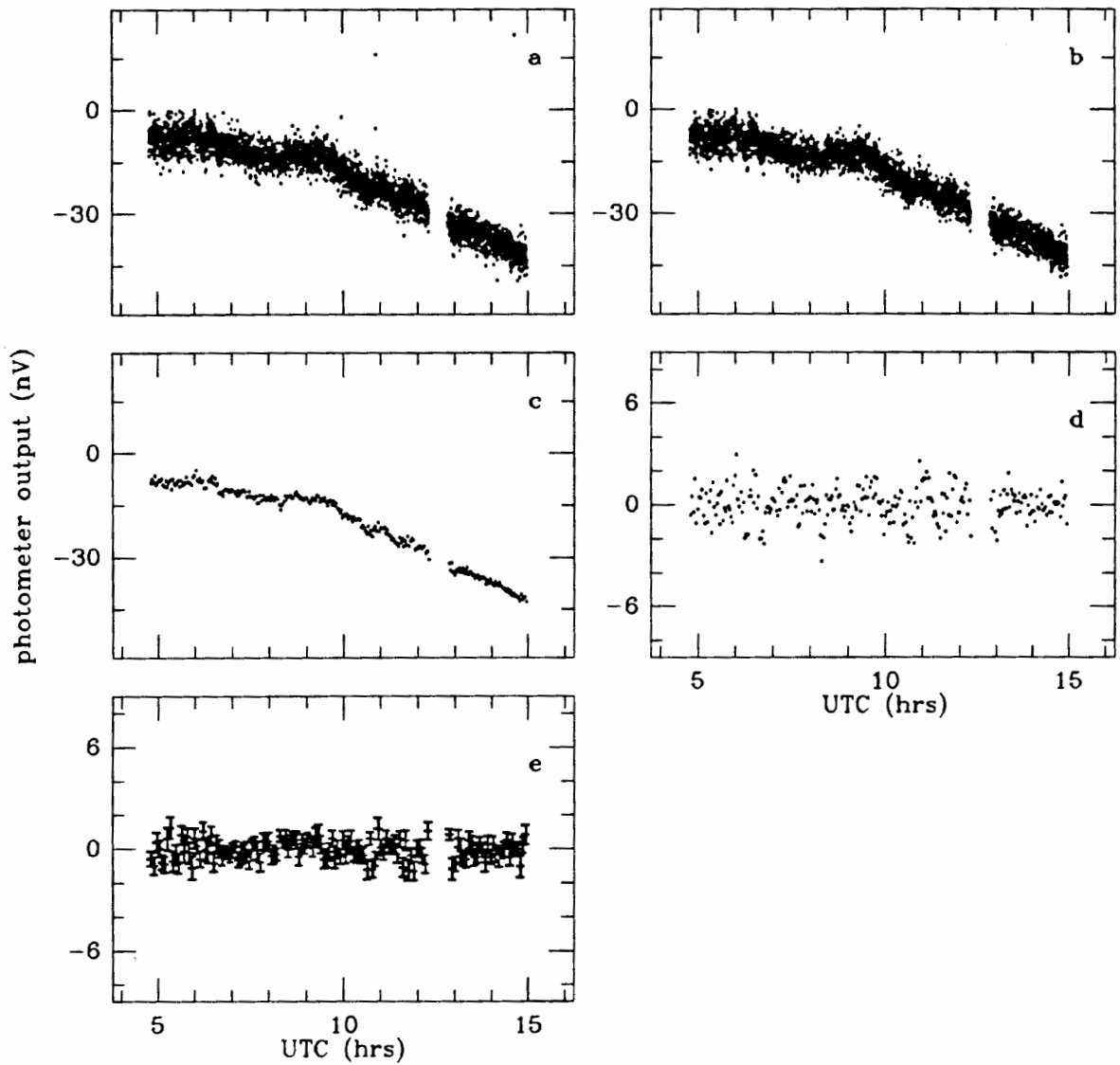


Figure 5.5. Data analysis steps for data of April 7, 1986. Panel (a) is the raw data, panel (b) is the data after outlier deletion, panel (c) is the average voltage in each scan, panel (d) is the residuals after subtracting the best fit polynomial, and panel (e) is the differences between successive left and right scans after demodulating the telescope wobble motion.

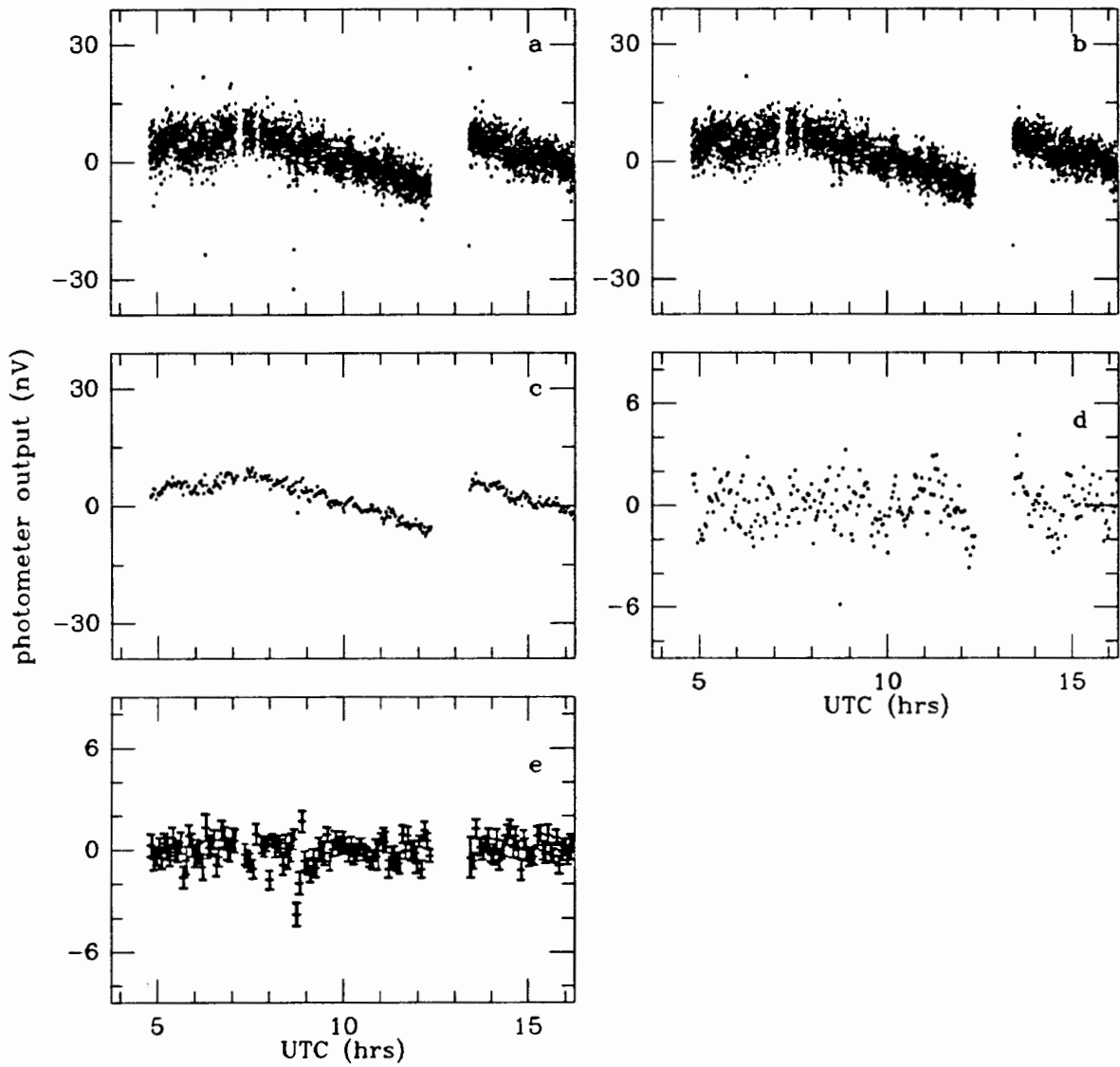


Figure 5.6. Data analysis steps for data of April 8, 1986. Panel (a) is the raw data, panel (b) is the data after outlier deletion, panel (c) is the average voltage in each scan, panel (d) is the residuals after subtracting the best fit polynomial, and panel (e) is the differences between successive left and right scans after demodulating the telescope wobble motion.

Calibration: On each observing night the calibration measurements discussed in the last chapter were made to determine the system calibration constant, K_n , and the atmospheric opacity, τ_n (table 4.1). These quantities were used to refer the anisotropy observations to a point above the atmosphere and express the data as an average Rayleigh-Jeans equivalent brightness temperature difference for each region on each night, $\Delta T_{B,nr} = \Delta v_{nr}/K_n e^{-\tau_n \sec z}$, where the dots indicating the earlier averaging have been dropped. Here $z = 43.6^\circ$ is the zenith angle of the sky region, which is just the zenith angle of the north celestial pole, 90° minus the the telescope's geographic latitude. Using the conversion presented in chapter 2, these average brightness temperature differences were expressed as fractional fluctuations in the CBR's thermodynamic temperature,

$$y_{nr} \equiv \Delta T_{nr}/T_{\text{CBR}} = \Delta T_{B,nr}(e^x - 1)^2 / (x^2 e^x T_{\text{CBR}}) = 0.57 \text{ K}^{-1} \Delta T_{B,nr} \quad 5.3$$

at $\lambda = 2.2$ mm. These fractional differences are shown in figure 5.7.

Night Averaging: All the nights' data were then combined by averaging the temperature differences for each region. Because there is a substantial night to night variation in the instrumental noise level, this averaging was weighted by the inverse variance of the data points. The resulting regional averages,

$$y_{\bullet r} = \left(\sum_n y_{nr} / \tilde{s}_{nr}^2 \right) / \left(\sum_n 1 / \tilde{s}_{nr}^2 \right), \quad 5.4$$

are shown in figure 5.8 together with their standard deviations, $s_r = \left(\sum_n 1 / \tilde{s}_{nr}^2 \right)^{-1/2}$.

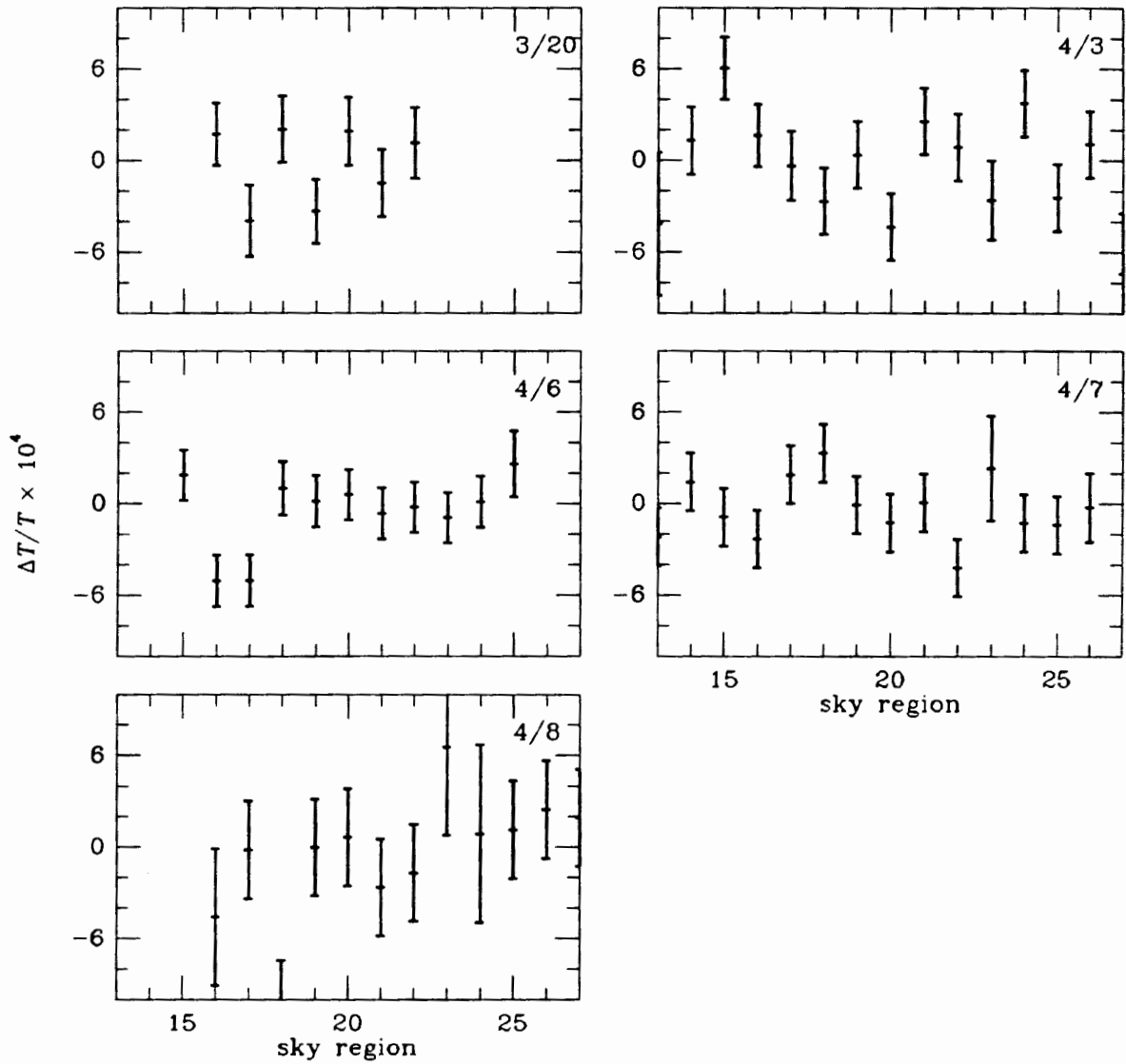


Figure 5.7. The fractional temperature differences for each region on each observing night, y_{nr} .

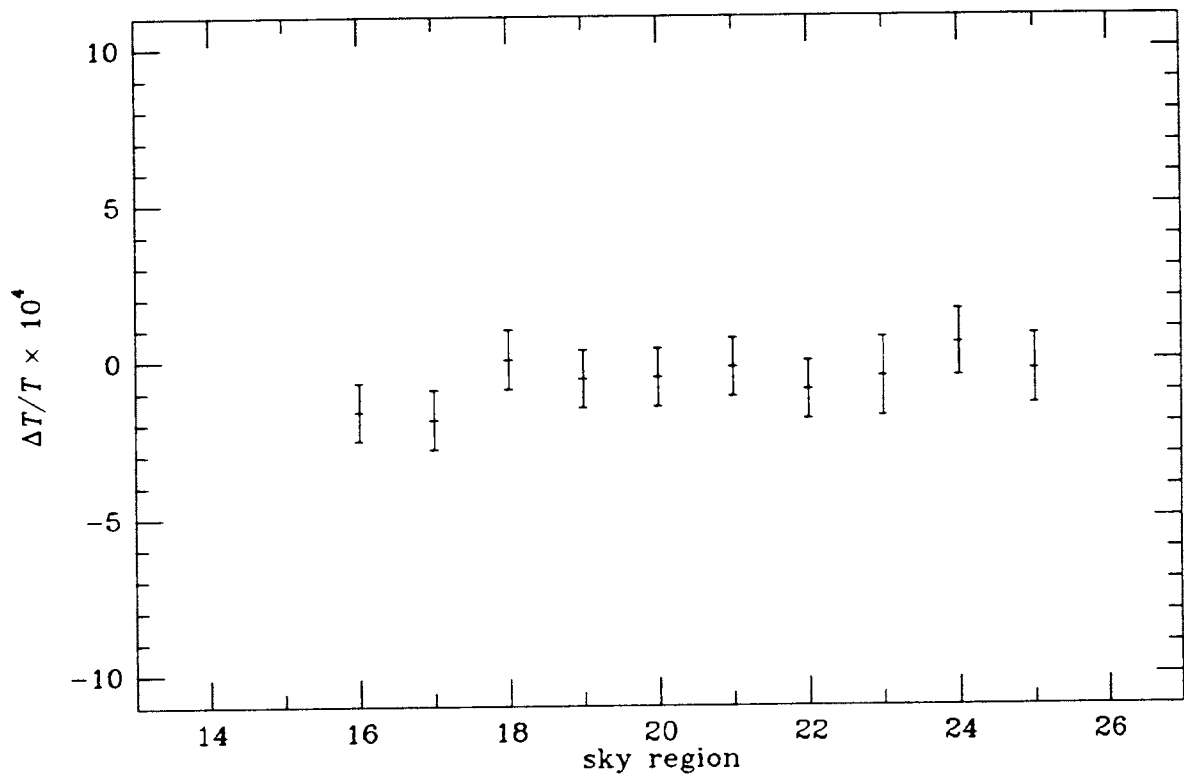


Figure 5.8. The fractional temperature difference for each region, averaged over all the nights, y_{er} .

Hypothesis Test

Since the data contributing to each point in figure 5.8 are from observations of one sky region only, the error bars on the points reflect only the instrumental noise level. The variance between the points, however, contains information about sky brightness fluctuations. If present, these fluctuations make the variance between the points larger than expected from the error bars. The difference between the measured variance and the instrumental noise variance is termed the *excess* variance. In reporting earlier observations of CBR anisotropies, Boynton and Partridge⁵⁶ presented a statistical test constructed by consideration of the Neyman-Pearson lemma determine an upper bound to the size of the excess variance. This analysis tests the hypothesis that the variance of sky brightness fluctuations is zero, $\sigma_{\text{sky}}^2 = 0$, against the continuum of hypotheses that the sky variance has some finite positive value, $\sigma_{\text{sky}}^2 = \hat{\sigma}^2 > 0$.

If the true variance of the sampled sky brightness fluctuations were $\hat{\sigma}^2$, then the terms $y_{\bullet r}^2/(s_r^2 + \hat{\sigma}^2)$, would be normally distributed with zero mean and unit variance, and the sum, $S = \sum_r y_{\bullet r}^2/s_r^2(s_r^2 + \hat{\sigma}^2)$, would be distributed as χ^2 , except for the weighting factor in the denominator, \hat{s}_r . With the definition $\mathcal{R} \equiv \sum_r s_r^{-2}/\sum_r s_r^{-4}$, the product $\mathcal{R}S$ is distributed approximately as χ^2 on $\nu_{\text{eff}} = \mathcal{R} \sum_r s_r^{-2}$ degrees of freedom.

To perform the test at a given confidence level, α , the root of

$$\mathcal{R}S(\hat{\sigma}) - \chi^2(\alpha, \nu_{\text{eff}}) = 0 \quad 5.5$$

is found. For the data of figure 5.8, the result of this test, summarized in table 5.1, is $\hat{\sigma} \leq 1.2 \times 10^{14}$ at the 95% confidence level. This limit, the major scientific result of this experiment, can be compared directly with theoretical predictions of $\text{var}(\Delta T^{(s)}/T_{\text{CBR}})$, as is done in the next chapter.

Table 5.1. Results of Hypothesis Test

ν_{eff}	\mathcal{R}	\mathcal{S}	$\hat{\sigma}$
9.7	9.4×10^{-9}	4.0×10^8	1.2×10^{-4}

Chapter 6. Interpretation and Summary

Interpretation

In the standard cosmological scenario, density and temperature perturbations present in the universe at decoupling should be detectable as CBR anisotropies. Predictions of the properties of these anisotropies have been made in the context of a variety of cosmological models.^{57,58,59,60,61,62} These calculations follow the dynamical evolution of primordial density perturbations through decoupling to the present and use the observed large scale galaxy correlation function to normalize the perturbation amplitudes. Implicit in this normalization is the assumption that galaxies are unbiased tracers of the overall matter distribution. In addition to the spatial spectrum and the type of primordial perturbations, predictions of CBR anisotropies are sensitive to overall properties of the universe: its age, expressed through the Hubble parameter $H_0 = 100h \text{ km s}^{-1} \text{ Mpc}^{-1}$, its spatial curvature, expressed through the ratio of the present density to the closure density, Ω , the existence of a nonzero cosmological constant, Λ , and the presence and nature of any nonbaryonic matter in the universe.

The result of the preceding data analysis is a 95% confidence upper limit to the amplitude of intensity fluctuations in the CBR, $\hat{\sigma} < 1.2 \times 10^{-4}$. Comparing this limit with the anisotropy amplitude predicted in various models constrains the acceptable range of values of the model parameters. In principle, the expected variance in the CBR temperature, which is directly comparable to the observed limit, can be calculated from the CBR correlation function and the autocovariance of the

sampling pattern. In practice, however, only two papers^{61,62} provide sufficient information for this direct calculation of the expected variance. For the other models, the predictions were estimated from the graphical presentations of the theoretical results. These predictions are summarized in table 6.1.

CBR anisotropies in a universe dominated by baryons are considered in the first two models in this table (WS⁵⁸ and W⁵⁹). For adiabatic perturbations, the results of this experiment effectively rule out low density models. Interpolating between the high and low density models gives a lower bound of $\Omega = 0.5$ for a scale invariant ($n = 1$) primordial perturbation spectrum. Less stringent limits are placed on models with steeper, non scale invariant adiabatic spectra or isothermal perturbations, but there are no compelling mechanisms for generating such fluctuations. Moreover, introducing a cosmological constant to satisfy the prediction by inflation theories that the universe is flat, $\Omega + \Lambda = 1$, does not markedly change the anisotropy predictions in the low density models.⁶³

Analysis of the abundances of the light elements generated during primordial nucleosynthesis⁶⁴ indicates, however, baryons cannot close the universe, i.e., that $\Omega_b < 0.2$ and probably $\Omega_b < 0.15$. The incompatibility of this constraint with the anisotropy limits raises the possibility the dominant form of matter in the universe is nonbaryonic. Of all the various forms of weakly interacting material that have been proposed, cold dark matter is perhaps the most promising. This material has been nonrelativistic since the very early stages of the universe, shortly after the inflationary epoch, and so have been free to gravitationally condense since then.

The second group of models in table 6.2 (VS⁶⁰ and BE⁶¹) consider scale invariant perturbations in a universe dominated by cold dark matter. In these cases, the amplitude of the fluctuations is smaller than in the baryon dominated model. The results of this experiment are only consistent with these models if $\Omega > 0.2$ and

Table 6.1. Model Predictions

Overall Density	Baryon Density	Hubble Parameter	Nonbaryonic Species	Perturbation Spectral Index	Perturbation Type	Predicted Anisotropy $\times 10^5$	Reference
Ω	Ω_b	h		n		$\left[\text{var} \left(\frac{\Delta T^{(*)}}{T_{\text{CBR}}} \right) \right]^{1/2}$	
1.0	1.0	0.52	none	4	adiabatic	1.5	WS
1.0	1.0	0.52	none	3	adiabatic	4.8	WS
1.0	1.0	0.52	none	2	adiabatic	6.3	WS
1.0	1.0	0.52	none	1	adiabatic		WS
1.0	1.0	0.52	none	0	adiabatic		WS
1.0	1.0	0.52	none	-1	adiabatic	3.4	WS
1.0	1.0	0.52	none	1	isothermal	0.28	WS
1.0	1.0	0.52	none	0	isothermal	1.6	WS
1.0	1.0	0.52	none	-1	isothermal	2.6	WS
0.1	0.1	0.5	none	4	adiabatic	17	W
0.1	0.1	0.5	none	3	adiabatic	30	W
0.1	0.1	0.5	none	2	adiabatic	61	W
0.1	0.1	0.5	none	1	adiabatic	86	W
0.1	0.1	0.5	none	0	adiabatic	89	W
0.1	0.1	0.5	none	-1	adiabatic	74	W
0.1	0.1	0.5	none	1	isothermal	0.13	W
0.1	0.1	0.5	none	0	isothermal	1.4	W
0.1	0.1	0.5	none	-1	isothermal	4.9	W
1.0	0.03	1.0	cold	1	adiabatic	0.73	VS
1.0	0.03	0.5	cold	1	adiabatic	1.4	VS
0.4	0.03	1.0	cold	1	adiabatic	2.1	VS
0.4	0.03	0.75	cold	1	adiabatic	3.2	VS
0.4	0.03	0.5	cold	1	adiabatic	5.7	VS
0.2	0.03	0.75	cold	1	adiabatic	9.2	VS
0.2	0.03	0.5	cold	1	adiabatic	18.1	VS
1.0	0.03	0.75	cold	1	adiabatic	0.49	BE
1.0	0.03	0.5	cold	1	adiabatic	1.1	BE
0.4	0.03	0.75	cold	1	adiabatic	1.7	BE
0.3	0.03	0.75	cold	1	adiabatic	2.6	BE
0.2	0.03	1.0	cold	1	adiabatic	3.3	BE
0.2	0.03	0.75	cold	1	adiabatic	5.1	BE
0.2	0.03	0.5	cold	1	adiabatic	10.4	BE
0.2	0.1	0.75	cold	1	adiabatic	13.7	BE
1.0	0.03	0.75	neutrinos	1	adiabatic	2.5	BE
1.0	0.03	1.0	cold	1	isocurvature	0.65	EB
0.2	0.03	1.0	cold	1	isocurvature	6.5	EB

$h > 0.75$. Globular cluster ages (> 13 billion years) indicate $h < 0.5$, implying a still higher limit, $\Omega > 0.3$. On the other hand, numerical simulations of galaxy clustering are unable to achieve agreement with observations if $\Omega > 0.2$.⁶⁵ Taken together, these results indicate galaxies may not be good tracers of the overall mass distribution.

Summary

The three major activities involved in this work were construction of an operational experimental apparatus, development of an observing technique for reducing atmospheric noise, and observation, of the CBR that set an upper limit on fine scale anisotropies.

The instrumentation is centered on a 9 m diameter Cassegrain radio telescope situated on a desert mountaintop in eastern Washington. The telescope's original secondary mirror was replaced with a low mass, carbon fiber composite mirror that is nutated to modulate the telescope's pointing direction. The nutation mechanism is capable of steering the beam up to $\pm 15'$ from the optic axis, and its bandwidth is close to 50 Hz. For switching the telescope beam $10'$, the transition time is about 10 ms. The control computer is capable of blind pointing the telescope with a radial error of less than $0.5'$.

The telescope is operated as a multimode system using a high throughput, far infrared photometer based on a ^3He cooled semiconductor bolometer. Centered at $\lambda = 2.2$ mm, the spectral bandwidth is $\Delta\lambda = 0.25$ mm, and in conjunction with this photometer, the telescope beam width is $4'$ FWHM. The overall noise level is $\delta T_N/T_{\text{CBR}} \sim 9 \times 10^{-4} \sqrt{s}$, competitive with all other technologies for these

measurements. The experiment is controlled by an automated data acquisition system, which provides system scheduling and elementary data analysis functions.

Central to the observing technique is the secondary mirror nutation system. This system allows high frequency (10 Hz), double differencing to be incorporated in the modulation process. With this sampling strategy detector limited performance is possible, even under unfavorable weather conditions. The effectiveness of this technique was demonstrated by its rendering atmospheric noise negligible during the observations, despite nonideal weather conditions.

Observations of the CBR at an effective angular scale of 8' revealed no anisotropy larger than 1.2×10^{-4} at the 95% confidence level. This limit excludes a low density, ($\Omega < 0.5$), baryon dominated universe, and constrains models of a cold dark matter dominated universe to $\Omega > 0.2$.

References

1. Penzias, A. A., and Wilson, R. W., 1965, "A Measurement of Excess Antenna Temperature at 4080 Mc/s," *Ap. J.*, **142**, 419.
2. This phrase, "big bang", is attributed to F. Hoyle, one of the architects of the steady state theory of the universe.
3. Dicke, R. H., Peebles, P. J. E., Roll, P. G., and Wilkinson, D. T., 1965, "Cosmic Black-Body Radiation," *Ap. J.*, **142**, 414.
4. Weiss, R., 1980, "Measurements of the Cosmic Background Radiation," *Ann. Rev. Astron. Astrophys.*, **18**, 489.
5. Smoot, G. F., De Amici, G., Friedman, S. D., Witebsky, C., Sironi, G., Bonelli, G., Mandolesi, N., Cortiglioni, S., Morigi, G., Partridge, R. B., Danese, L., and De Zotti, G., 1985, "Low-Frequency Measurements of the Cosmic Background Radiation Spectrum," *Ap. J. (Letters)*, **291**, L23.
6. De Amici, G., Smoot, G., Friedman, S. D., and Witebsky, C., 1985, "New 33 GHz measurements of the Cosmic Background Radiation Intensity," *Ap. J.*, **298**, 710.
7. Lubin, P., Villela, T., Epstein, G., and Smoot, G., 1985, "A Map of the Cosmic Background Radiation at 3 Millimeters," *Ap. J. (Letters)*, **298**, L1.
8. de Lapparent, V., Geller, M. J., and Huchra, J. P., 1986, "A Slice of the Universe," *Ap. J. (Letters)*, **302**, L1.
9. Guth, A. H., 1986, "The New Inflationary Universe, 1984," in *Inner Space/Outer Space*, ed. by E. W. Kolb, M. S. Turner, D. Lindley, K. Olive, and D. Seckel, (University of Chicago Press).

10. Bardeen, J. M., Steinhardt, P. J., and Turner, M. S., 1983, "Spontaneous Creation of Almost Scale-Free Density Perturbations in an Inflationary Universe," *Phys. Rev. D*, **78**, 679.
11. Hawking, S. W., and Moss, I. G., 1983, "Fluctuations in the Inflationary Universe," *Nucl. Phys.*, **B224**, 180.
12. Zel'dovich, Ya. B., 1972, *Mon. Not. Roy. astr. Soc.*, **160**, 1P.
13. Bond, J. R., and Efstathiou, G. 1984, "Cosmic Background Radiation Anisotropies in Universes Dominated by Non-Baryonic Dark Matter," *Ap. J. (Letters)*, **285**, L45.
14. Vittorio, N., and Silk, J., 1984, "Fine-Scale Anisotropy of the Cosmic Microwave Background in a Universe Dominated by Cold Dark Matter," *Ap. J. (Letters)*, **285**, L39.
15. Abbott, L. F., 1986, "Inflation and the Isotropy of the Microwave Background," in *Inner Space/Outer Space*, ed. by E. W. Kolb, M. S. Turner, D. Lindley, K. Olive, and D. Seckel, (University of Chicago Press).
16. Uson, J. M., and Wilkinson, D. T., 1984, "Improved Limits on Small-Scale Anisotropy in Cosmic Microwave Background," *Nature*, **312**, 427.
17. Wilson, M., 1983, "On the Anisotropy of the Cosmological Background Matter and Radiation Distribution. II. The Radiation Anisotropy in Models with Negative Spatial Curvature," *Ap. J.*, **273**, 2.
18. Yang, J., Turner, M. S., Steigman, G., Schramm, D. N., and Olive, K. A., 1984, "Primordial Nucleosynthesis: A Critical Comparison of Theory and Observation," *Ap. J.*, **281**, 493.

19. Davis, M., Efstathiou, G., Frenk, C. S., and White, S. D. M., 1985, "The Evolution of Large Scale Structure in a Universe Dominated by Cold Dark Matter," *Ap. J.*, **292**, 371.
20. Schaeffer, R., and Silk, J., 1985, "Biased Galaxy Formation in a Universe Dominated by Cold Dark Matter," *Ap. J.*, **292**, 319.
21. Weiss, R., 1980, "Measurements of the Cosmic Background Radiation," *Ann. Rev. Astron. Astrophys.*, **18**, 489.
22. Danese, L., De Zotti, G., and Mandolesi, N., 1983, "Radio Source Contributions to Small-scale Anisotropies of the Microwave Background," *Astron. and Astrophys.*, **121**, 114.
23. Pajot, M., 1985, private communication.
24. Reynolds, R., Roesler, F., and Scherb, F., 1974, "The Intensity Distribution of Diffuse Galactic $H\alpha$ Emission," *Ap. J. (Letters)*, **192**, L53.
25. Meyer, S. S., 1986, private communication.
26. Kraus, J. D., 1986, *Radio Astronomy*, 2nd ed., (Cygnus-Quasar: Powell, Ohio).
27. Bond, J. R., and Efstathiou, G. 1984, "Cosmic Background Radiation Anisotropies in Universes Dominated by Non-Baryonic Dark Matter," *Ap. J. (Letters)*, **285**, L45.
28. Vittorio, N., and Silk, J., 1984, "Fine-Scale Anisotropy of the Cosmic Microwave Background in a Universe Dominated by Cold Dark Matter," *Ap. J. (Letters)*, **285**, L39.
29. Uson, J. M., and Wilkinson, D. T., 1984, "Improved Limits on Small-Scale Anisotropy in Cosmic Microwave Background," *Nature*, **312**, 427.
30. Tucker, J. R., and Feldman, M. J., 1985, "Quantum Detection at Millimeter Wavelengths," *Rev. Mod. Phys.*, **57**, 1055.

31. Helstrom, C. W., 1968, *Statistical Theory of Signal Detection*, 2nd ed., (Pergamon: Oxford).
32. Sunyaev, R. A., and Zel'dovich, Ya. B., 1970, "Small-Scale Fluctuations of Relic [sic] Radiation," *Astrophys. Space Sci.*, **7**, 3.
33. Jones, B. J. T., and Wyse, R. F. G., 1985, "The Ionisation of the Primeval Plasma at the Time of Recombination," *Astron. Astrophys.*, **149**, 144.
34. Boynton, P. E., and Partridge, R. B., 1973, "Fine-Scale Anisotropy of the Microwave Background: An Upper limit at $\lambda = 3.5$ Millimeters," *Ap. J.*, **181**, 243.
35. Lindgren, B. W., 1962, *Statistical Theory*, (Macmillan: New York).
36. Deeter, J. E., and Boynton, P. E., 1982, "Techniques for the Estimation of Red Power Spectra. I. Context and Methodology," *Ap. J.*, **261**, 337.
37. Deeter, J. E., and Boynton, P. E., 1986, private communication.
38. Stone, W. A., Thorp, J. M., Gifford, O. P., and Hoitink, D. J., 1983, "Climatological Summary for the Hanford Area," PNL-4622, Pacific Northwest Laboratory, Richland, WA.
39. Turner, T. S., Optical Sciences Center, University of Arizona.
40. Ruze, J. 1965. "Lateral-Feed Displacement in a Paraboloid," *IEEE Trans. Ant. Prop.*, **TAP 13**, 660.
41. Ulich, B. L., 1976, "Pointing Characteristics of the 36-foot Telescope," Tucson Operations Internal Report No. 1, National Radio Astronomy Observatory, Tucson, AZ.
42. Harmer, R. L., and McDonald, E. W., 1966. "Alignment of the 30-foot Antenna Facility," NA65H-1120, North American Aviation. Columbus, Ohio.
43. Boynton, P. E., Stokes, R. A., and Deeter, J. E., 1974.

44. Born, M., and Wolf, E., 1980, *Principles of Optics*, 6th ed., (Pergamon: Oxford), §8.5.2
45. Ruze, J., 1966, "Antenna Tolerance Theory – A Review," *Proc. IEEE*, **54**, 633.
46. Golden, L., 1977, private communication.
47. Ulich, B. L., 1981, "Millimeter Wave Radio Telescopes: Gain and Pointing Characteristics," *Int. J. Infrared and Millimeter Waves*, **2**, 293.
48. Model TC2012, RCA Closed Circuit Video Equipment, Lancaster, PA.
49. Model 391A, Ithaco Inc., Ithaca NY.
48. Born, M., and Wolf, E., 1980, *Principles of Optics*, 6th ed., (Pergamon: Oxford), §8.8.
49. Emerson and Cumings, Inc., Woburn, Massachusetts.
50. Ulich, B. L., 1974, "Absolute Brightness Temperature Measurements at 2.1-mm Wavelength," *Icarus*, **21**, 254.
51. Clark, W. W., III, Miller, J. E., and Richardson, P. H., 1984, "Sky Brightness Measurements at 135 GHz and 215 GHz," *IEEE Trans. Antennas Propagat.*, **TAP 23**, 928.
52. Ulich, B. L., Cogdell, J. R., and Davis, J. H., 1973, "Planetary Brightness Temperatures at 8.6 mm and 3.1 mm Wavelengths," *Icarus*, **19**, 59.
53. Low, F. J., and Davidson, A. W., 1965. "Lunar Observations at a Wavelength of 1 mm," *Ap. J.*, **142**, 1278.
54. Reber, E. E., 1970, "Brightness Temperature of the Quiet Sun and New Moon at 3.3- and 5.7 mm," *Icarus*, **12**, 348.

55. Bond, J. R., and Efstathiou, G. 1984, "Cosmic Background Radiation Anisotropies in Universes Dominated by Non-Baryonic Dark Matter," *Ap. J. (Letters)*, **285**, L45.
55. Boynton, P. E., and Partridge, R. B., 1973, "Fine-Scale Anisotropy of the Microwave Background: An Upper limit at $\lambda = 3.5$ Millimeters," *Ap. J.*, **181**, 243.
57. Davis M., and Boynton P., 1980 "On the Present Observability of Density-Temperature Fluctuations in the Early Universe," *Ap. J.*, **237**, 265.
58. Wilson, M. L., and Silk, J., 1981, "On the Anisotropy of the Cosmological Background Matter and Radiation Distribution. I. The Radiation Anisotropy in a Spatially Flat Universe," *Ap. J.*, **243**, 14.
59. Wilson, M., 1983, "On the Anisotropy of the Cosmological Background Matter and Radiation Distribution. II. The Radiation Anisotropy in Models with Negative Spatial Curvature," *Ap. J.*, **273**, 2.
60. Vittorio, N., and Silk, J., 1984, "Fine-Scale Anisotropy of the Cosmic Microwave Background in a Universe Dominated by Cold Dark Matter," *Ap. J. (Letters)*, **285**, L39.
61. Bond, J. R., and Efstathiou, G. 1984, "Cosmic Background Radiation Anisotropies in Universes Dominated by Non-Baryonic Dark Matter," *Ap. J. (Letters)*, **285**, L45.
62. Efstathiou, G., and Bond, J. R.. 1986, "Isocurvature Cold Dark Matter Fluctuations," *Mon. Not. Roy. astr. Soc.*, **218**, 103.
63. Vittorio, N., and Silk, J., 1985, "Microwave Background Anisotropy and Decaying Particle Models for Flat Universe."

64. Yang, J., Turner, M. S., Steigman, G., Schramm, D. N., and Olive, K. A., 1984, "Primordial Nucleosynthesis: A Critical Comparison of Theory and Observation," *Ap. J.*, **281**, 493.
65. Davis, M., Efstathiou, G., Frenk, C. S., and White, S. D. M., 1985, "The Evolution of Large Scale Structure in a Universe Dominated by Cold Dark Matter," *Ap. J.*, **292**, 371.
67. Located at the Battelle Observatory near Richland, WA.
68. Ulich, B. L. 1976, "Pointing Characteristics of the 36-foot Telescope," NRAO Tucson Operations Internal Report No. 1.
69. Ruze, J. 1965, "Lateral-Feed Displacement in a Paraboloid," *IEEE Trans. Antennas Propagat.*, **TAP 13**, 660.
70. Turner, T. S., 1978, private communication, Optical Sciences Center, Tucson, Az.
71. Sedlecek, C., and Smith, D., 1980, private communication.
72. Varathane "Colors in Plastic," untinted, Flecto Manufacturing, San Jose, CA.
73. Model VTS-100, Vibration Test Systems, Aurora, Ohio
74. Free-Flex pivots, The Bendix Corporation, Fluid Power Division, Utica, N. Y.
75. Model HR-500, Schaevitz Engineering, Pennsauken, N. J.
76. Model 600, Crown International, Inc., Elkhart, Indiana.
77. Model 3582A, Hewlett Packard
78. D'Azzo, J. J., and Houpis, C. H. 1975, "Linear Control Theory and Design," (McGraw-Hill: New York)
79. Aikens, R. S. 1975, "A Cassegrain Mirror Control System for Infrared Chopping Applications," *AURA Engineering Technical Report No. 57*.

80. Ceccarelli, C., Dall'oglio, G., Ferri, G., Pietranera, L., Radford, S., and Xie, G. Z., 1984, *Infrared Phys.*, **24**, 493.
81. Nishioka, N. S., Richards, P. L. and Woody, D. P., 1978, *Appl. Opt.*, **17**, 1562.
82. NiCr film on a silicon substrate; Mini-Systems, Inc., North Attleboro, MA.
83. Moseley, S. H., 1984, private communication.
84. Winston, R., 1970, *J. Opt. Soc. Am.*, **60**, 245.
85. Harper, D. A., Hildebrand, R. H., Stiening, R., and Winston, R., 1976, *Appl. Opt.*, **15**, 53.
86. Davis, J.E., 1980, *Infrared Phys.*, **20**, 287; Cochise Instruments, Sierra Vista, AZ.
87. E. I. duPont de Nemours & Co., Inc., Wilmington, DE.
88. Halpern, M., Gush, H. P., Wishnow, E., and de Cosmo, V., 1986, *Appl. Opt.*, in press.
89. Corning Glass Works. Corning, NY.
90. Möller, K. D., and Rothschild, W. G., 1971, "Far Infrared Spectroscopy," Wiley-Interscience, New York.
91. Ade, P., 1984, private communication.
92. Mather, J. C., 1982, *Appl. Opt.*, **21**, 1125.
93. Hewlett Packard Model 3582A.

Appendix A. A High Performance Beam Switch

Abstract

Nutation of a Cassegrain telescope's secondary mirror is a convenient method of steering the telescope beam through a small angle. This principle was exploited to build a flexible, high performance beam switch for a millimeter wave telescope. A low mass, carbon fiber composite mirror is moved by linear electrodynamic motors operated in a frequency compensated control loop. To reduce the peak stresses on the mechanical linkages and to attain optimum performance a digitally generated, tailored input waveform is used. In an interval of about 10 ms, the system is capable of shifting the telescope beam by $10'$, which requires rotating the 75 cm diameter secondary mirror by 1.25° .

Introduction

Differential measurements are insensitive to a variety of systematic effects which may otherwise obscure the signal of interest. In astronomy a common technique is "beam switching," where the difference between the incident radiation from a source and from a nearby, sourceless region of the sky is measured. At millimeter and infrared wavelengths switching frequencies greater than 5 Hz are necessary to overcome the primary source of variable atmospheric attenuation and emission, rapid fluctuations of water vapor content.

Nutation of a Cassegrain telescope's secondary mirror is a convenient way of rapidly steering the telescope beam through a small angle. For studies at millimeter

wavelengths of fine scale anisotropies in the cosmic background radiation, a mechanism was developed to nutate the 75 cm diameter subreflector of a Cassegrain radio telescope with a 9 m diameter primary mirror.⁶⁷ The system's unity gain bandwidth is close to 50 Hz, its maximum switching amplitude is greater than 20', peak to peak, and its equilibrium position is adjustable within the amplitude range.

The following sections discuss the system's optical design, its mechanical and electronic components, the analysis of its dynamics, the design of its control system, its operation, and its performance.

Optical Design

Nutation of the a Cassegrain telescope's subreflector by an angle, $\Delta\phi$, shifts the electrical axis, or beam direction, of the telescope proportionally,⁶⁸

$$\Delta\theta = \left[R \left(\frac{BDf}{f} - \frac{BDF}{F} \right) - \frac{\ell}{f} (BDf + BDF) \right] \Delta\phi. \quad A.1$$

Here $\Delta\theta$ is the resulting beam shift, f and F are the primary and Cassegrain focal lengths, BDf and BDF are the corresponding beam deviation factors,⁶⁹ which account for the finite curvature of the telescope mirrors, and ℓ and R are the distances from the subreflector vertex to the primary focus and to the subreflector pivot axis, respectively. Because the pivot axis is behind the subreflector vertex, nutation displaces the subreflector laterally; this displacement leads to the first term in equation A.1. The second term arises from the change in the angular orientation of the primary and secondary mirrors. Figure A.1 illustrates the optical arrangement of our telescope and the optical parameters are listed in table A.1. To move

the main beam of our telescope by $10'$, the secondary mirror must be rotated by almost 1.25° .

As the main beam shift, $\Delta\theta$, increases coma becomes evident. Because our detector (Appendix B) is a nonimaging photometer, however, our requirements on image quality are not particularly stringent. Ray tracing studies⁷⁰ of our telescope indicate more than 95% of the power from a point source remains within the photometer aperture for main beam shifts up to $15'$ from the optic axis.

System Components

The beam switching system contains both mechanical and electronic parts. Figure A.2 shows the mechanical arrangement of the nutation mechanism. Driven by a pair of electrodynamic motors, the mirror nutates about its center of mass on flexural pivots. To minimize the vibration transmitted to the telescope structure, the motors counterrotate on similar pivots in a torque cancelling arrangement. Electronic components include an amplifier that powers the motors, a transducer for sensing the mirror position, and a control network that compensates the mechanism's dynamic response to allow closed loop operation. A protection circuit prevents the system from self-destructing under abnormal conditions and a digital function generator supplies a driving waveform tailored to the system's transfer function.

Mirror Assembly: The secondary mirror is a hyperboloid, 75 cm in diameter and 11 cm deep at the vertex. Two requirements of the nutation mechanism determined its mechanical design. First, to preserve the optical characteristics of the telescope the mirror must not deform under the dynamic loads imposed by high frequency.

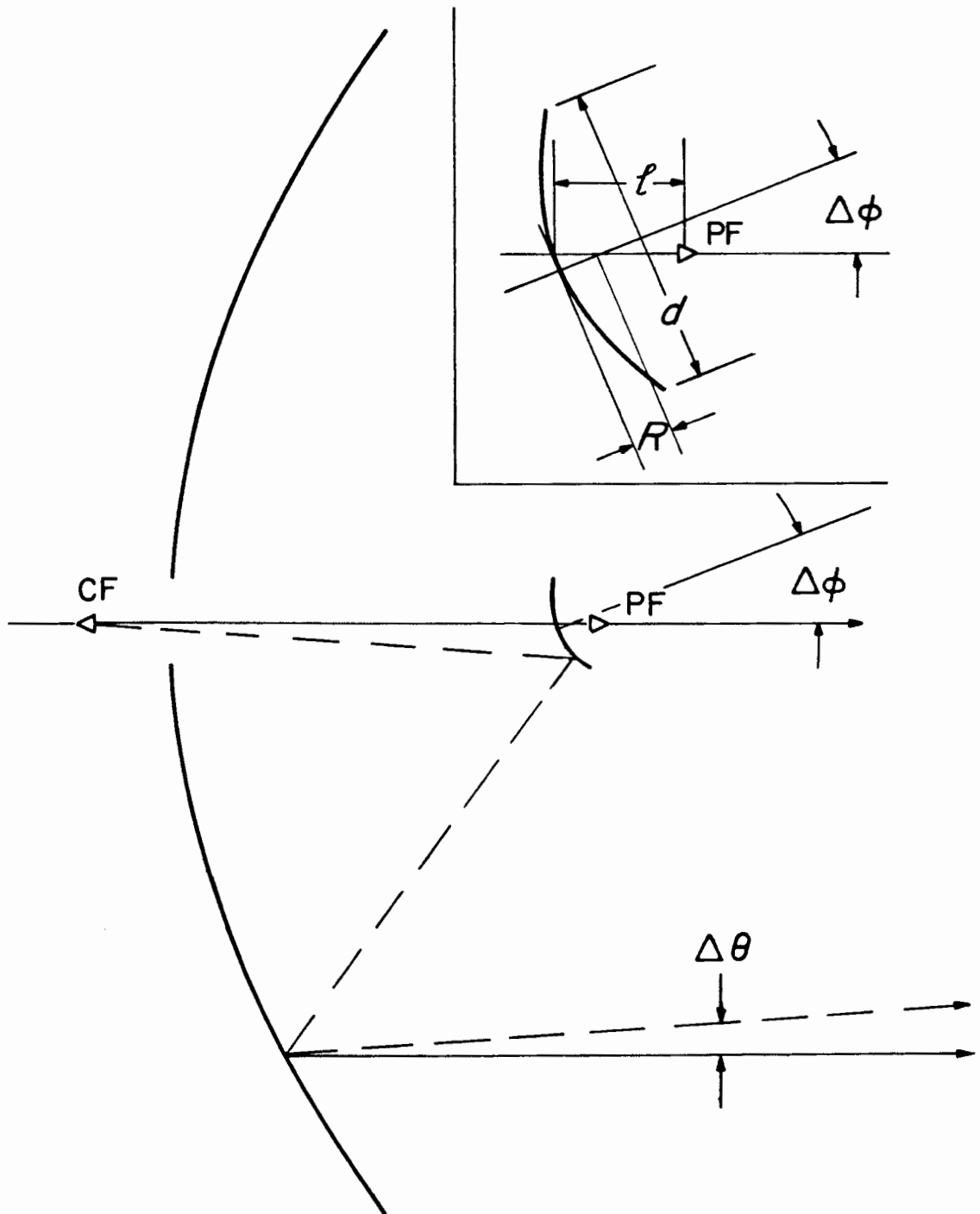


Figure A.1. Optical arrangement of the Battelle 9m telescope, illustrating beam switching by nutation of the secondary mirror.

Table A.1. Optical Parameters

primary diameter	D	9144.60 mm
primary focal length	f	3200.40 mm
primary focal ratio	f/D	0.35
primary beam deviation factor	$B\Delta f$	0.75
secondary diameter	d	750.00 mm
secondary focal length	F	39992.60 mm
secondary focal ratio	F/D	4.37
Cassegrain magnification	m	12.50
secondary beam deviation factor	$B\Delta F$	1.00
secondary vertex to primary focus	ℓ	282.57 mm
secondary vertex to pivot	R	90 mm
primary vertex to secondary focus	L	613.21 mm

large amplitude nutation. Second, the mirror assembly's moment of inertia must be small enough that the mirrors are capable of driving the nutation at the desired frequency.

Based on the force rating of the motors, which are the largest that would fit in the available space, the design goal was to make a mirror with a moment of inertia less than 0.3 kg m^2 . To achieve this, the mirror assembly was made of carbon fiber cloth impregnated with epoxy resin. This material has a stiffness to mass ratio similar to that of metals, but is more easily fabricated into low mass structures of complex shape.

The mirror assembly was designed and fabricated with the generous assistance of engineers at the Boeing Company.⁷¹ It consists of a hyperboloid membrane with

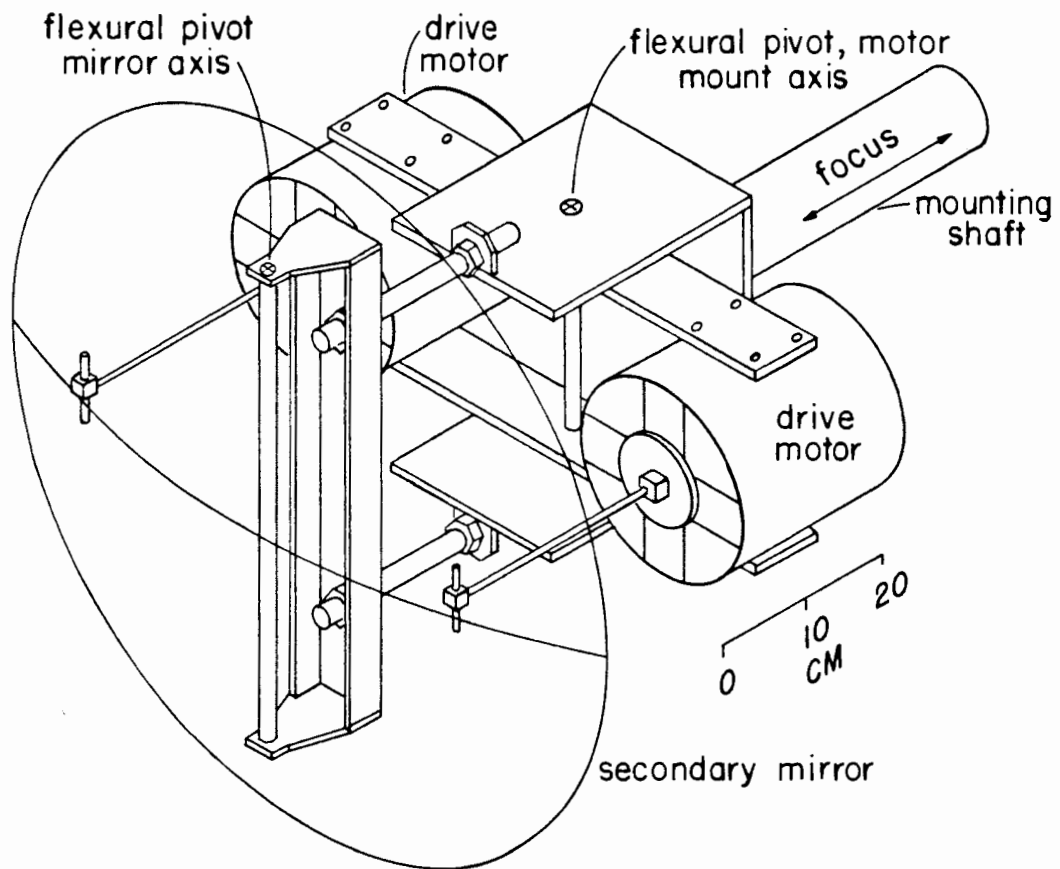


Figure A.2. Secondary mirror nutation mechanism, illustrating the mirror and motor mount flexural pivots, the electrodynamic drive motors and the focus travel carriage. The mirror backstructure and translation stage are omitted for clarity.

a stiffening structure bonded to its concave side. This backstructure incorporates mounts for the pivots and for linkages to the motors, as well as a steel and lead counterweight to balance the assembly about the pivot axis. Two mirrors were made: a fiber glass prototype and a final carbon fiber model.

The composite parts were molded from fabric impregnated with epoxy resin. To make the mirror mold, a steel template was cut to the radial profile of the hyperboloid on a numerically controlled milling machine and then an aluminum mold was machined on a lathe that followed this template. Precut fabric sheets were laid in the polished mold and the assembly was cured in an autoclave at 120 C. After curing, the material may be reheated to 65 C without distorting, making the mirror insensitive to environmental temperature extremes. Pieces of the backstructure were prepared the same way and then bonded to the back of the membrane with epoxy cement.

After the mirror was assembled, it was removed from the mold and the front surface was electroplated with copper to provide a reflecting surface. The copper layer is roughly 0.13 mm thick, much thicker than the skin depth at the experiment's operating wavelength of $\lambda = 2$ mm. Several treatments were tried to protect the copper surface from weathering and tarnishing, including rhodium overplating and wax coating. The most satisfactory was an application of a clear acrylic spray paint that has no far infrared absorption bands.⁷² In the laboratory, samples of copper clad fiberglass printed circuit board were tested both with and without the acrylic coating. These tests show that any difference in the samples' reflectivity at $\lambda = 2$ mm was less than 1%.

During the course of the project, water twice intruded between the copper plating and the carbon fiber membrane. Subsequent frost heaving distorted the reflecting surface and the water chemically attacked the resin surface of the mirror.

To repair this damage the copper coating and the affected portions of resin were removed, and then thin epoxy coating was applied by casting in the original mold. This restored the surface shape, and a new copper layer was deposited to replace the reflecting layer. After each resurfacing or replating operation, the mirror was checked against the template using a feeler gauge; in all cases, the measured rms deviations were less than 0.13 mm.

Driving motors: Two electrodynamic linear motors connected 180° out of phase in a "push-pull" arrangement drive the nutation mechanism. These motors operate similarly to loudspeakers, with a solenoidal armature suspended in the field of a permanent magnet, so current flowing through the solenoid induces an axial electromotive force. Each motor⁷³ develops 37.5 Nt A^{-1} , up to a maximum force output of 450 Nt, and has a mass of 22.5 kg. The motor armatures, connected to the mirror backstructure, are suspended from the motor bodies by nearly critically damped springs with a stiffness of 7060 Nt m^{-1} .

Mounting: The secondary mirror mounting (fig. A.2) is an integral part of the nutation mechanism. Flexural pivots, on either end of a steel axle in the mirror backstructure, allow mirror nutation by $\pm 3.5^\circ$. To minimize the vibration transmitted to the telescope structure, the motors are mounted on the ends of a bar that counterrotates about its center on a pair of similar pivots. As discussed below, if the mirror and motor pivot spring constants are chosen so their ratio is proportional to the ratio of the moments of inertia of the mirror and the mounted motors, then the torques on the supporting structure cancel. Two convenient models⁷⁴

have $0.3 \text{ Nt m rad}^{-1}$ and $2.5 \text{ Nt m rad}^{-1}$, for the mirror and motor pivots, respectively, which are in the desired ratio if the mirror's moment of inertia is 0.27 kg m^2 . All of these pivots are essentially idea springs with negligible damping.

The mounting incorporates several adjustments for aligning and positioning the secondary mirror. To allow focussing, the nutation mechanism is mounted on a carriage that can travel 160 mm along the telescope's optic axis. This focus travel was aligned parallel to the optic axis by adjusting the legs of the tripod supporting the prime focus cage. Additionally, the focus carriage can rotate about the optic axis $\pm 10^\circ$ from the nominal horizontal to permit leveling the nutation motion precisely. Electric motors in first order control loops drive both the focus and rotation motions. The angle between the mirror nutation axle and the focus travel also can be adjusted, and a translation stage mounted between the mirror and the motors permits moving the mirror up to 10 mm in any direction perpendicular to the optic axis.

Optical auto collimation was used to align the secondary mirror with the telescope's optic axis as follows. First, the telescope was pointed at the zenith and its position adjusted so the rim of the primary mirror was level, as determined by a theodolite placed at the primary vertex. Then the optic axis was taken as the zenith direction, and an optical plummet[†] was mounted at the primary vertex so the plummet's and the telescope's optic axes were coincident.

[†] An optical plummet is a surveying instrument that has two small, right angle telescopes with coaxial objectives pointing in opposite directions. It is commonly used to align tall buildings in a single bound.

The subreflector was translated so its vertex was within 0.6 mm of the plummet cross hairs. For angular alignment, a small glass mirror was mounted at the subreflector's vertex and normal to its rotation axis. The angle of the subreflector was adjusted so the return beam was closer than $30''$ to the plummet's optic axis.

Since changes in the telescope elevation shift both the subreflector position and angle, the final alignment was made at $\approx 45^\circ$ elevation, where CBR observations were planned.

Electronic Components: The subreflector's nutation angle, θ_1 , is sensed by a linear variable differential transformer (LVDT) position transducer.⁷⁵ This device works by measuring the change in the inductance between the coils of a solenoidal transformer caused by the motion of a magnetic core along the solenoid axis. A second order low pass filter in the demodulation circuit attenuates the 11 kHz excitation carrier by restricting the transducer bandwidth to about 1 kHz. In response to movement of the core, the transducer's output, V_o , is 0.5 V mm^{-1} . The LVDT body is mounted on the nutation mechanism's support structure and the LVDT core is attached to the mirror backstructure 18 cm from the nutation axis. Then, by the small angle approximation, $V_o/\theta_1 = 1.6 \text{ V deg}^{-1}$, where θ_1 is the mirror nutation angle.

A power amplifier⁷⁶ with an output current capacity of $\pm 20 \text{ A}$, a voltage compliance of $\pm 120 \text{ V}$, and a bandwidth of 45 kHz drives the motors. This amplifier is connected in a transconductance configuration, producing an output current proportional to the input voltage, $I_o/V_i = 5.3 \text{ A/V}$, so the force developed by the motors is $F/V_i = 200 \text{ Nt V}^{-1}$.

The functions of the three other electronic components, the control network, the protection circuit, and the digital function generator, are described in subsequent sections. They were all designed especially for the beam switch system and built from integrated semiconductor circuits using standard electronic construction practices.

Table A.2. Nutation Mechanism Dynamical Parameters

Mirror moment of inertia	I	0.47 kg m ²
Motor mass	M	22.5 kg
Motor mount lever arm	r	0.22 m
Reduced moment of inertia	I'	0.39 kg m ²
Mirror pivot strength	k_1	0.3 Nt m rad ⁻¹
Motor pivot strength	k_2	2.5 Nt m rad ⁻¹
Motor suspension strength	k_3	7060 Nt m ⁻¹
Motor suspension damping	b	54 Nt s m ⁻¹
Damping Ratio	ζ	0.16
Symmetric eigenfrequency	ω_s	1.1 rad s ⁻¹
Antisymmetric eigenfrequency	ω_a	42 rad s ⁻¹

Dynamical Analysis

A dynamical model of the secondary mirror nutation mechanism is shown in figure A.3 and the system's dynamical parameters are listed in the table A.2. In the following analysis I is the mirror's moment of inertia, M is the mass of each motor and F is the force it develops, $2r$ is the length of the mirror mounting bar, θ_1 and θ_2 are the angular displacements of the mirror and motor mount and k_1 and k_2 are the strengths of their respective pivot springs, and k_3 and b are the stiffness and damping of the motor suspensions.

The equations of motion for the angular displacements of the mirror, θ_1 , and the motor mount, θ_2 are

$$I\ddot{\theta}_1 + 2k_1\theta_1 + 2k_3r^2(\theta_1 - \theta_2) + 2br^2(\dot{\theta}_1 - \dot{\theta}_2) = 2rF \quad \text{A.2}$$

and

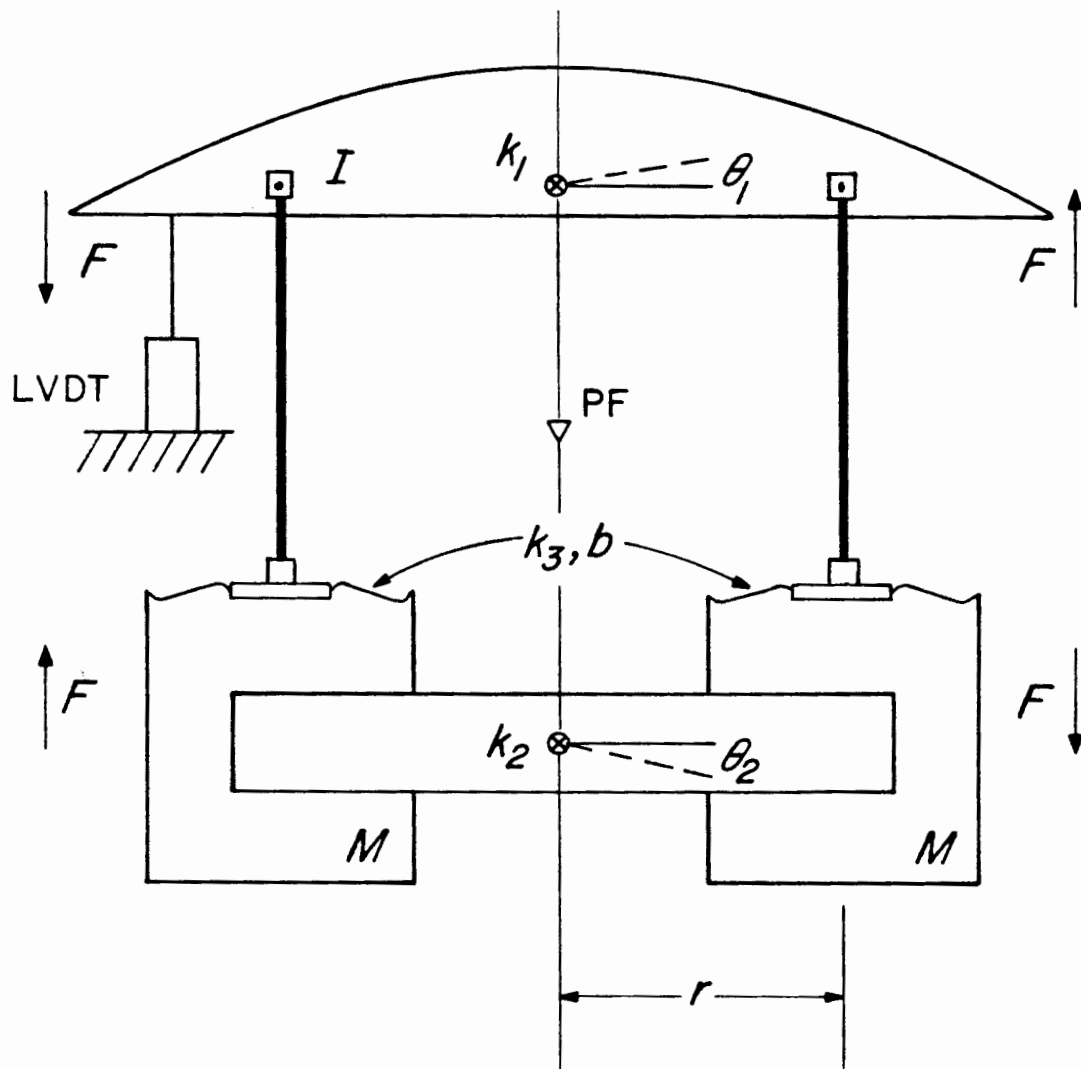


Figure A.3. Dynamical model of nutation mechanism.

$$2Mr^2\ddot{\theta}_2 + 2k_2\theta_2 + 2k_3r^2(\theta_2 - \theta_1) + 2br^2(\dot{\theta}_2 - \dot{\theta}_1) = -2rF, \quad \text{A.3}$$

where the dots indicate time derivatives. By defining differential and common mode amplitudes, $\xi = \theta_1 - \theta_2$ and $\Theta = (I\theta_1 + 2Mr^2\theta_2)/(I + 2Mr^2)$, respectively, these equations can be separated to describe the symmetric and antisymmetric modes of the system:

$$\ddot{\Theta} + \omega_s^2\Theta + \frac{2Mr^2}{I + 2Mr^2} \left(\frac{2k_1}{I} - \frac{2k_2}{2Mr^2} \right) \theta_2 = 0 \quad \text{A.4}$$

and

$$\ddot{\xi} + \omega_s^2\xi + \omega_a^2\xi + 2\omega_a\zeta\dot{\xi} + \left(\frac{2k_1}{I} - \frac{2k_2}{2Mr^2} \right) \theta_2 = \frac{2rF}{I'}. \quad \text{A.5}$$

Here $I' = 2Mr^2I/(I + 2Mr^2)$ is the system's reduced moment of inertia, $\omega_s = \sqrt{2k_1/I}$ is the oscillation frequency of the mirror on its pivots, $\omega_a = \sqrt{2k_3r^2/I'}$ is the oscillation frequency of the reduced system on the motor suspensions, and $\zeta = \sqrt{b^2r^2/2k_3I'}$, is the damping ratio of the reduced oscillator.

If the relative pivot strengths are chosen properly, $k_1/k_2 = I/2Mr^2$, the torques at the the pivots cancel and the equations are uncoupled. Then the motors will not be able to excite the rigid body. symmetric mode, $\theta_1 = \theta_2$, and there will be no net torque on the structure supporting the pivots. This arrangement minimizes the vibration transmitted to the secondary mirror support structure by the oscillating mechanism. Under these conditions, the eigenfrequencies of the symmetric mode are $s = \pm i\omega_s$, and the antisymmetric mode eigenfrequencies are $s = \omega_a \left(-\zeta \pm i\sqrt{1 + \omega_s^2/\omega_a^2 - \zeta^2} \right)$, where s is the complex frequency coordinate.

The mirror and motor mount pivot axes are separated by about 40 cm, and the supporting structure connecting them is cantilevered from the motor mount end. If the pivot springs are too strong, the torque at the mirror pivot will cause this

support to flex, and the driving motors may excite parallel mechanical resonances in the structure. Also, since it is impractical to make the pivot strength ratio exactly equal to the moment of inertia ratio, torque cancellation will not be perfect. On the other hand, the pivot springs provide the restoring torque necessary to keep the nutation mechanism centered. If they are too weak, the amplitude of symmetric mode oscillations excited by time varying external loads on the mechanism – wind, primarily – will be excessively large, and may exceed the mechanism's amplitude limits. The pivot strengths used, which give $\omega_s \approx 0.2$ Hz, represent a compromise between these two factors.

By setting $k_1/k_2 = I/2Mr^2$ and taking the Laplace transforms of equations A.2 and A.3,

$$\left[s^2 + \omega_s^2 + \frac{I'}{I} (\omega_a^2 + 2\omega_a \zeta s) \right] \theta_1 - \frac{I'}{I} (\omega_a^2 + 2\omega_a \zeta s) \theta_2 = \frac{2rF}{I} \quad \text{A.6}$$

and

$$\left[s^2 + \omega_s^2 + \frac{I'}{2Mr^2} (\omega_a^2 + 2\omega_a \zeta s) \right] \theta_2 - \frac{I'}{2Mr^2} (\omega_a^2 + 2\omega_a \zeta s) \theta_1 = -\frac{2rF}{2Mr^2}, \quad \text{A.7}$$

the dynamical equations can be solved algebraically for the mechanism's frequency response,

$$\frac{\theta_1}{F} = \frac{2r/I}{\omega_s^2 + \omega_a^2 + 2\zeta\omega_a s + s^2} \quad \text{A.8}$$

and

$$\frac{\theta_2}{F} = \frac{2r/2Mr^2}{\omega_s^2 + \omega_a^2 + 2\zeta\omega_a s + s^2}. \quad \text{A.9}$$

When the effect of the transducer, power amplifier and motors are included, the system transfer function is obtained from A.8,

$$\frac{V_t}{V_i} = \frac{K}{\omega_s^2 + \omega_a^2 + 2\zeta\omega_a s + s^2}. \quad \text{A.10}$$

To empirically verify this transfer function, a band limited, pseudorandom signal was applied to the amplifier input and the transducer signal was measured by a low frequency spectrum analyzer.⁷⁷ The result (fig. A.4) clearly shows the resonant behavior arising from a pair of complex poles at the antisymmetric mode eigenfrequencies, $s = \omega_a(-\zeta \pm \sqrt{\zeta^2 - 1 - \omega_s^2/\omega_a^2})$. Since $\omega_s^2 \ll \omega_a^2$, the resonant frequency, $\omega_a/2\pi \simeq 6.7$ Hz, and damping constant (ratio) $\zeta \simeq 0.16$, can be determined from this measurement.

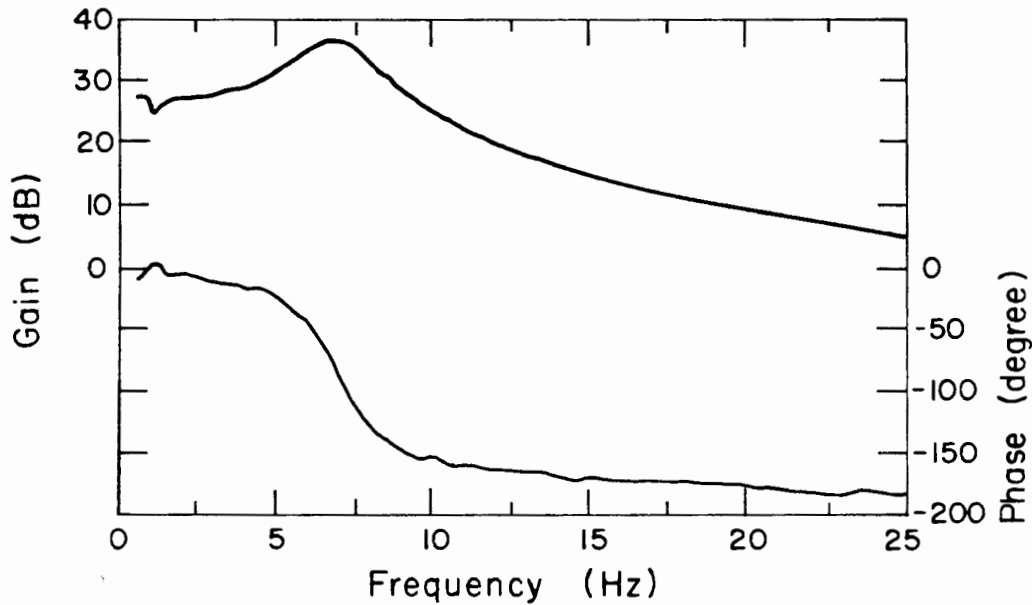


Figure A.4. Measured open loop frequency response of secondary mirror nutation mechanism. Upper trace is gain, lower trace is phase shift.

Control System Design

There are two basic ways to operate the nutation mechanism. In open loop operation, a signal is applied directly to the input of the power amplifier and dynamics of the mechanism determine the resulting motion of the mirror. This was the method used to determine the mechanism's frequency response (fig. A.4). As a way of modulating the telescope beam for differential measurements, however, open loop operation is unsatisfactory for a number of reasons. First, wind gusts will drive the symmetric mode of the mechanism, which will then oscillate about its equilibrium position, $\Theta = 0$, with a period, $1/\omega_s$, that is, by design, quite long. Second, a directly driven harmonic oscillator is generally restricted to sinusoidal motion, especially at frequencies above its resonance. Square wave modulation is more efficient than sine wave modulation, however, offering a $\sqrt{2}$ increase in the signal to noise ratio of a synchronously demodulated detector. Finally, a more complex modulation pattern may be used to discriminate against atmospheric noise better than simple sinusoidal or square wave motion.

In closed loop operation, on the other hand, the position of the mirror is subtracted from the input signal and the difference, called the error signal, is applied to the amplifier input. The result of this negative feedback is mirror motion that reduces the error signal. When properly implemented, a closed loop system can overcome the limitations of an open loop system. By offsetting the motors from their equilibrium position, external loads will be automatically balanced to maintain a stable mirror position and, within the system's bandwidth, the mirror will follow an arbitrary input waveform. The control network that generates the error signal must be carefully tailored, however, so frequency dependent phase shifts in the mechanisms's dynamics do not upset the stability of the system.

The objective of the control system is linear position control in the widest possible bandwidth consistent with good stability. Within the context of control system theory,⁷⁸ the optimum solution to this problem is to electronically compensate the nutation mechanism so it emulates the frequency response of a perfect integrator, $1/s$. With increasing frequency an integrator's gain falls at 6 dB per octave, and at all frequencies its phase shift is a constant lag of 90° . Examination of the mechanism's transfer function (fig. A.4) reveals, however, a destabilizing phase reversal at frequencies above the dominant resonance. Below the resonance the gain is constant, and above the resonance it falls at 12 dB per octave.

A block diagram of a control network that effects the desired emulation is shown in figure A.5, and the control elements' transfer functions are displayed in figure A.6. while table A.3 lists the values of system parameters. Two major control elements are required, an integrator before the amplifier input and a lead compensator in the feedback loop.⁷⁹ The integrator, with a zero just below the resonant pole, boosts the low frequency gain. The lead compensator provides both direct and derivative feedback to the summing junction at the integrator input. The relative amount of (and cross over frequency between) direct and derivative feedback is adjustable through the damping control.

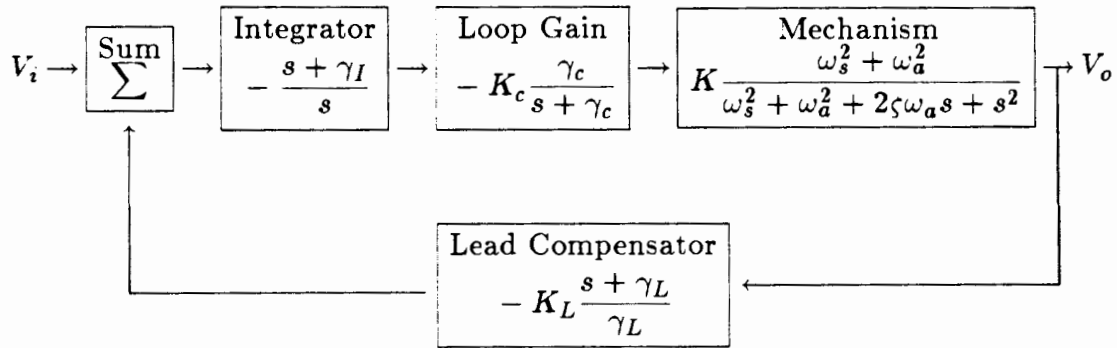


Figure A.5. Block diagram of nutation mechanism control system, showing the transfer function of each element.

Classical control theory states that for stable operation, the phase shift must be less than 180° at the unity gain frequency. The derivative feedback has a leading phase shift of 90° that stabilizes the oscillator above resonance.

The final control element is a loop gain amplifier between the integrator and the amplifier input. This element governs the ratio of open to closed loop gains, determining the system's maximum slew rate. To attenuate the LVDT carrier frequency, the transducer amplifier incorporates a second order filter with a cutoff frequency of 1 kHz. The gains of both the lead compensator and the loop gain amplifier also are rolled off at this frequency to prevent high frequency noise from dissipating excessive amplifier power and unnecessarily heating the drive motor coils.

Operation

Since a powerful, high performance system like this is vulnerable to self destruction, especially during testing of the feedback control system, a protection circuit is essential to successful operation. This circuit monitors the mirror position, the

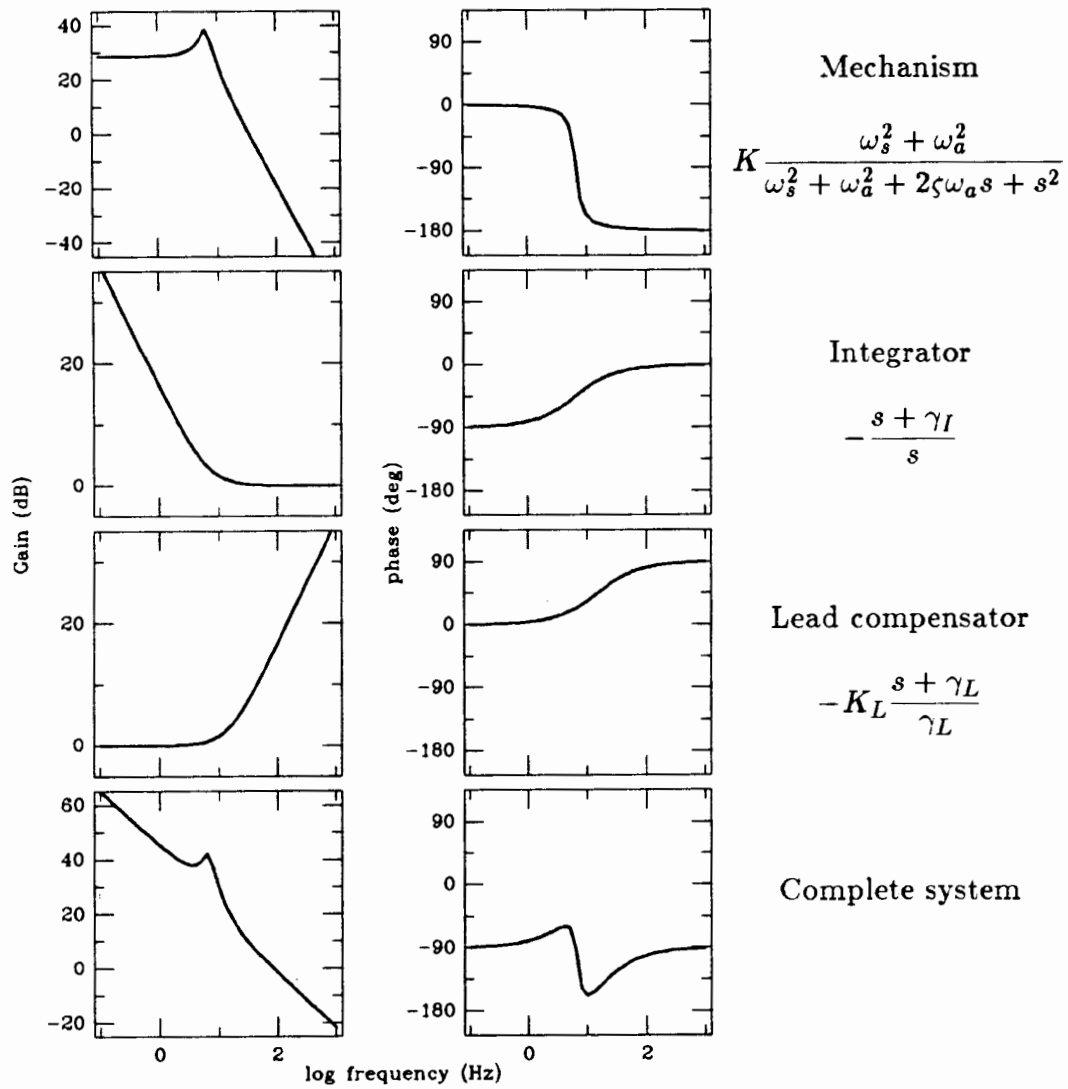


Figure A.6. Transfer functions of nutation mechanism control system elements.

Table A.3. Control System Parameters

Mechanism resonance	$\omega_a/2\pi$	6.7 Hz
Mechanism damping ratio	ζ	0.16
DC gain of mechanism	K	28.6 dB
Integrator zero	$\gamma_i/2\pi$	6.5 Hz
loop gain	K_c	up to 10 dB
Lead compensator gain	K_L	up to 40 dB
Lead compensator zero	$\gamma_L/2\pi$	6 to 35 Hz
Rise time, 10% to 90%	t_r	8 ms

relative motion of the motor armatures and bodies, the motor current, and the continuity of the linkages between the mirror and the motor armatures. If an error condition is detected, the circuit grounds both the input and output of the power amplifier and turns off the amplifier power supplies within 100 μ s. Since its installation, the circuit has protected the beam switch components from untimely damage.

The performance of the system is indicated in figures A.7 and A.8. A bandwidth close to 50 Hz is displayed by the closed loop frequency response (fig. A.7), and when driven by a square wave input the rise time is about 8 ms (fig. A.8).

Although this square wave response is adequate, it has two drawbacks. First, the rise time and amount of overshoot are inversely related. Second, and more serious, the initial response to the step input is a large discontinuous change in acceleration, or jerk. This jerk, much like a hammer blow, led repeatedly to the fatigue and failure of the linkages between the motors and the mirror. Although the protection circuit shut down the system to prevent further damage, failure times as short as 15 minutes were observed, an unsatisfactory situation.

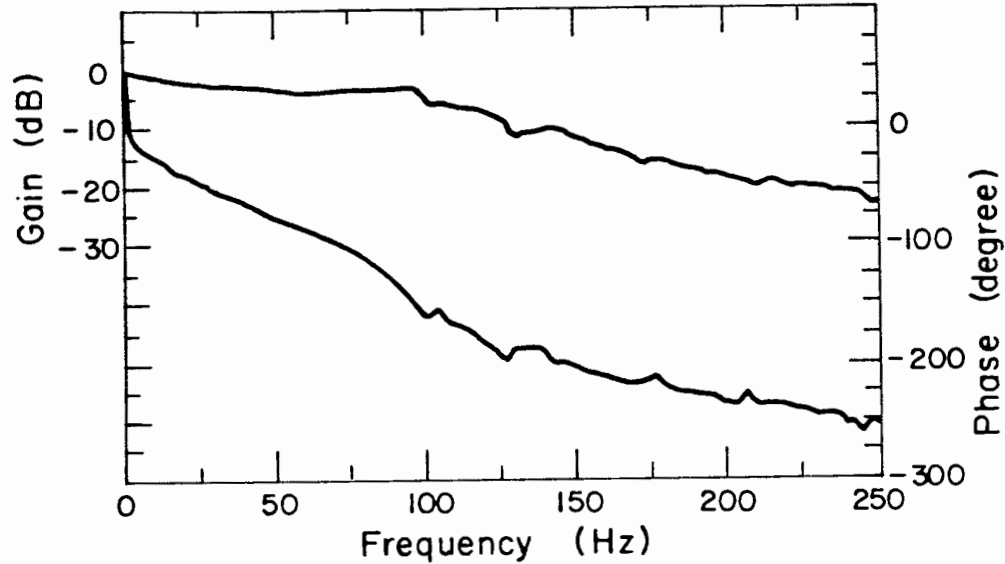


Figure A.7. Closed loop frequency response of compensated system.
Upper trace is gain, lower trace is phase shift.

To provide a less violent driving function, a digital circuit was used to generate a cubic polynomial transition waveform, assuring continuous accelerations throughout the switching cycle. Furthermore, to compensate for the control system's limited bandpass, this input waveform was tailored by adding an appropriate amount of quadratic polynomial so the mirror position follows the low jerk, cubic transition (fig. A.9). In that figure, notice the fast rise time and negligible overshoot and ripple. After implementation of the smooth transitions, there were no difficulties with failures of the linkages between the mirror and motors. Digital generation of the input waveform also facilitated the three position switching (fig. A.10) used to reduce the effects of atmospheric noise (Chapter 2).

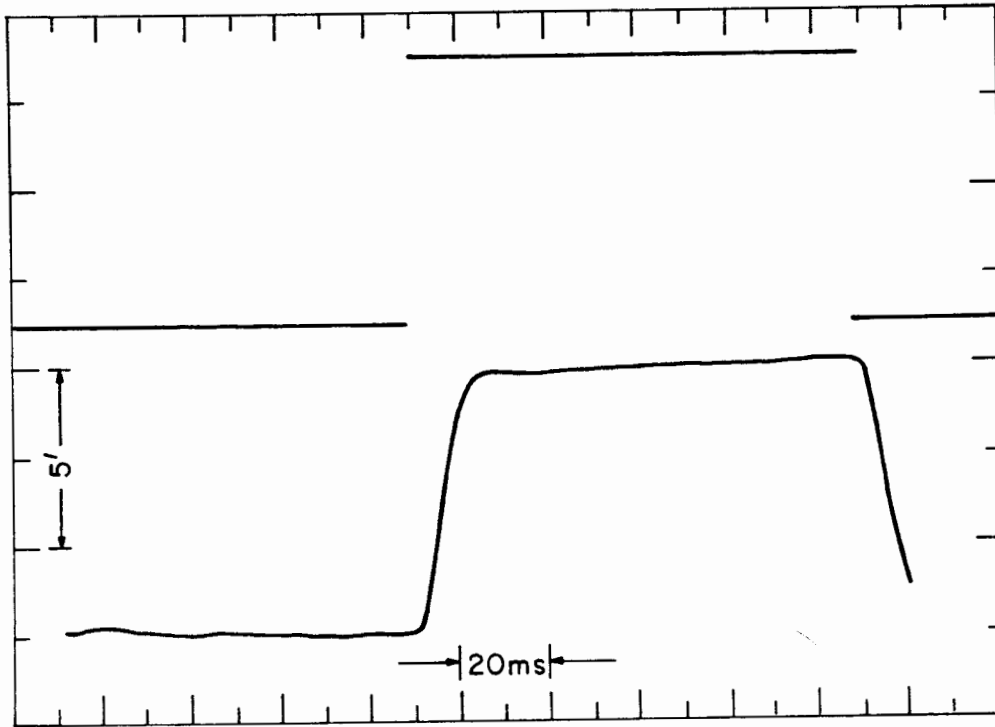


Figure A.8. Response of frequency compensated system to square wave input.

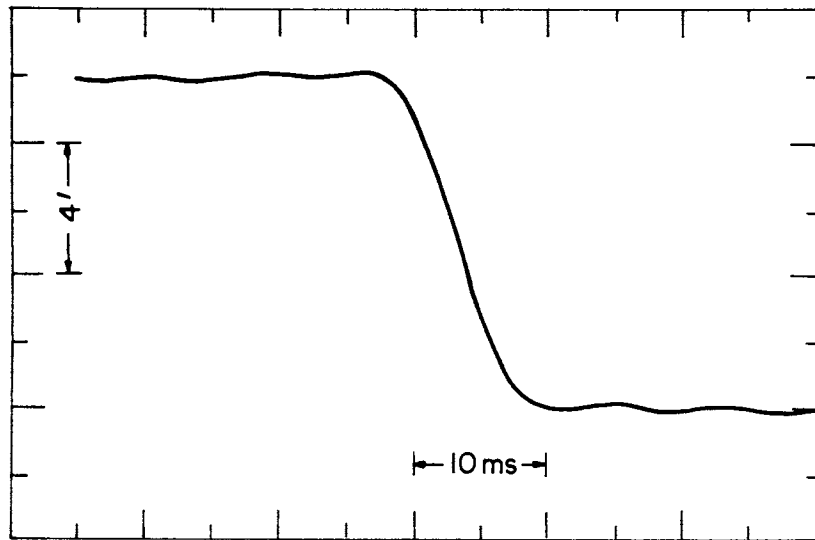


Figure A.9. Detail of system response to tailored input waveform.

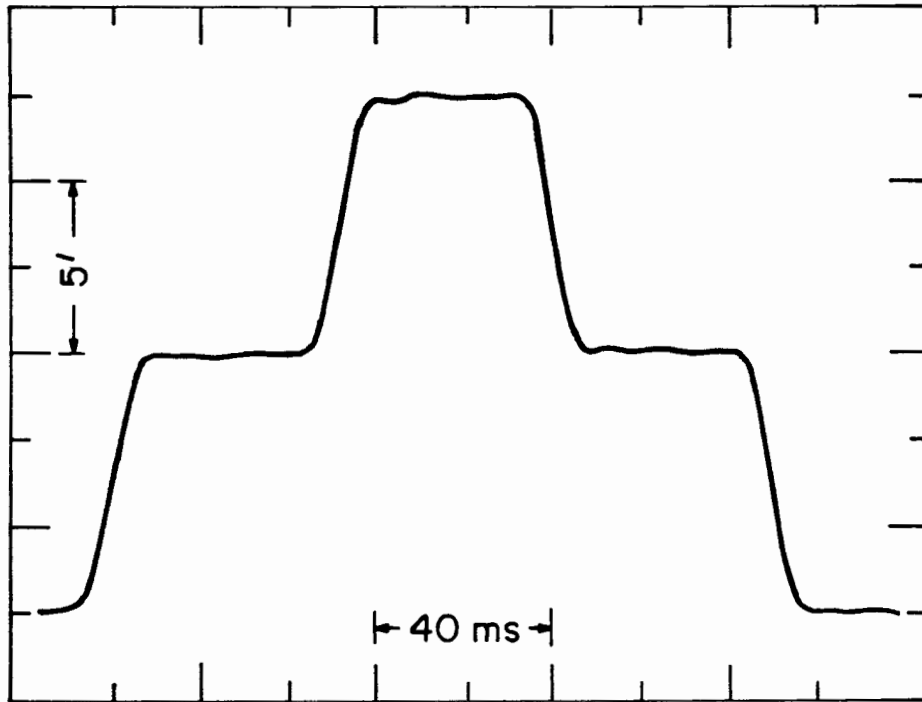


Figure A.10. Three position switching with tailored input waveform.

Appendix B. An Improved Far Infrared Photometer

Abstract

We describe the design, operation and performance of a high throughput far infrared photometer. The instrument is intended for astronomical observations at millimeter and submillimeter wavelengths and is suitable for use with either ground based or balloon borne telescopes.

I. Introduction

For observations of the cosmic background radiation, far infrared photometry with a bolometric detector is an attractive technique. Quasi-optical filters are available with large fractional bandwidths that match the transparent windows between atmospheric molecular absorption lines. Unlike a coherent radiometer, a bolometer can have, in principle, unlimited optical throughput. Such a high throughput system can take advantage of the collecting area of a large telescope for photometry of extended sources. Finally, the noise equivalent power of cryogenically cooled semiconductor bolometers is sufficiently small that the sensitivity of a high throughput, wide bandwidth, far infrared photometer is unequalled at short millimeter and submillimeter wavelengths.

In this paper, we describe a photometer designed for ground based and balloon borne observations of the cosmic background radiation. A versatile, self contained cryogenic refrigerator, the basis of the system, is described in Section II and its operation is detailed in Section III. Section IV describes the optical elements, which include a large area composite semiconductor bolometer, a cooled high throughput

condensing cone, and the filters which determine the photometer's spectral response. The performance of the instrument is discussed in Section V.

II. The Cryogenic System

Figures B.1 through B.3 illustrate the general arrangement of the cryostat. Two concerns motivated the asymmetric design. First the off-axis placement of the vent and pumping lines allows operation with the optic axis at any zenith angle up to 80° . Second, the position of the optical window adjacent to the external wall of the dewar permits two units to be used simultaneously in the focal plane of a single telescope. For example, measurements of an object at two wavelengths could be made using a Cassegrain telescope with a nutating subreflector. Both left and right handed units were produced. Because a lightweight instrument facilitates handling and balloon borne operation, aluminium was used extensively in the cryostat's construction to minimize its mass, which is less than 20 kg.

The welded aluminum main chamber has a volume of 4.5 ℓ and holds a bath of liquid ^4He at ambient pressure. By passing through a heat exchanger in the vent line, boil-off gas from this bath cools the radiation shield to about 90 K. Two independent, self contained, single cycle evaporation refrigerators are mounted on the bottom of the main chamber. Each refrigerator has its own activated charcoal cryopump in intimate thermal contact with the main liquid ^4He bath. A pair of hermetically sealed valves, mounted in the vacuum space and operated from outside the dewar, control operation of these pumps. The evaporators, each having a volume of 35 cm^3 , are supported by thin wall stainless steel pumping tubes telescoped in a triple wall arrangement that maximizes the thermal isolation of the evaporators while retaining compact construction. Condensation lines passing through the main

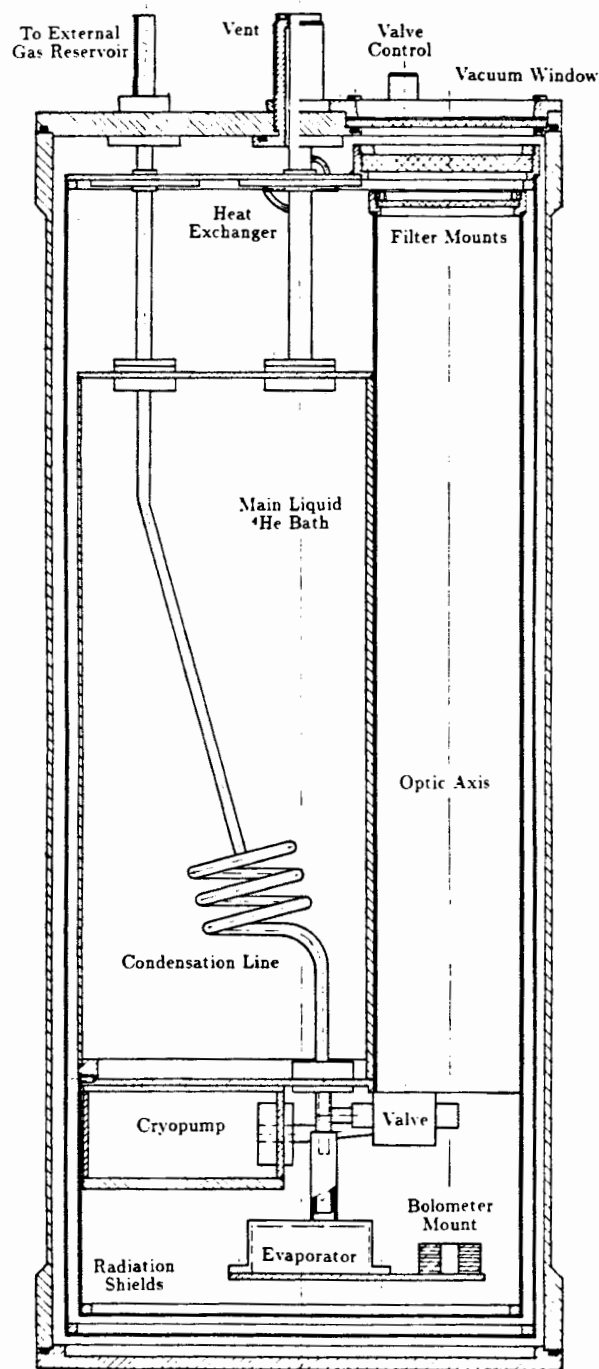


Figure B.1. Cross section of the cryostat, illustrating the major parts discussed in the text.

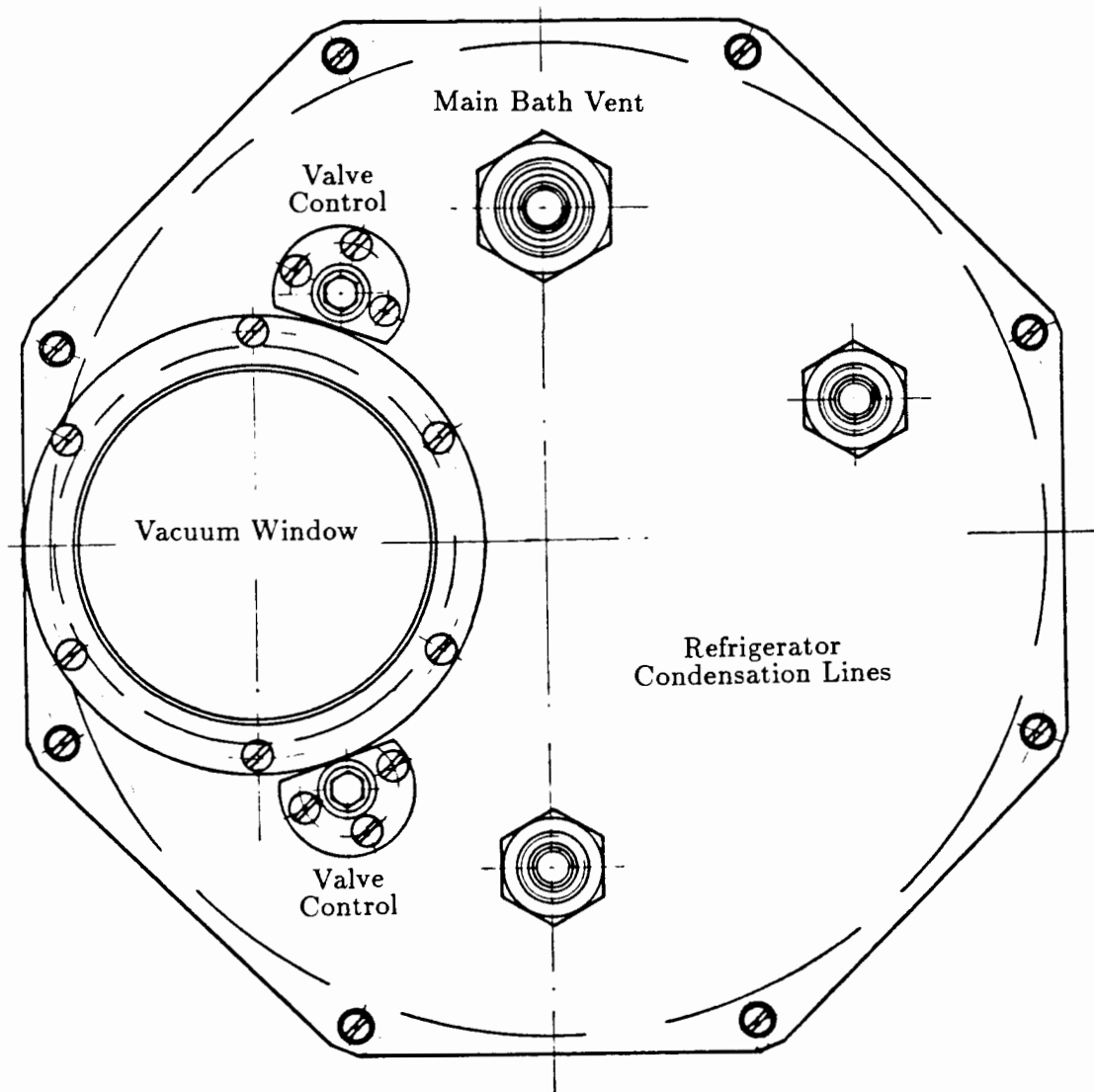


Figure B.2. Top view of cryostat, showing the asymmetric design.

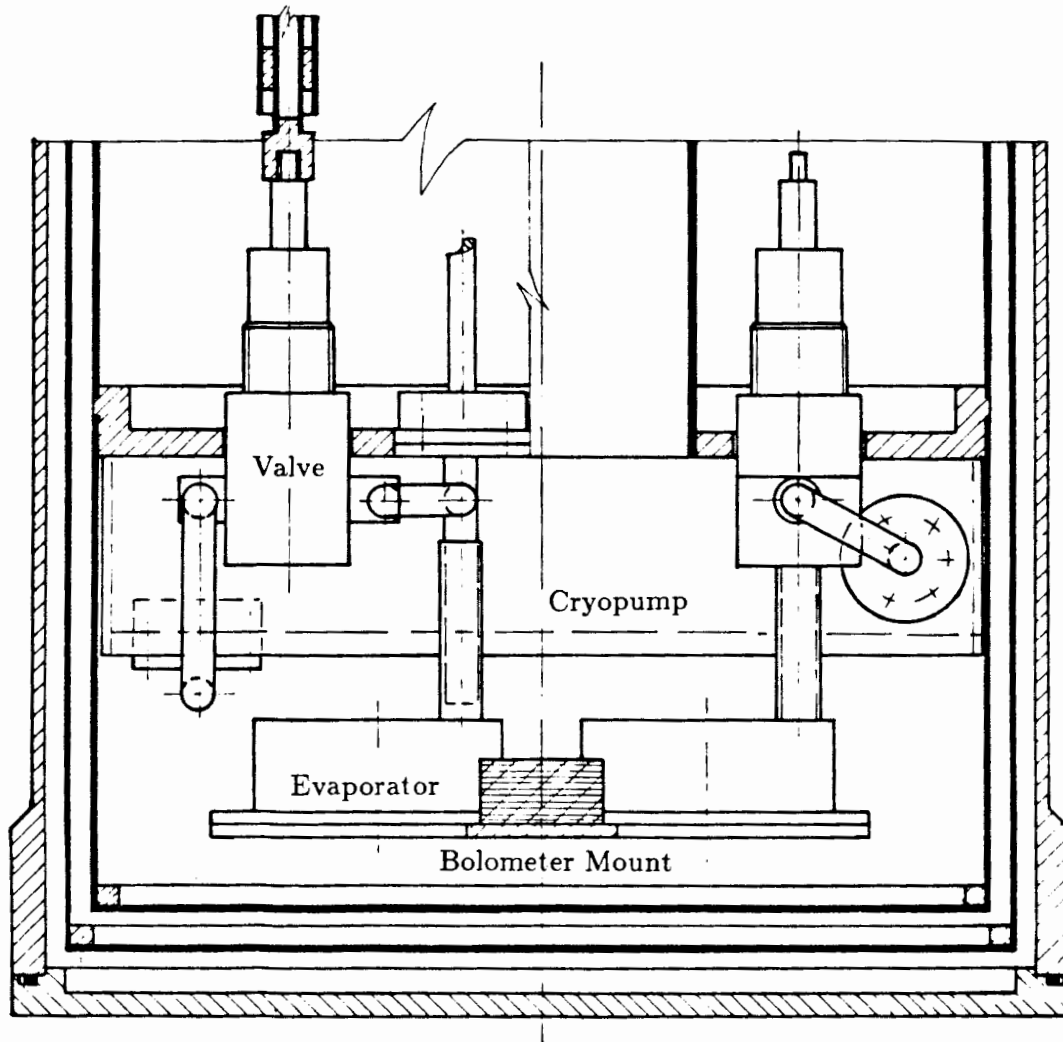


Figure B.3. Detail of the evaporation refrigerator mounting.

liquid helium bath connect external gas reservoirs with the evaporators and a gold-plated copper plate that thermally connects the two evaporators is the mounting surface for the detector and cold optics.

Although the sensitivity of cryogenic bolometers operated at 0.35 K is generally greater than those operated at 1 K, Ceccarelli *et al.*⁸⁰ have noted that a bolometer operating at 1 K may be used efficiently at ground based sites in certain situations. To allow flexibility in the choice of detector, therefore, we designed this cryostat to operate at either 1 K or 0.35 K.

One of the refrigerators precools the detector to 1 K by evaporating ^4He . The second refrigerator holds the detector at its working temperature. Depending on the temperature desired, either ^3He or ^4He may be used as the working fluid in this second refrigerator. If ^4He is chosen, a small capillary must be introduced at the exit from the second evaporator to break the superfluid film.

III. Cooling Procedure

A special procedure was developed to precool the low temperature stage without the use of a mechanical thermal switch. Beginning at room temperature, with the vacuum vessel and precooler evacuated, the cryopump valves closed, and the appropriate amount of either ^3He or ^4He in the gas reservoir of the second refrigerator, liquid nitrogen is introduced into the main bath and a few milliliters of oxygen are liquefied in the evaporator of the precooler. This brings the cryostat's interior temperature to 77 K. The oxygen is then removed by a mechanical vacuum pump, further cooling the refrigerators to 65 K. We chose oxygen as the working fluid for this step because the pressure at oxygen's triple point, 1.2 torr, is unusually low,

below the reach of a mechanical vacuum pump. This insures the oxygen will not solidify when it is evaporated.

After the oxygen is completely evaporated, the cryostat is inverted to empty it of nitrogen. Then the main chamber is filled with liquid helium, and 12 ℓ (s.t.p.) of ^4He are liquefied in the precooler. This also cools the bolometer and the helium in the second refrigerator to liquid helium temperature, 4.2 K.

When the refrigerators' temperature has stabilized, the precooler's cryopump valve is opened and evaporation of ^4He in this first refrigerator cools the detector mount to 1 K. At this temperature ^3He can be liquefied quite efficiently, with over 95% condensing into the liquid phase. Following evaporation of the precooler's ^4He , the second cryopump valve is opened. If ^4He is used in the second refrigerator, the temperature of the detector is maintained at 1K; otherwise, if ^3He is used, the detector is further cooled to 0.35K.

The holding time with the detector at its working temperature is typically longer than 15 hours, regardless of the helium isotope in the second refrigerator or the zenith angle of the optic axis. The minimum temperature attained with ^3He in the second refrigerator is about 5% lower when the cryostat is horizontal than when vertical, however, probably due to a increase in the surface area of the fluid in contact with the evaporator walls.

IV. Optical Elements

During measurements of the cosmic background radiation, we operated the cryostat at 0.35 K, using a composite semiconductor bolometer ⁸¹ constructed in D. A. Harper's laboratory at Yerkes Observatory. The bolometer has a gallium doped germanium thermometer element bonded to one face of an octagonal diamond

substrate, 5 mm across the flats and 0.1 mm thick and a bismuth absorbing film deposited on the diamond's opposite face. The absorbing film's surface resistivity, $177 \Omega/\square$, matches the impedance of the diamond. Glass fibers suspend the device in the center of a cylindrical cavity (8 mm diameter and 8 mm deep) in a copper block which is attached to the evaporation refrigerators.

The detector forms a simple voltage divider circuit with a thin film, $20 \text{ M}\Omega$ load resistor chip⁸² that is mounted adjacent on the refrigerator. This particular resistor model displays no excess noise⁸³ and is more compact and easier to mount than a wire wound resistor. Bias current is supplied by a battery, and a low noise JFET source follower, cooled to about 80 K, matches the high impedance bolometer circuit to the input of a low noise, high gain, room temperature preamplifier.

A compound parabolic concentrator^{84,85} and a cylindrical light pipe comprise the cold field optics of the instrument (fig. B.4). With entrance and exit apertures of 45 mm and 5 mm, respectively, the concentrator defines a 12° FWHM field of view. This matches an $f/4.5$ telescope focus, and has an optical throughput of $0.5 \text{ cm}^2 \text{ ster}$. Direct attachment to the bolometer mounting block cools the concentrator and also tightly couples the detector cavity to the exit aperture of the concentrator. The concentrator was made by electroforming a nickel flash and a 0.13 mm layer of copper over a polished stainless steel mandrel that had been machined with a numerically controlled lathe (Plate B.I). After the concentrator was removed from the mandrel, the inner reflective surface was gold plated.

The light pipe is a polished copper tube, 50 mm in diameter, in thermal contact with the main liquid helium bath. It couples the entrance of the concentrator to the entrance window of the cryostat.



Plate B.I: Steps in manufacture of compound parabolic concentrators. Left to right: unpolished stainless steel mandrel, mandrel after electroforming concentrator, polished mandrel after removal of concentrator, and the finished concentrator.

Table B.1 list the filters used to determine the spectral response of the instrument. The low frequency of the passband and the high throughput and large entrance aperture of the optics place stringent demands on the properties of filter materials.

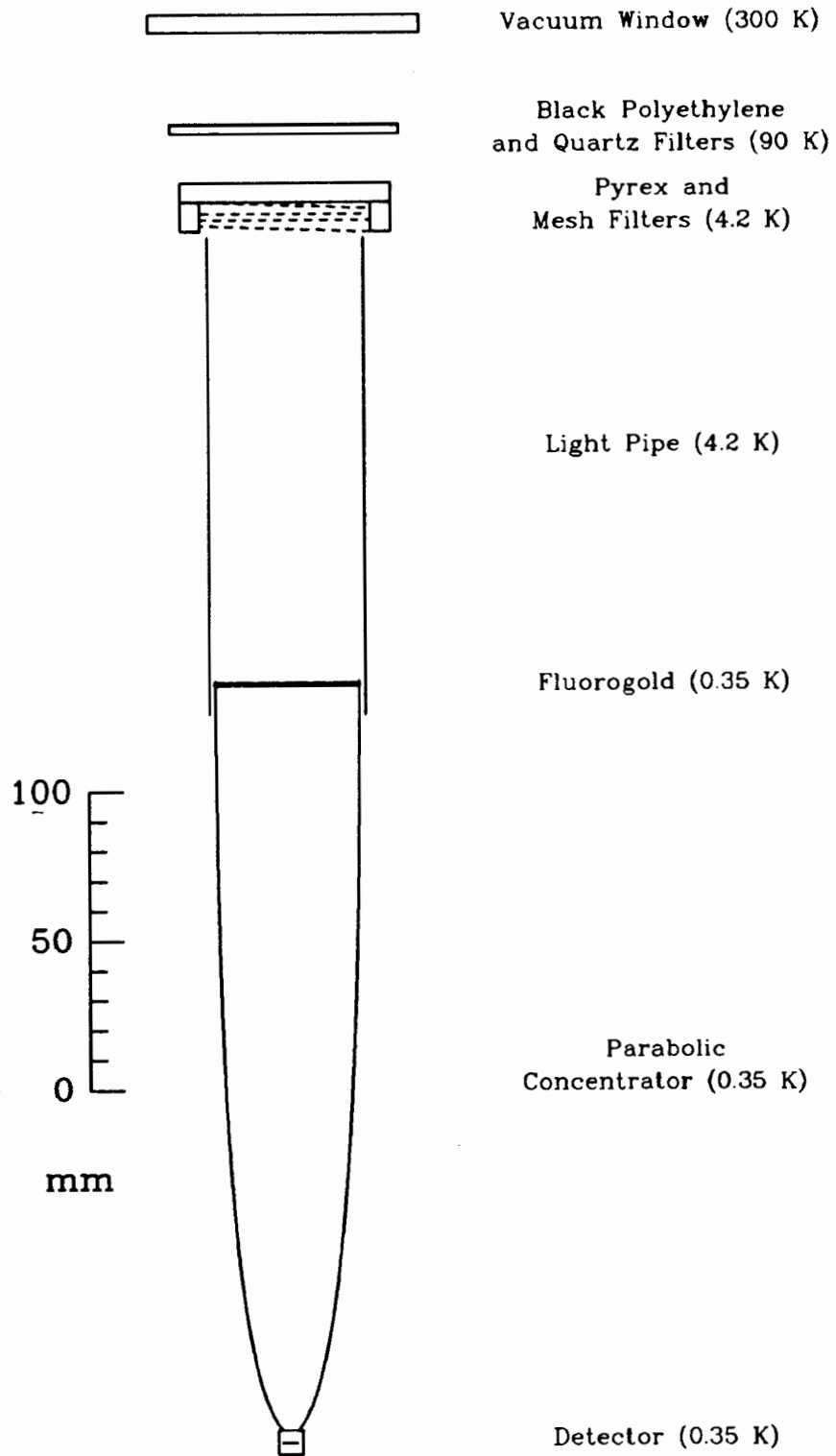


Figure B.4. Photometer optical elements.

Table B.1. Spectral Filters

Filter material	Position	Thickness	Temperature
Teflon	Vacuum window	3.0 mm	300 K
Black polyethylene	Radiation shield	0.2 mm	90 K
Crystal Quartz		3.0 mm	
Pyrex	Main helium bath	6.35 mm	4.2 K
Resonant Mesh		...	
Fluorogold	Cone entrance	1.5 mm	0.35 K
Black Paper	Cone exit	0.15 mm	0.35 K

The primary filter element is a resonant mesh⁸⁶ that defines the millimeter wavelength response of the instrument. This filter has a bandwidth of 1 cm^{-1} FWHM, centered at 4.5 cm^{-1} . A peak transmission of close to 80% was measured by the manufacturer and capacitive blocking meshes incorporated in the filter structure effectively suppress out of band transmission at frequencies below 30 cm^{-1}

Because the bolometer is an intrinsically broad band detector, proper blocking of optical and near infrared radiation is essential to successful operation. We found the submillimeter band between 30 cm^{-1} and 300 cm^{-1} especially difficult to block. Fluorogold,⁸⁷ a high temperature gasket material composed of glass fibers embedded in teflon, has previously been used as a blocking filter in this troublesome region. Fluorogold's low thermal conductivity and large heat capacity caused severe difficulties in our system, however, because the near infrared radiation absorbed by fluorogold tends heat the center of a large diameter filter several degrees above the temperature of the filter mount. Moreover, fluorogold has a large coefficient of thermal expansion, which makes maintaining good thermal contact between the filter and its mount difficult, exacerbating the heating problems. Thermal radiation

from such a warm filter decreases the sensitivity of the instrument by increasing the background radiation load on the detector. Raising the temperature of a fluorogold filter from 4.2 K to only 6 K or 7 K is sufficient to halve the detector sensitivity. Furthermore, the absorptivity of fluorogold is rather small at frequencies below 80 cm^{-1} so a very thick ($\sim 3\text{ cm}$) filter would be required to provide adequate blocking at 30 cm^{-1} , further complicating the mounting and thermal problems.

Halpern *et al.*⁸⁸ recently showed that Pyrex,⁸⁹ when cooled to 4.2 K, has several properties that make it an effective blocking filter for submillimeter wavelengths. First, Pyrex's low frequency absorptivity is greater than that of fluorogold, allowing a moderate thickness (6.34 mm) of Pyrex to provide adequate blocking at 30 cm^{-1} without reducing the transmission of the system at 4.5 cm^{-1} . Secondly, the ratio of heat capacity to thermal conductivity, or thermal time constant, is much less for pyrex than for fluorogold so thermal gradients across the filter are less severe. Finally, Pyrex's coefficient of thermal expansion is small, making it possible to maintain good thermal contact with the filter mount. By using a pyrex filter, we avoided the filter heating and bolometer loading problems we had experienced with fluorogold.

The black polyethylene and single crystal quartz mounted on the 90 K radiation shield are opaque⁹⁰ at frequencies above 300 cm^{-1} . To insure any stray near infrared radiation that leaks past the radiation shields will not reach the detector, we placed a thin fluorogold filter at the entrance to the condensing cone and a sheet of quartz loaded black paper⁹¹ immediately above the bolometer.

V. Performance

We measured the performance of the photometer both in the laboratory and at the focus of a Cassegrain radio telescope with a 9 m diameter primary aperture (Chapter 3). The laboratory tests confirmed the spectral response of the instrument and the electrical properties of the detector. From lunar observations with the telescope, we determined the sensitivity of our system when referred to a point above the atmosphere.

To confirm the efficacy of the blocking filters, we used a series of four brass wire meshes placed at 45° to the optic axis as low pass reflection filters. In this orientation, these meshes reflected only frequencies below 7, 9, 18, and 22 cm^{-1} , respectively, into the detector. The signal obtained by viewing a broad band source then represents the spectral response integrated from zero frequency up to the cutoff of the filter. We noted no significant difference between any of the meshes and an aluminum reflector, which implies there is no significant response except in the passband.

The electrical responsivity of the bolometer may be estimated from the slope of its load curve (fig. 5) at the working point.⁹² When the detector cavity was sealed at 0.35 K, so the device was not illuminated, we found a responsivity of 10^7 V/W . The voltage noise density of the circuit at 10 Hz, measured with a low frequency spectrum analyzer,⁹³ was $e_n = 12 \text{ nV}/\sqrt{\text{Hz}}$, consisting of approximately equal contributions from the detector and the JFET preamplifier. The intrinsic noise equivalent power of the electrical circuit is then $\text{NEP}_e = 1.2 \times 10^{-15} \text{ W}/\sqrt{\text{Hz}}$.

If, on the other hand, the bolometer viewed a 77 K black body through the filters, the effect of the radiation load was to shift the working point and decrease the responsivity to $6 \times 10^6 \text{ V/W}$. The noise power was correspondingly increased to

$NEP_e = 2 \times 10^{-15} \text{ W}/\sqrt{\text{Hz}}$. This radiation load is similar to the load from the sky when the photometer is at the telescope focus.

Lunar observations were undertaken to determine the sensitivity of the photometer to extended sources when operated in conjunction with the telescope (Chapter 3). These measurements consisted of short scans of the moon, together with determinations of the atmospheric opacity from the variation in the sky's brightness with zenith angle. Although the intrinsic detector noise remained constant, differences from night to night in the atmospheric opacity caused the effective noise level to vary when referred to a point above the atmosphere. Of the half dozen nights when measurements were made, the clearest night's opacity was $\tau = 0.2$, and the system noise level, expressed as a fractional change in the CBR temperature, was $\Delta T_N/T_{\text{CBR}} = 8.6 \times 10^{-3} \sqrt{\text{s}}$.

Vita

Simon John Elliot Radford, the first son of Jennifer and Roger Radford, was born in New York Infirmery on October 27, 1957. He grew up in New York City and attended Deerfield Academy. In 1979 he received a B. S. in Engineering Physics from Cornell University and, in 1982, a M. S. in Astronomy from the University of Washington.

Errata

August 19, 1987

On page 16,

$$\mathcal{F}_b(k) = \exp(-k^2\theta_b^2/16 \ln 2),$$

$$\dot{\mathcal{F}}_s(k) = 2i \sin(k_x\theta_s/2),$$

$$\mathcal{T}_s(k) = |\mathcal{F}_b\dot{\mathcal{F}}_s|^2 = 4 \sin^2(k_x\theta_s/2) \exp(-k^2\theta_b^2/8 \ln 2), \quad 2.13$$

and the units of the ordinate in Figure 2.5 are $\mathcal{T}_s/4$.

On page 17, the units of the ordinate in Figure 2.6 are $\mathcal{T}_s/4$, and

$$\mathcal{T}_{p,n}(k) = 4 \sin^{2n}(k_x\theta_s/2) \exp(-k^2\theta_b^2/8 \ln 2). \quad 2.15$$

On page 18,

$$C_s(\theta) = (2\pi)^{-2} \int_{-\infty}^{\infty} d^2k e^{-ik\theta} \mathcal{T}_s(k). \quad 2.17$$

On page 78,

$$\mathcal{T}_{2+1}(k) = \pi^{-2} \sin^4(k_x\theta_s/2) \sin^2(k_x\theta_w/2) \exp(-k^2\theta_b^2/8 \ln 2), \quad 4.6$$

and the units of the ordinate in Figure 2.7 are $\mathcal{T}_s/4$.